DYNAMIC STALL CHARACTERISTICS OF AN OSCILLATING AIRFOIL IN A HARMONICALLY VARYING FREESTREAM VELOCITY

A THESIS

Presented to

The Faculty of the Division of Graduate

Studies and Research

by

John Bruce Malone

In Partial Fulfillment

of the Requirements for the Degree

Doctor of Philosophy

in the School of Aerospace Engineering

Georgia Institute of Technology

December 1974

DYNAMIC STALL CHARACTERISTICS OF AN OSCILLATING AIRFOIL IN A HARMONICALLY VARYING FREESTREAM VELOCITY

Approved:

G. Alvin Pierce, Chairman

R. L. Carlson

D. P. Giddens

Date approved by Chairman: 11·15·74

ACKNOWLEDGMENTS

I would like to acknowledge the many people whose time and efforts have made the writing of this thesis possible. Foremost among these is my faculty advisor, Dr. G. Alvin Pierce. His guidance and encouragement throughout this thesis project and during my entire graduate studies program is most sincerely appreciated.

The final version of this thesis has incorporated many helpful suggestions from the faculty reading committe. I would like to thank the committee members, Dr. G. Alvin Pierce, Dr. Robert L. Carlson, and Dr. Donald P. Giddens, for their thorough reading of this paper. In addition, the work of Mrs. Ruth Shaw during the typing of both the rough and final draft of this paper is greatly appreciated.

The experimental phase of this project was made possible by the efforts of several people. I would like to acknowledge the many hours spent by Mr. John Caudell in preparing the electronic equipment used for the experimental tests. Appreciation is extended to Mr. Donald Kunz for his aid in running the wind tunnel facility and for the taking of test data, and also to Mr. John Gaines, for his help during the installation of the gust generator mechanism.

Finally, to my parents, and to my wife, Linda, I would like to express my deepest gratitude and affection for the many years of patience and personal sacrifice that they have given to me throughout my academic career.

Special permission was received from the Division of Graduate Studies to vary from the Thesis Manual instructions for figure numbers in order to meet the requirements of this work.

TABLE OF CONTENTS

LIST OF TABLES

LIST OF FIGURES

SYMBOLS

a	airfoil torsional axis location as percentage of semi-chord; positive aft of half chord point
A_R	gust amplitude ratio
b	airfoil semi-chord
B_o	amplitude of airfoil pitching oscillations
C_L	lift coefficient
C_M	moment coefficient
C_W	work coefficient
C_{L_o}	steady portion of lift coefficient
C_{M_o}	steady portion of moment coefficient
$C(k)$	Theodorsen's function
D_a	gust double amplitude
E	hot wire voltage
F_R	frequency ratio
F_{max}	maximum amplitude of force
f_d	damped natural frequency (Hertz)
f_o	lowest measurable velocity with hot wire probe
$F(k)$	real part of Theodorsen's function
$G(k)$	imaginary part of Theodorsen's function
h	total vertical displacement

h_o	mean vertical displacement
Δh	manometer column height
I	mass moment of inertia of dummy shaft
I_d	mass moment of inertia of drive arm
I_m	mass moment of inertia of airfoil model and adjustment disks
I_t	mass moment of inertia of model, disks, rigid linkage, and drive arm
K	spring constant
k_v	reduced frequency of tunnel velocity, based on airfoil semi-chord
k_b	reduced frequency of airfoil
k_{vb}	reduced frequency based on the sum of tunnel velocity and airfoil frequencies, and airfoil semi-chord
L	lift force
ℓ_T	distance between model shaft and airfoil trailing edge
M	aerodynamic moment
M_d	moment at drive arm during forced elastic oscillations of airfoil
M_R	total applied moment
P_o	stagnation pressure
r	effective length of drive arm
R_L	amplitude of unsteady lift
R_m	amplitude of unsteady moment
R_N	Reynold's number
t	time

T_o	stagnation temperature
V	tunnel velocity
V_o	mean tunnel velocity
V_1	percentage amplitude variation of freestream velocity from mean value of tunnel speed
$\alpha_{S.S.}$	static stall angle of airfoil
δ	logarithmic-decrement
ω	drive arm oscillation frequency (rad/sec)
ω_b	airfoil rotational oscillation frequency (rad/sec)
ω_d	damped natural frequency (rad/sec)
ω_h	airfoil vertical oscillation frequency (rad/sec)
ω_n	natural frequency (rad/sec)
ω_v	freestream oscillation frequency (rad/sec)
φ	phase angle
φ_R	phase angle between rotation displacement and velocity @ t = 0
φ_h	phase angle between vertical displacement and velocity @ t = 0
ρ	air density
θ	angle of attack
θ_d	angular rotation of drive arm
θ_o	mean angle of attack
$\Delta\theta$	instantaneous change in angle of attack
$\dot{\theta}$	angular velocity
$\ddot{\theta}$	angular acceleration

σ	standard deviation
ζ	damping factor

SUMMARY

The unsteady freestream environment of a helicopter rotor blade in forward flight was simulated using a gust generator mechanism installed in a low-turbulence wind tunnel. The gust generator mechanism produces a two-dimensional, sinusoidal, axial gust with a variation in velocity of up to seventy percent of the mean tunnel speed. This facility was used to study the effects of an unsteady freestream on the dynamic stall characteristics of an oscillating airfoil.

The model used for this investigation had a NACA 0012 contour, and was oscillated in pitch about the quarter-chord point. The amplitude of oscillation was varied between 2 and 8 degrees, while the mean angle of attack ranged from 0 to 20 degrees. The frequency of the axial gust was varied between .5 and 2 Hertz. An operational analog computer was used to obtain both the aerodynamic moment acting on the model, and the work done by the moment during pitching oscillations of the airfoil.

The experimental tests indicate that the unsteady freestream can produce large changes in the shape of the aerodynamic moment versus angle of attack hysteresis loops. The test results also show that the stability of the system, as evidenced by the work done on the oscillating airfoil, can be adversely effected by the unsteady freestream under certain parametric conditions.

CHAPTER I

INTRODUCTION

The experimental investigation described in this thesis was designed to examine how a harmonic variation in freestream velocity alters the lift and moment acting on a two-dimensional airfoil. Emphasis was placed on determining the effect that this type of unsteady freestream has on the dynamic stall characteristics of an airfoil oscillating in pitch. The following paragraphs provide a brief discussion of the dynamic stall phenomenon and its importance in helicopter rotor aerodynamics.

Dynamic stall of a lifting surface in a freestream occurs when the airfoil angle of attack increases at a finite rate until stall is produced. The factor that differentiates between dynamic stall and static stall is the presence of the non-zero angular rate of change superimposed on a high airfoil angle-of-attack. The angle of attack change can either be a rapid increase into the stall region, or it can be an oscillatory motion which results in a periodic stall and unstalling of the airfoil. In either case, the aerodynamic forces acting on an airfoil experiencing dynamic stall are very different from those developed during static-stall for the same airfoil [1-6].

The effects of dynamic stall are important in several areas of aircraft design and related fields. For example, compressor blades are subject to dynamic stall for certain inlet conditions. Sudden wind gusts

on an aircraft wing, or abrupt maneuvers of the vehicle can produce dynamic stall. Helicopters operating at high thrust coefficients while in hovering or vertical flight can also experience dynamic stall over portions of the rotor azimuth. Since the dynamic stall of a lifting surface produces large increases in lift and aerodynamic moment [1-6] over the statically measured values, the fatigue life of the structure can be adversely effected.

Dynamic stall can also occur on a helicopter rotor during forward flight. Due to the vector addition of the helicopter forward velocity and the rotor blade rotational velocity, each segment of the rotor blade sees a harmonically varying freestream velocity. The consequent variation in dynamic pressure causes an inequality of lift force between the advancing and retreating blades which can produce an unwanted rolling moment about the rotor hub. In order to counteract this effect, cyclic pitch is introduced into the blade motion to balance out the lift forces by harmonically decreasing the angle of attack on the advancing side and increasing the angle of attack on the retreating side. As forward speed is increased, the rotor shaft must be tilted forward, thereby further increasing the retreating blade angle. At some forward speed the retreating blade is operating at such a high angle that airfoil stall is produced. Since the cyclic pitch produces a finite value of angular rate, the stall which occurs on the rotor blade is a dynamic type of stall.

Along with the larger than normal airloads produced during dynamic stall, the rotor blade can, under certain conditions, absorb

energy from the freestream. This transfer of energy to the structure can cause the phenomenon known as stall flutter. Stall flutter is a limit cycle type of aeroelastic oscillation that produces large vibration levels in the rotor control linkages, which not only reduce pilot comfort and the rotor blade fatigue life, but in addition, actually imposes an operational limit to helicopter performance. Hence, an accurate knowledge of the forces, moments, and aerodynamic work produced during dynamic stall is of great importance.

Recent studies [7-10] have made use of unsteady aerodynamics by introducing data obtained from dynamic stall experiments into existing helicopter rotor loads programs. These modified programs have given results which show a marked improvement in the correlation of theoretical data with inflight measured airloads. This observation further indicates the need for obtaining accurate unsteady aerodynamic data for airfoils experiencing dynamic stall.

Several authors have recently made theoretical analyses which have made substantial contributions to the understanding of dynamic stall [11-12]. At this time, however, both the difficulties in developing an exact mathematical model of the fluid flow about a stalled airfoil and the complexity of solving the unsteady Navier-Stokes equations have prevented the development of an acceptable analytical solution to the dynamic stall problem. As a consequence of this, the main thrust in the past two decades has been directed towards the experimental determination of airfoil forces and moments produced during dynamic stall. For the case of the helicopter in forward flight, the forces and moments acting on oscillating airfoils in constant velocity

freestreams have been determined experimentally by a number of authors.

One of the earliest and most exhaustive studies of dynamic stall was performed by R. L. Halfman, H. C. Johnson and S. M. Halsey [1]. In 1951 they reported results on tests using an airfoil that could oscillate in pitch and in translation about various mean angles of attack. From these tests the effects of various parameters, such as reduced frequency and mean angle, on the airfoil forces and moments were determined. Curves were presented of the lift forces and aerodynamic moments versus the airfoil angle of attack. For the pitching oscillations, the work per cycle was obtained by integration of the moment versus angle curves. An examination of these curves shows that for high values of mean angle the lift reaches a higher than normal value before stall occurs. Also, the moment versus angle curves show that a large nose down aerodynamic moment occurs just prior to airfoil stall. The curves of work per cycle versus reduced frequency indicate that for certain combinations of mean angle and reduced frequency, positive work is done on the airfoil by the airstream. This absorption of energy by the airfoil has been identified as the cause of the stall flutter phenomenon by several authors [1,13].

In another early experiment, A. G. Rainey [14] measured the forces and moments on a finite wing oscillating in pitch about the midchord. The researcher presented his experimental data in the form of curves of normal force and moment slopes versus reduced frequency. One important result of Rainey's report was presentation of the experimental evidence of the delay of flow separation from the lifting surface due to a positive value of angular rate during the upstroke of

each oscillation cycle. This delay in flow separation allows the airfoil to pitch to a higher angle of attack before stalling occurs, thereby causing the high values of lift which are attained on the airfoil during dynamic stall.

In recent years, several other experimental programs have been conducted to obtain the forces and moments acting on thin airfoils oscillating at or near stall [2-5,15]. The airfoil data were presented both graphically by means of lift and moment hysteresis loops and in tabular form. The effects of various parameters such as angular amplitude, frequency, Mach number and mean angle have been throughly investigated. As in the experimental programs, all of the loads were obtained for constant freestream velocities during oscillation of the airfoil.

Some of the most recently reported experiments were performed by F.O. Carta, et al. [6]. Using a method described in Reference 16, they tabulated their unsteady airfoil data obtained from pitching oscillations in terms of parameters containing angle of attack, its rate and acceleration. They showed that the original experimental normal force and moment loops could be accurately reproduced by making use of their data in tabular form.

Another approach to the problem, besides the direct measurement of aerodynamic forces, has been to examine the details of the mechanics of dynamic stall. Early experiments showed that a strong vortex is shed from the upper surface of the airfoil during dynamic stall [13]. As it passes over the airfoil surface, the vortex alters the pressure distribution around the airfoil and produces among other things, a

large nose-down aerodynamic moment. Recently, J. M. Martin [17] and his associates found experimental evidence that more than one vortex can be shed during each airfoil oscillation, depending on the value of the reduced frequency.

W. Johnson and N. D. Ham [18] have described experimental and analytical studies which also emphasize the importance of vortex shedding during dynamic stall. Using a potential theory, they showed that the addition of a large vortex traveling downstream over the airfoil surface produced theoretical pressure distributions similar to those found experimentally [19]. Therefore, the presence of the shed vorticity close to the airfoil surface and in the near wake during dynamic stall may be expected to have an effect on the forces and moments experienced by the lifting surface.

To correctly simulate the dynamic stall environment of a helicopter rotor in forward flight, consideration should be given to the fact that the local velocity experienced by the blade, and consequently the vortex transport velocity, is not constant. At any particular radius it varies harmonically with the rotor angular velocity. As has been mentioned previously, however, all of the experiments to date on dynamic stall have been conducted with the freestream velocity held constant during airfoil oscillations. Therefore, since the velocity of the shed vorticity determines its distance from and effect on the nearby airfoil surface, it would seem that additional experimental work which takes into account a harmonically varying freestream velocity is needed.

In order to investigate the effects of a varying freestream velocity on airfoil airloads, a gust generating mechanism was installed

in the Georgia Tech Low Turbulence Wind Tunnel. The wind tunnel is of the open circuit type with an upstream fan which produces a maximum tunnel speed of approximately 50 mph. The mechanism consists of six rotating vanes installed at the down-stream exit of the tunnel. When rotated during wind tunnel operation, these vanes produce a harmonic variation in freestream velocity throughout the tunnel test section.

An airfoil model with a NACA 0012 section was used and a support system was designed to allow pitching oscillations about the quarter chord. The airfoil mean angle of attack, the amplitude of oscillation, and the frequency of pitching oscillations were varied within certain limits.

The lift force acting on the airfoil was determined using two different techniques. One method made use of two piezoelectric load cells incorporated into the model support located on either side of the wind tunnel. The second method used a pair of strain gage bridges which were installed on the same model supports.

The total applied moment, which included the inertia of the system, was obtained using both a third load cell and another strain gage bridge located on the model drive assembly. An operational analog computer with parallel logic was used to separate the aerodynamic moment from the total applied moment by continuously solving the airfoil equations of motion. In addition, the work done on the airfoil by the aerodynamic moment was determined using the analog computer.

During an experiment, several parameters were varied to determine the effects of freestream oscillation on the airfoil aerodynamics. Among the parameters studied were the frequency ratio (i.e., airfoil frequency

to freestream frequency), amplitude ratio (freestream double amplitude to mean freestream velocity), and the airfoil mean angle of attack.

CHAPTER II

WIND TUNNEL FACILITY

The gust generator designed for the investigation described here is installed in the Low Turbulence Wind Tunnel (Figure 2-1) at the Georgia Institute of Technology. The facility is a closed-jet open-circuit type with the fan located at the upstream tunnel entrance. The maximum test-section airspeed under normal operating conditions is approximately 80 ft/sec.

Flow straightening honeycomb is located in the settling chamber which is just forward of the converging nozzle. One sidewall of the test-section is of a variable-contour design which can be adjusted by screw-jacks located along the entire downstream portion of the tunnel. For the gust generator calibration tests, the test-section sidewalls were parallel, giving a square cross section of 42 inches on a side. The gust generator was installed at the wind tunnel.

Gust Generator Mechanism

The gust generator (Figure 2-2) consists of four major component groups: drive motor and controls; drive-side gear-box assembly; idle-side assembly; and gust generator vanes.

The drive motor (Figure 2-3) is a Wood's, one horsepower, SCR motor. The motor torque and speed are regulated by a Wood's ULTRACON SCR drive control, Model U-100. Power is applied to the drive-side gear-box through a drive belt and a pair of pulleys.

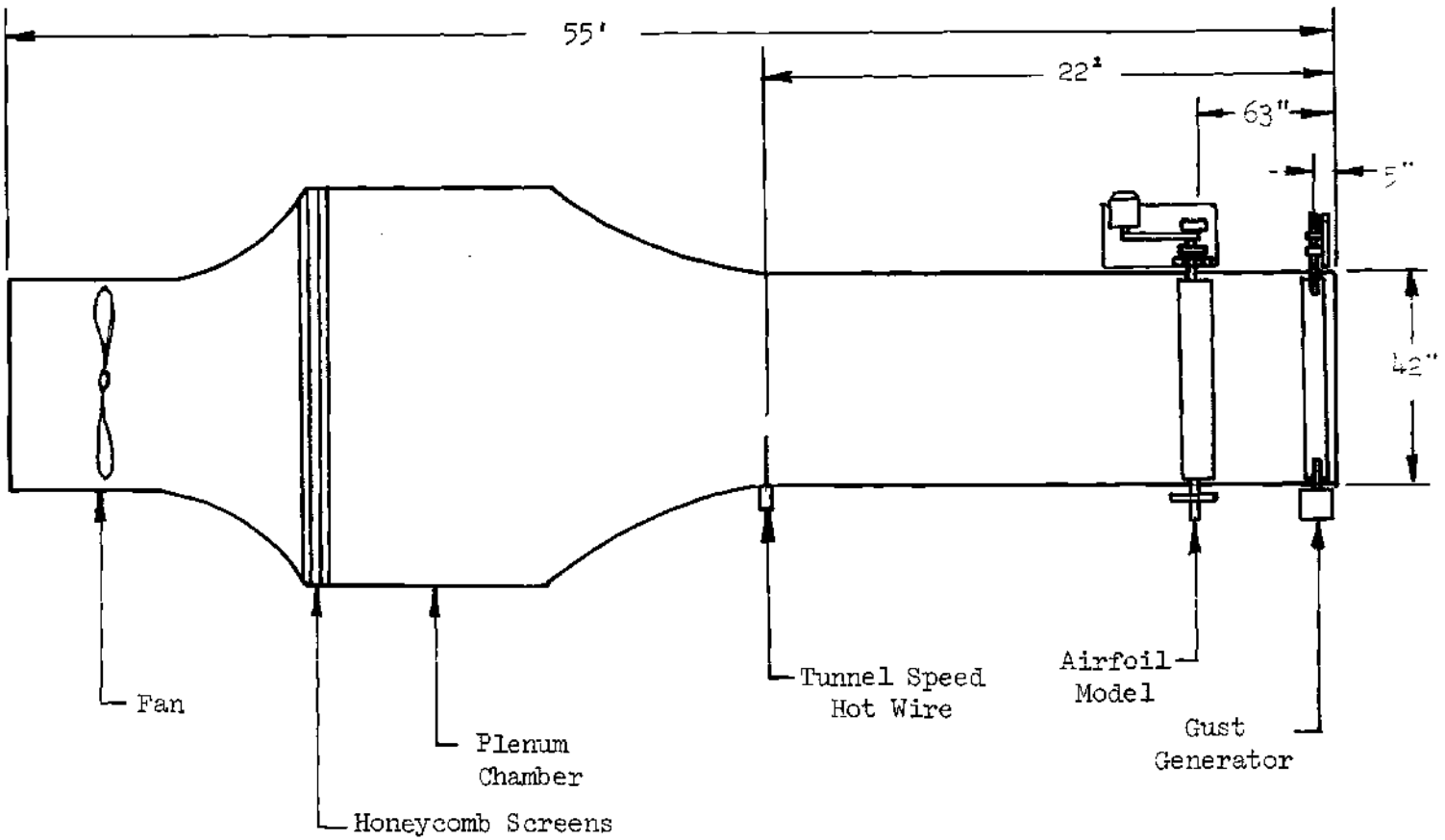

Figure 2-1. Low Turbulence Wind Tunnel

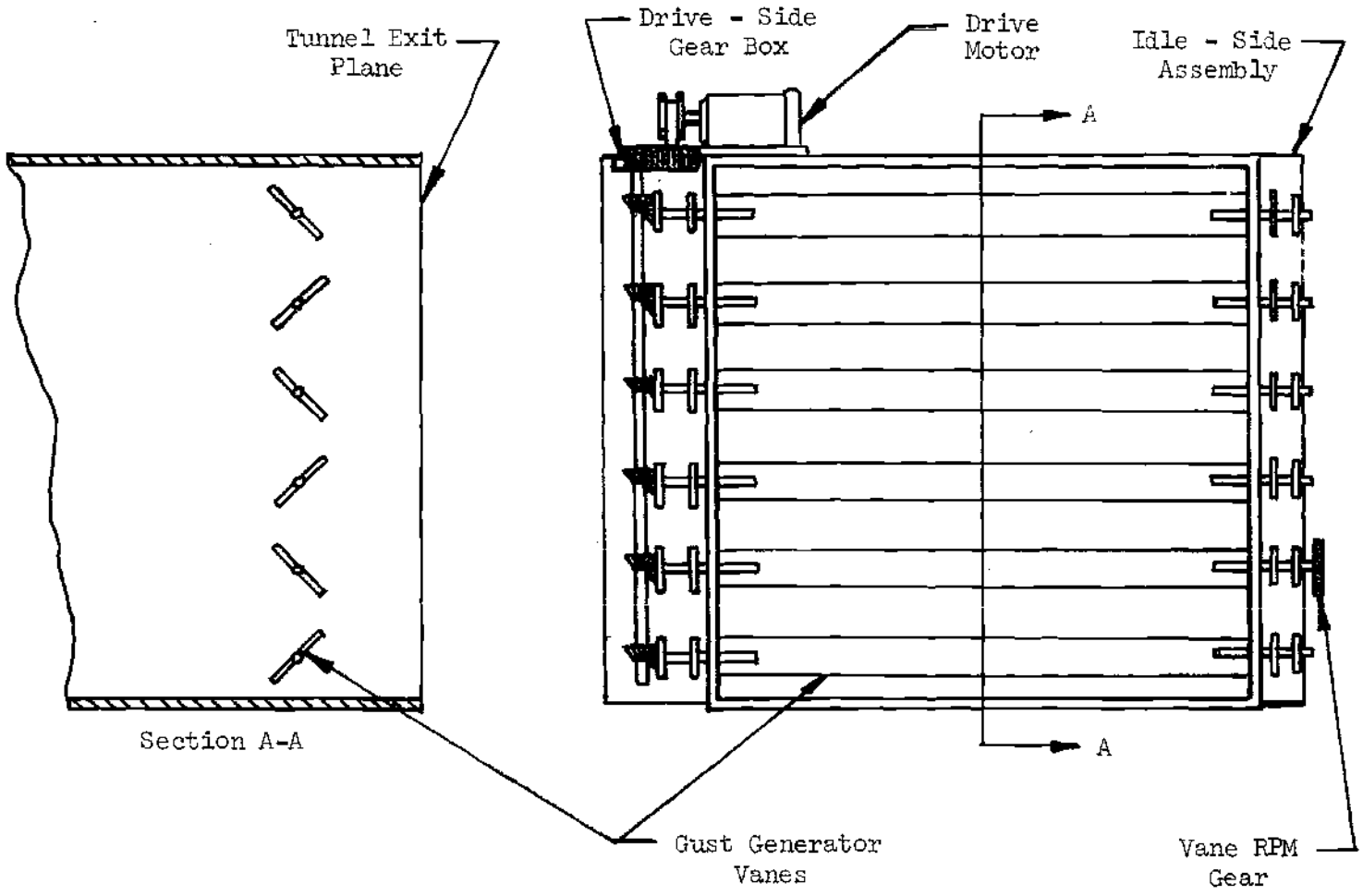

Figure 2-2. Gust Generator Mechanism

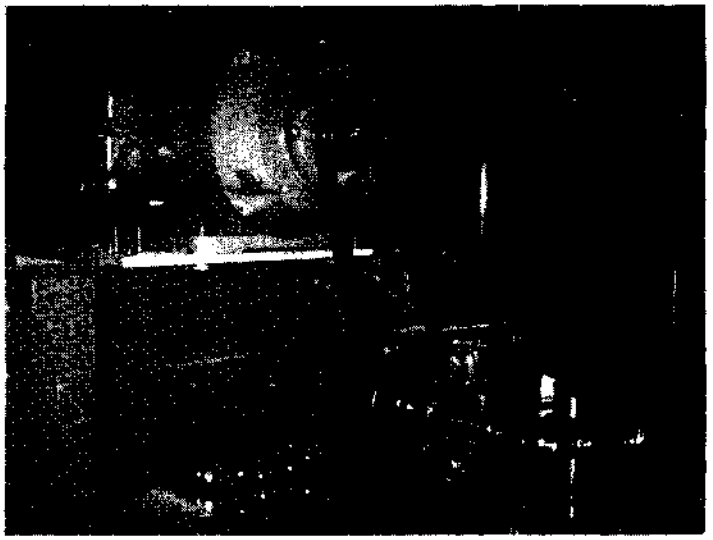

Figure 2-3. Gust Generator Drive Motor

The drive-side gear-box assembly (Figure 2-4) serves to impart rotational motion to six vanes which span the wind tunnel exit. The assembly has a worm gear which reduces the gear ratio between the drive motor and the gust generator vanes. A vertical shaft transmits the rotational motion through bevel gears to six, 18 inch long, slotted shafts which are supported by pairs of pillow blocks. The gust generator vanes on the drive side are fitted into the slotted shafts and are each secured by two screws. The entire gear-box assembly is surrounded by a safety cover.

The idle-side assembly (Figure 2-5) consists of six, 18 inch long, slotted shafts, each supported by pairs of pillow blocks. The gust generator vanes are attached to these shafts on the idle side in a manner similar to that on the drive side. A sixty-tooth gear attached to the end of one of the shafts outside of the tunnel is used, together with a magnetic detection device, to determine the rotational rate of the gust generator vanes.

The gust generator vanes (Figure 2-6) are aluminum rectangles, 1/4 inch thick, and $42\frac{1}{2}$ inches in length. There are three sets of six vanes, each set having differing widths. The widths are 2, $3\frac{1}{2}$, and 4-7/8 inches which cause, respectively, a 25%, 50%, and 75% blockage of the tunnel exit when the vanes are in a vertical position. The vanes are geared to rotate in alternating directions in order to minimize the effect of aerodynamic forces on the supporting shafts and mechanism.

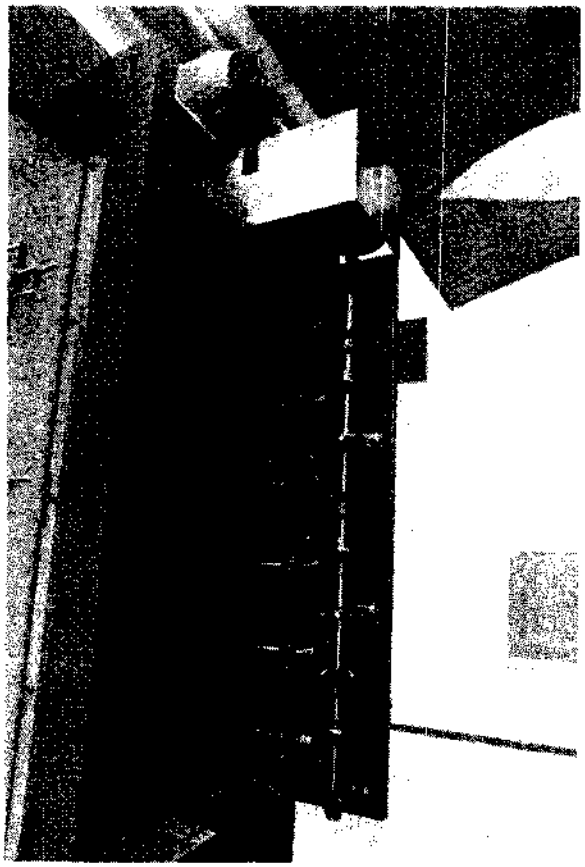

Figure 2-4. Drive Side Gear Box - Safety Cover Removed

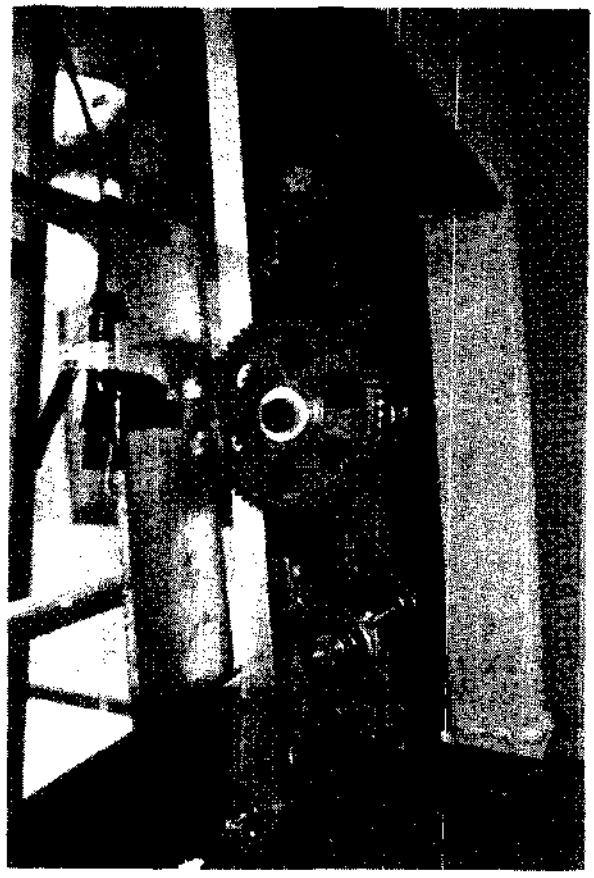

Figure 2-5. Idle-Side Assembly and RPM Timing Gear

Figure 2-6. Gust Generator Vanes Installed in Wind Tunnel (view upstream)

Installation of the Gust Generator in the Wind Tunnel

The gust generator was installed approximately five inches upstream from the tunnel exit. The drive and idle assemblies were independently bolted to the tunnel frame and then aligned horizontally and vertically with respect to each other to allow for proper installation of the rotating vanes.

Three plexiglass panels which are normally installed in one of the tunnel walls were removed and replaced with 3/4 inch plywood sheets. The plywood sheets were secured by metal braces and were adjusted by means of screws so that the edges of adjacent sheets were flush with each other inside of the wind tunnel. These plywood sheets not only served to stiffen this portion of the wind tunnel, but also provided access for the hot wire probe during testing. A total of eighteen, $1\frac{1}{2}$ inch diameter access holes were drilled for the hot wire probe and fitted with wooden plugs which could be removed or secured in place as required from the outside of the wind tunnel.

A magnetic detection device was installed on the idle-side assembly by means of an aluminum support. The device was adjusted so that its face was within .003 of an inch from the outside surface of the sixty-tooth gear which was attached to one of the idle-side vane shafts. The device produces a voltage signal for each passage of a tooth on the rotating gear. The closer the device is to the gear surface, the larger the voltage that is produced. The signal was then fed into an electronic counter. The sixty teeth on the gear, coupled with a one-second counting duration, gave a readout of vane speed in revolutions per minute. Since each revolution of the vanes produces two pressure

pulses in the airstream, the gust frequency produced is twice the vane frequency.

Hot Wire Anemometer and Probe Assembly

The anemometer used for the gust generator calibration was a Flow Corporation constant-temperature hot wire anemometer, Model 900A. The hot wire probe was also manufactured by the Flow Corporation and was 14 inches in length, and 1/4 inch in diameter. The probe sensing element consisted of .00035 inch diameter tungsten wire which was welded to the probe tip. This gave a value of f_o for the hot wire of approximately two ft/sec.

Since the hot wire probe was too short to permit velocity measurements at the tunnel centerline or beyond, a steel extension tube was constructed to which the probe was connected. The tube was 1-1/8 inches in diameter and 28 inches in length. With this extra length, velocity measurements could be made to within 9 inches of the far tunnel wall.

Because of the weight of the steel extension tube, a fairly substantial support was needed for the hot wire probe assembly. A cylindrical holder was devised which could be mounted horizontally, over top of three 1/4 inch screws which were attached, symmetrically, around each hole drilled in the plywood tunnel walls. Three wing nuts were used to secure the holder to the tunnel wall. A rubber gasket, between the holder and the wall, served to provide an airtight seal for the probe assembly. A set screw located at the end of the holder was provided to securely clamp the hot wire probe in any desired position. A scale in inches was etched into the tube along its length to establish

the location of the hot wire tip when the probe was inside the wind tunnel.

Hot Wire Calibration

The hot wire was calibrated in the low-turbulence wind tunnel. Gust generator vanes were installed across the tunnel exit and rotated into a horizontal position during the calibration. A pitot-static tube was inserted into the tunnel from the top of the facility and located on the tunnel centerline. The tube was then connected to a manometer located in the tunnel control room. The manometer column height was adjusted to read zero with the tunnel turned off. The hot wire probe was then installed so that the probe tip was in line vertically with the pitot static tube and approximately five inches below the bottom of the tube.

The hot wire signal from the anemometer was measured on a digital voltmeter. The wind tunnel was then started in order to obtain a signal from the hot wire other than the zero-velocity voltage. The hot wire signal was maximized by rotating the hot wire while monitoring the digital voltmeter. When the voltage was a maximum, the hot wire was clamped in position.

The calibration procedure consisted of setting an arbitrary wind tunnel speed and then adjusting the manometer to obtain the column height which represented this airspeed. The corresponding hot wire voltage was obtained from the digital voltmeter. This procedure was repeated for various airspeeds ranging from about five to seventy feet per second. Corresponding values of column height, Δh, and hot wire

Voltage, E , were recorded for each airspeed.

The stagnation temperature and pressure were measured and recorded before beginning the hot wire calibration. The stagnation temperature was measured again after the tests and was found to have increased by several degrees Fahrenheit. The actual temperature used in the calibrations was taken as the average of the two values.

A computer program was used to determine the wind tunnel airspeeds corresponding to the values of Δh recorded during the calibration. Bernoulli's incompressible flow equation was used to determine velocity, V , with respect to Δh. The equation is given below.

$$V = 119.9756038 \sqrt{\frac{\Delta h \; T_o}{p_o}} \qquad (2\text{-}1)$$

The program also established least-squares curve fits to E^2 versus $\sqrt{V}$ data obtained from the calibration. Both linear and quadratic fits were determined with their associated standard deviations, σ , in ft/sec. The quadratic least-squares curve had the smallest values of σ and was used as the calibration curve for the hot wire (Figure 2-7). The final equation relating velocity to hot wire voltage is given below.

$$V = \left(100.106 - \sqrt{10771.5 - 1082.02 \; E^2}\right. \qquad (2\text{-}2)$$

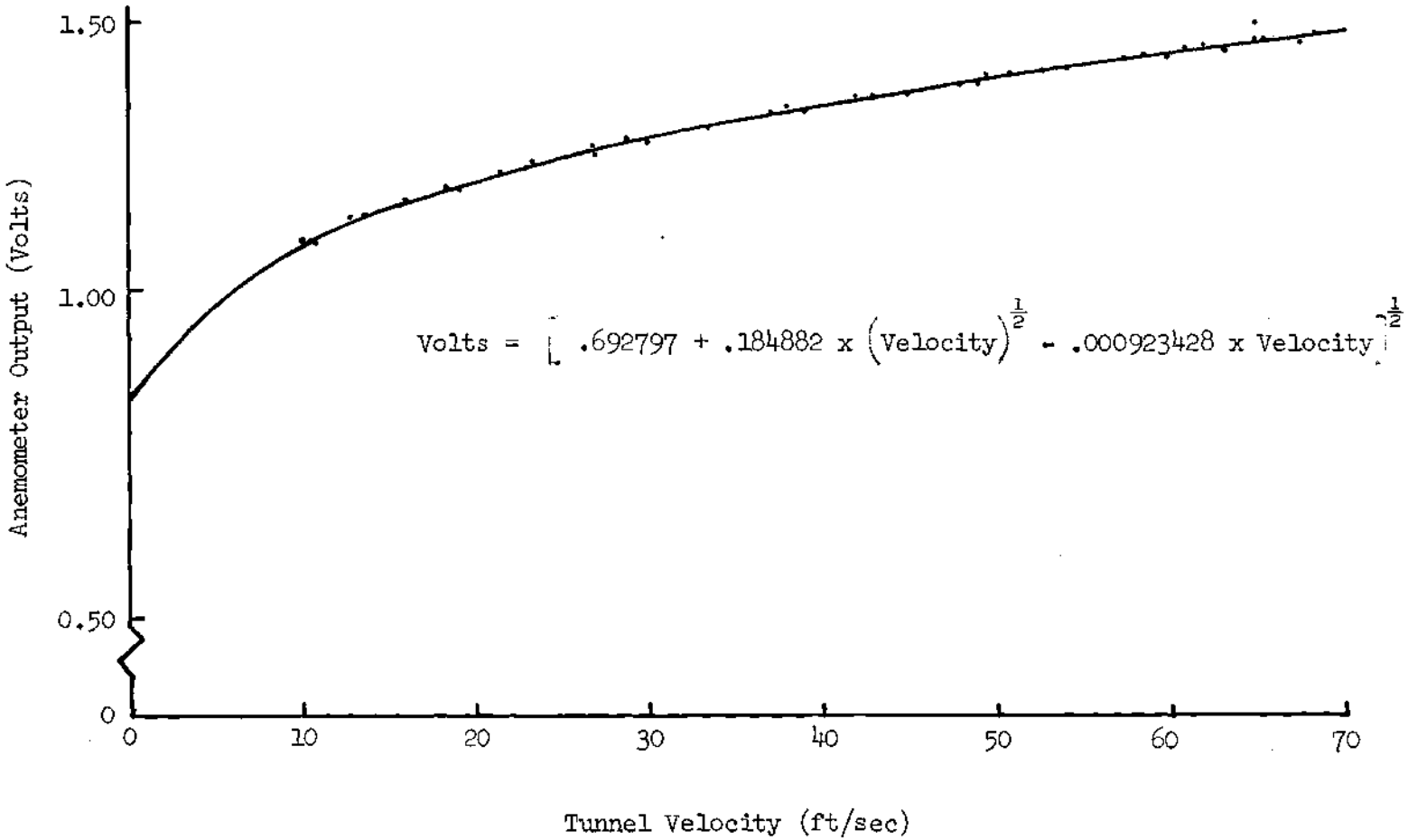

Figure 2-7. Hot Wire Calibration Curve

Gust Generator Performance

The electronic equipment used to measure the gust double-amplitude is shown in Figure 2-8. The x-y plotter used in the calibration tests was a Hewlett Packard Model No. 7001A. The oscilloscope, which was used to monitor and photograph the gust-waveform, was a Tektronix, dual-trace oscilloscope, Model No. 533A. The electronic counter used to determine the vane RPM was a General Radio, Model No. 1192-B.

After the turn-on procedures for the hot wire were completed, the zero-velocity voltage from the anemometer was used to calibrate the x-y plotter. Then, with the gust generator vanes in a horizontal position, the wind tunnel was turned on, producing a hot wire voltage dependent on the tunnel velocity. The hot wire was rotated to obtain a maximum voltage reading on the digital voltmeter. The hot wire was then clamped in place and the wind tunnel turned off.

General Survey of the Gust Field

A survey was taken to determine the quality of the gust velocity produced by the gust generator. Several effects were of particular interest: the effects on the waveform caused by distance from the gust generator vanes; the change in waveform over the tunnel cross-section; and the effects of mean airspeed and gust frequency on the shape of the waveform.

As mentioned previously, there were eighteen holes drilled in the plywood sidewall. These holes were spaced vertically in groups of three. The holes were covered by plugs which could be removed or replaced, as required. Each group represented a test station, consisting

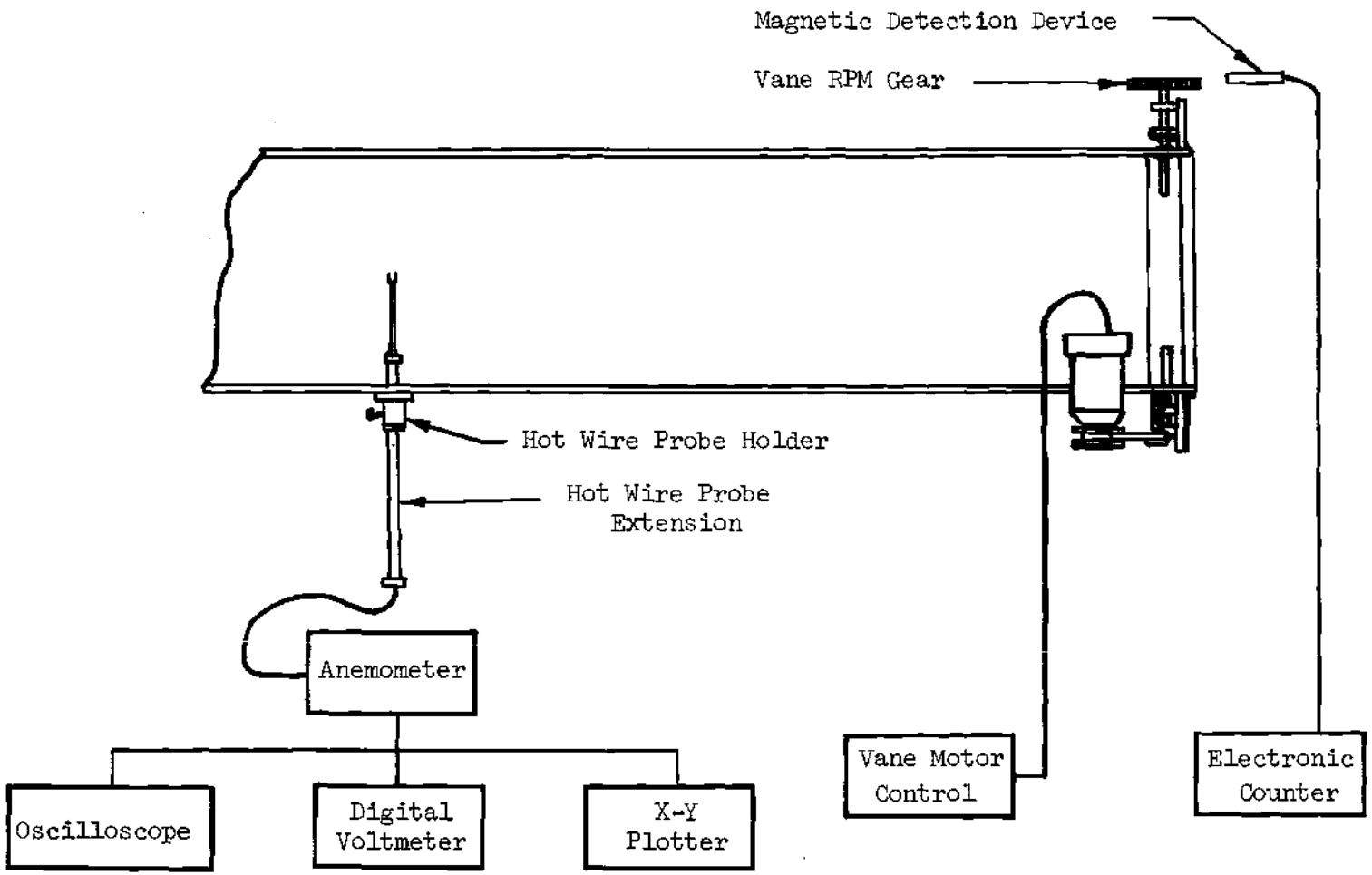

Figure 2-8. Electronic Equipment Used for Gust Velocity Survey

of a total of nine test points (Figure 2-9). The test stations were numbered from 1 to 6 from the vanes proceeding in the upstream direction. Each hole represented three cross section test points: two 9 inches from either tunnel wall, and one on the tunnel centerline. Cross-sectional test-points were numbered from 1 to 9 from the west side of the tunnel towards the opposite side and from the top to the bottom (see Figure 2-8). A particular test point in the tunnel was then designated by its station number and cross section number (i.e. 6/5).

The gust waveform was obtained from the hot wire probe and anemometer which were connected both to an x-y plotter and an oscilloscope. The oscilloscope and the plotter were used to monitor the waveform and check for any stalling of the tunnel fan caused by the operation of the gust generator. The oscilloscope was also used to obtain a permanent record of the velocity waveform by photographing the trace. Since neither the actual gust amplitude nor the mean-airspeed were necessary for this survey, the x-y plotter was not calibrated to a known tunnel airspeed.

For the survey, the 25% vanes were installed in the gust generator. Three tunnel-fan speeds were investigated (500, 650, and 800 RPM) together with three gust frequencies (40, 80, and 120 RPM). A full 9 test-point survey was performed at stations 6 and 2. Since there were no observed cross sectional effects on the gust waveform, the other stations were surveyed only on the tunnel centerline.

Upon completion of the tests using the 25% vanes, the 50% and 75% vanes were studied at one test-point (6/5). Several conclusions were drawn from the test results concerning the gust waveform produced

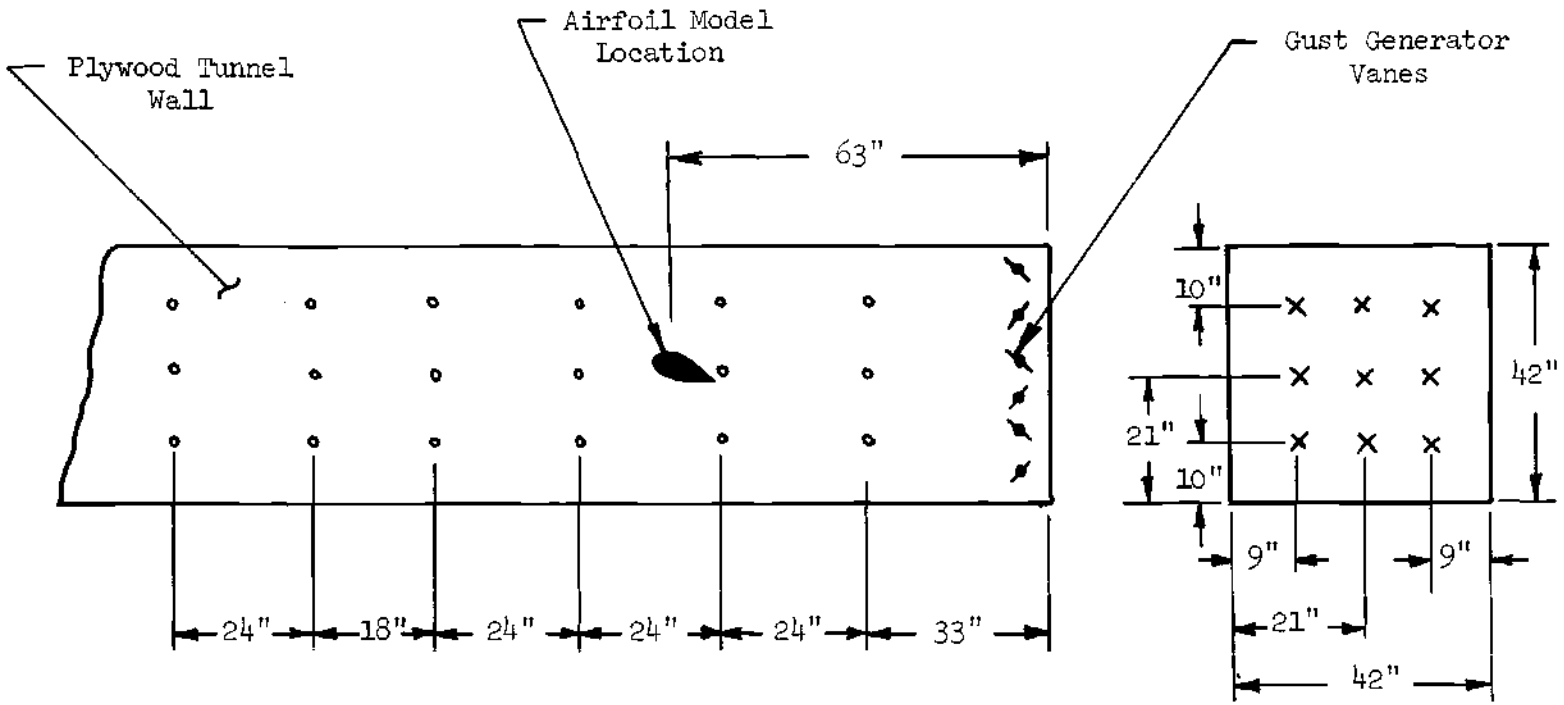

Figure 2-9. Test Station Locations for Gust Waveform Survey

by the gust generating mechanism (see Figures 2-10 to 2-12).

1) The hot wire output waveforms had fair to good shapes for all three gust frequencies.
2) The distance of the hot wire probe from the gust generator vanes did not appear to effect the shape of the gust waveform.
3) The waveform double amplitude increases with mean airspeed.
4) The waveform double amplitude decreases with increasing gust frequency.
5) The maximum tunnel airspeed was limited for a given set of vanes and was determined by either the stalling of the tunnel fan or the amount of tunnel wall vibration.
6) The minimum tunnel airspeed was limited by distortion of the waveform. Increasing the vane area decreased the lower airspeed limit.
7) Generation of low frequency gusts caused larger than normal loads on the tunnel structure at high airspeeds due to the increased time duration of the tunnel blockage during each vane cycle.

Calibration of the Gust Generator

To calibrate the gust generator, curves of gust double amplitude versus tunnel mean airspeed were developed. These curves were constructed from data obtained at three gust-frequencies (40, 80, and 120 RPM) and at various, randomly picked, tunnel airspeeds.

After the initial procedures were completed, the gust generator was started before turning on the wind tunnel. This sequence was

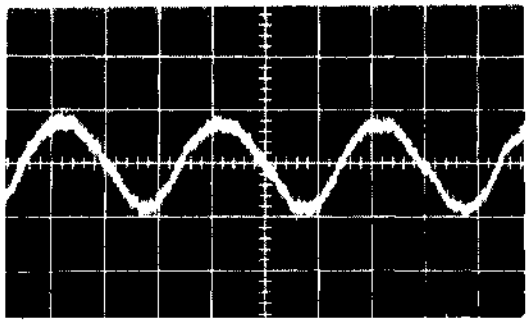

a) Gust Freq. = 40 RPM

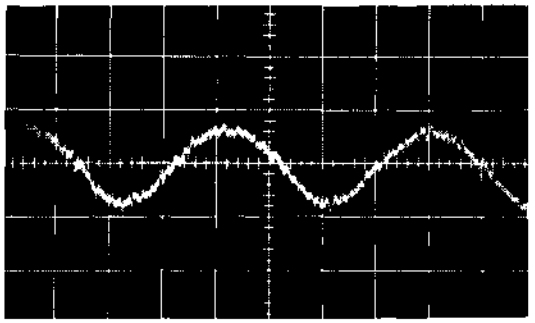

b) Gust Freq. = 80 RPM

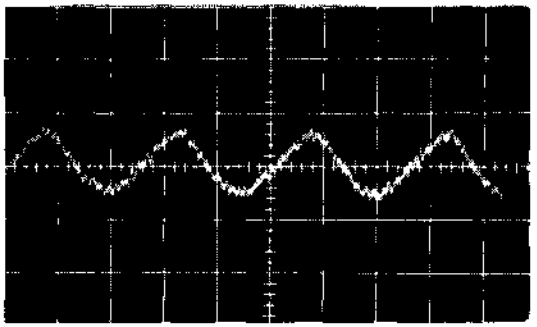

c) Gust Freq. = 120 RPM

Figure 2-10. Axial Gust Waveform for 25% Vanes

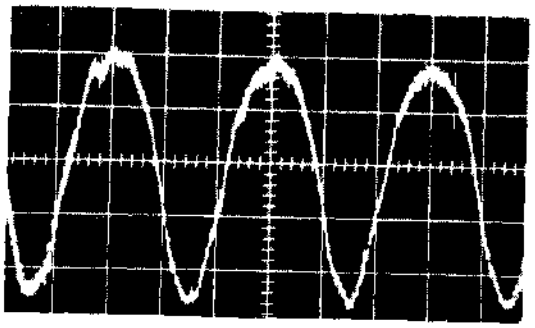

a) Gust Freq. = 40 RPM

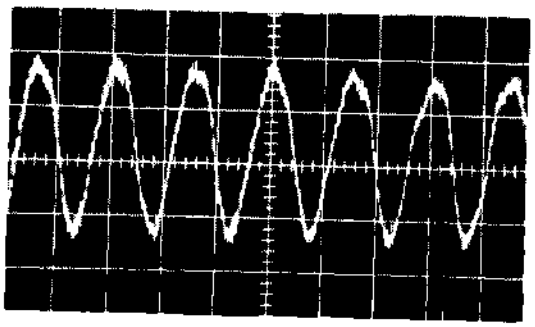

b) Gust Freq. = 80 RPM

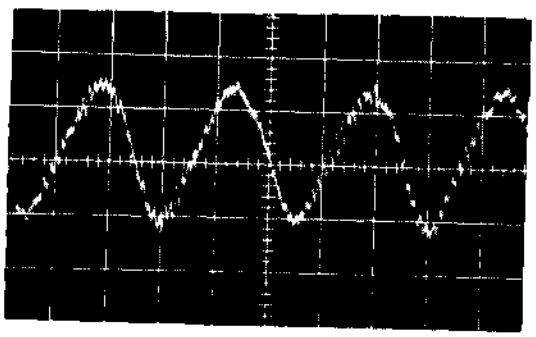

c) Gust Freq. = 120 RPM

Figure 2-11. Axial Gust Waveform for 50% Vanes

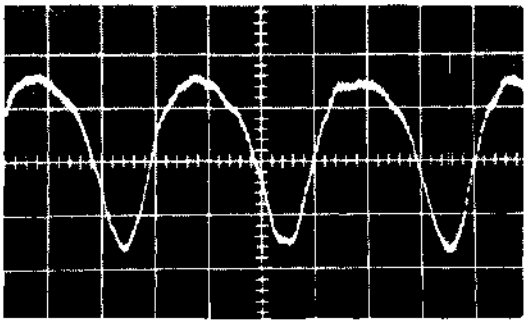

a) Gust Freq. = 40 RPM

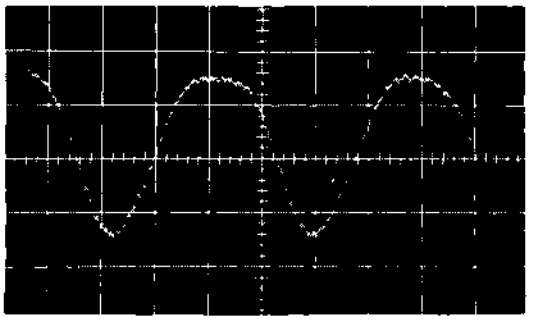

b) Gust Freq. = 80 RPM

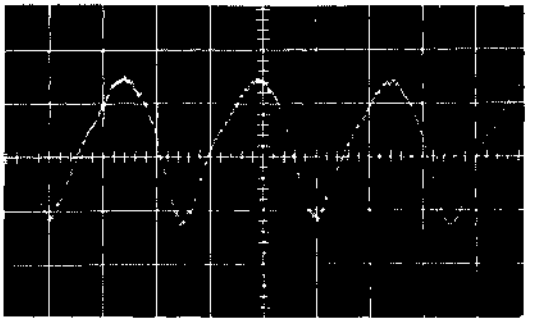

c) Gust Freq. = 120 RPM

Figure 2-12. Axial Gust Waveform for 75% Vanes

essential in order to protect the gust generator mechanism from the effects of steady aerodynamic loading. The gust generator was set at the desired frequency using the electronic counter. Different airspeeds were picked at random. A separate trace was made on the x-y plotter for each airspeed. The maximum airspeeds picked were determined by the set of vanes installed in the gust generator. Several test runs were made at each gust frequency with 6 random airspeeds for each test run. These experiments were repeated for each gust frequency and for all three sets of vanes.

The x-y plotter traces were then examined to obtain the maximum and minimum voltage of the gust waveform corresponding to each random airspeed. These pairs of voltages were recorded for each airspeed and separated into groups according to gust frequency and the particular set of gust generator vanes that was used during the tests.

A computer program was developed which converted the maximum and minimum voltages into maximum and minimum airspeeds by making use of the hot wire calibration curve. The mean airspeed was taken as the average of these two extreme velocities. The program also determined the gust double amplitudes and the percentage of mean speed for each of the double amplitudes. For these data, plots were constructed of the gust double-amplitude versus mean-airspeed for the three gust frequencies and the three different sets of vanes (Figures 2-13 and 2-15). Experimental work performed by J. A. Miller using a similar facility at the Naval Post Graduate School [20] has also indicated that the gust double amplitude is a function of gust frequency, tunnel speed, and vane width.

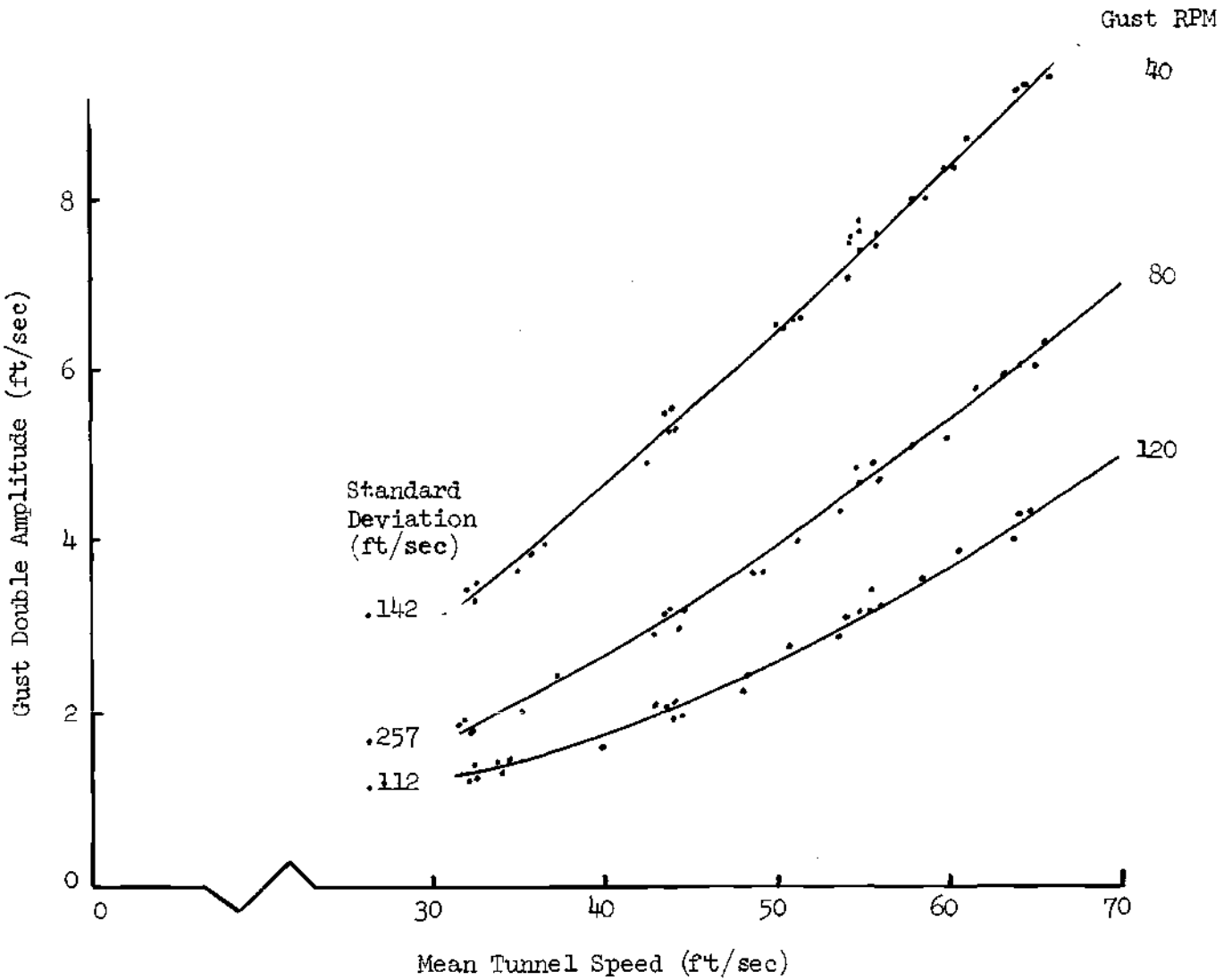

Figure 2-13. Least Squares Curve Fits of Experimental Data for the 25% Gust Generator Vanes

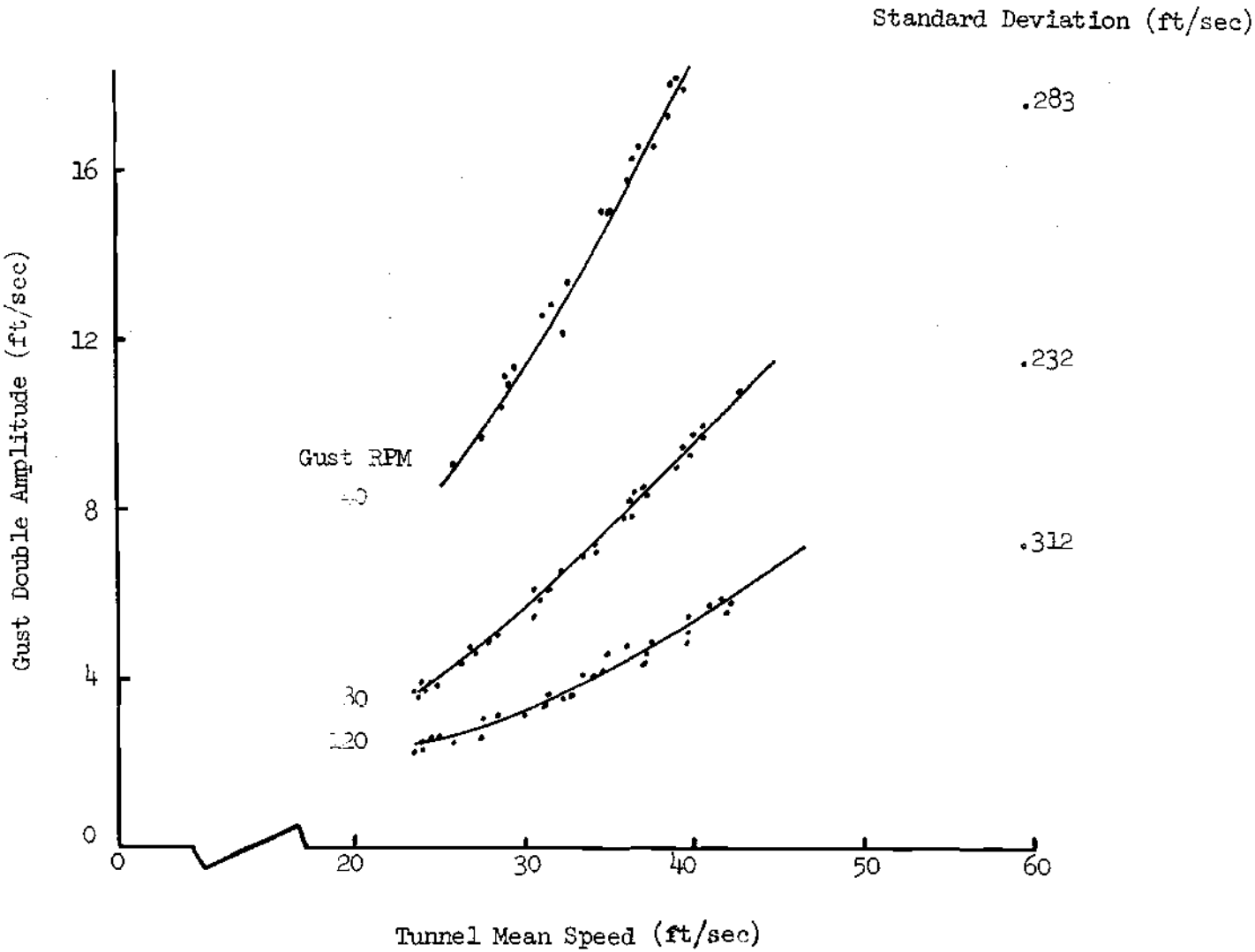

Figure 2-14. Least Squares Curve Fits of Experimental Data for the 50% Gust Generator Vanes

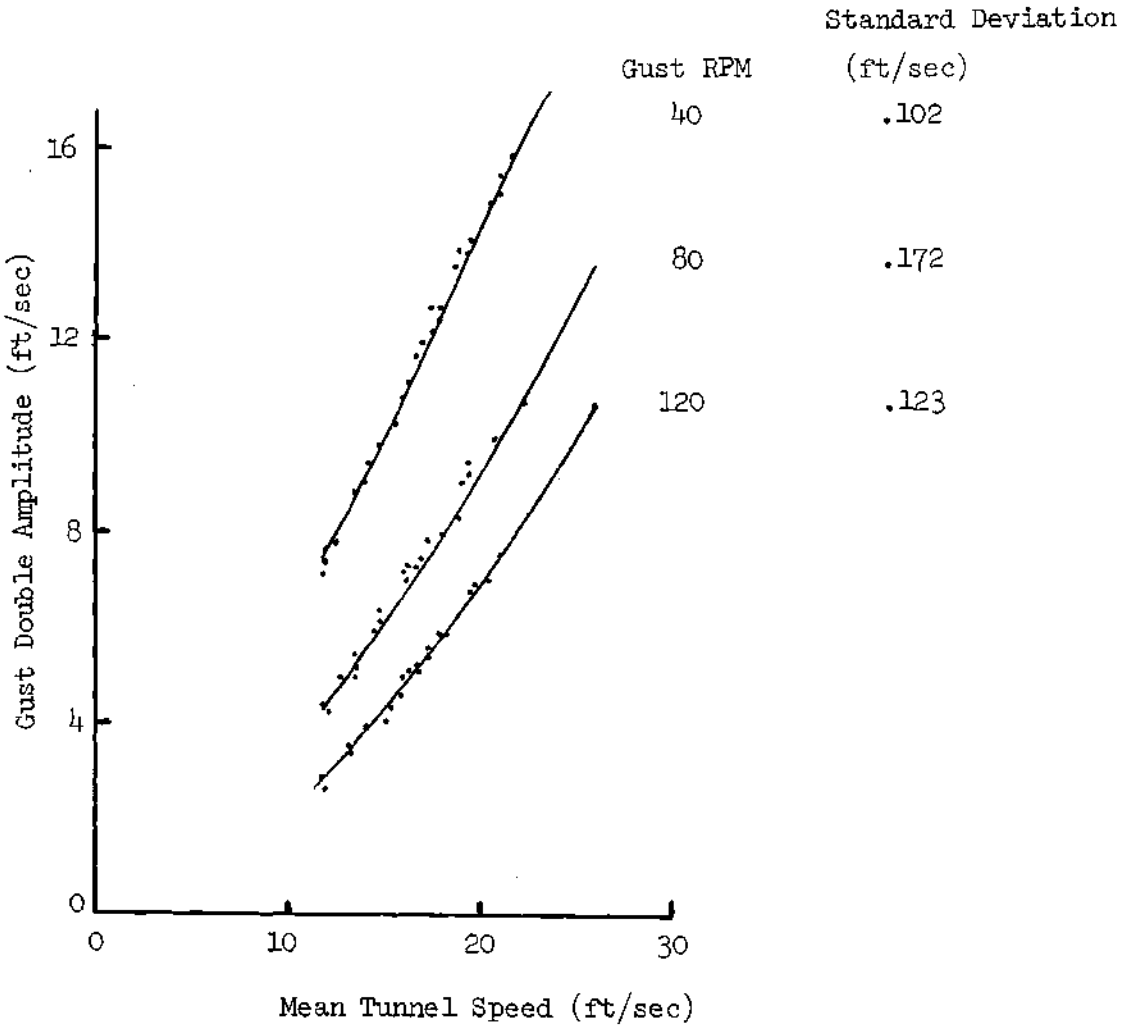

Figure 2-15. Least Squares Curve Fits of Experimental Data for the 75% Gust Generator Vanes

Since some scatter of the calibration data occurred, a computer program was used to determine first through fourth order least square curves which fit the double amplitude versus mean airspeed data. The standard deviation for each curve fit was also calculated. The curves with the smallest standard deviation were then chosen as the calibration for the gust generator at each of the three gust frequencies and for the three sets of vanes. These curves are plotted together with the experimental data in Figures 2-13 to 2-15. The equations for each set of vanes are given in Tables 2-1 through 2-3.

The calibration data were replotted in terms of gust amplitude ratio versus mean tunnel speed, where the gust amplitude ratio is defined as:

$$A_R = \text{gust double amplitude/mean tunnel speed} \qquad (2\text{-}3)$$

These experimental data are shown plotted versus tunnel airspeed in Figures 2-16 through 2-18, together with calculated values of the amplitude ratio obtained from the appropriate least squares calibration curve for each gust frequency.

Additional curves for intermediate values of gust frequency were obtained at intervals of 10 RPM by a cross-plotting technique (see Appendix A). The resulting second order curves are shown plotted in Figures 2-19 through 2-21. Tables 2-4 through 2-6 give the equations of these curves.

Table 2-1. Least Squares Curve Fits for 25% Vanes

Gust Freq.	Gust Double Amplitude as Function of Mean Velocity
40 RPM	$D_a(V_o) = -1.64306 + .141153 \times V_o + 4.32421 \times 10^{-4} \times V_o^2$
80 RPM	$D_a(V_o) = -2.53367 + .174024 \times V_o - 1.74551 \times 10^{-3} \times V_o^2 + 1.74799 \times 10^{-5} \times V_o^3$
120 RPM	$D_a(V_o) = 4.1410 - .248137 \times V_o + 5.97936 \times 10^{-3} \times V_o^2 - 3.24131 \times 10^{-5} \times V_o^2$

Table 2-2. Least Squares Curve Fits for 50% Vanes

Gust Freq.	Gust Double Amplitude as Function of Mean Velocity
40 RPM	$D_a(V_o) = -4.03592 + .379948 \times V_o + 4.76418 \times 10^{-3} \times V_o^2$
80 RPM	$D_a(V_o) = 3.50492 - .336256 \times V_o + .017976 \times V_o^2 - 1.42843 \times 10^{-4} \times V_o^3$
120 RPM	$D_a(V_o) = 9.61396 - .790608 \times V_o + .025592 \times V_o^2 - 2.11127 \times 10^{-4} \times V_o^3$

Table 2-3. Least Squares Curve Fits for 75% Vanes

Gust Freq.	Gust Double Amplitude as Function of Mean Velocity
40 RPM	$D_a(V_o) = 10.7375 - 1.76713 \times V_o + .163745 \times V_o^2 - 3.29981 \times 10^{-3} \times V_o^3$
80 RPM	$D_a(V_o) = - 2.75527 + .557904 \times V_o + 2.47581 \times 10^{-3} \times V_o^2$
120 RPM	$D_a(V_o) = - 3.19315 + .582807 \times V_o - .01079 \times V_o^2 + 3.35512 \times 10^{-4} \times V_o^3$

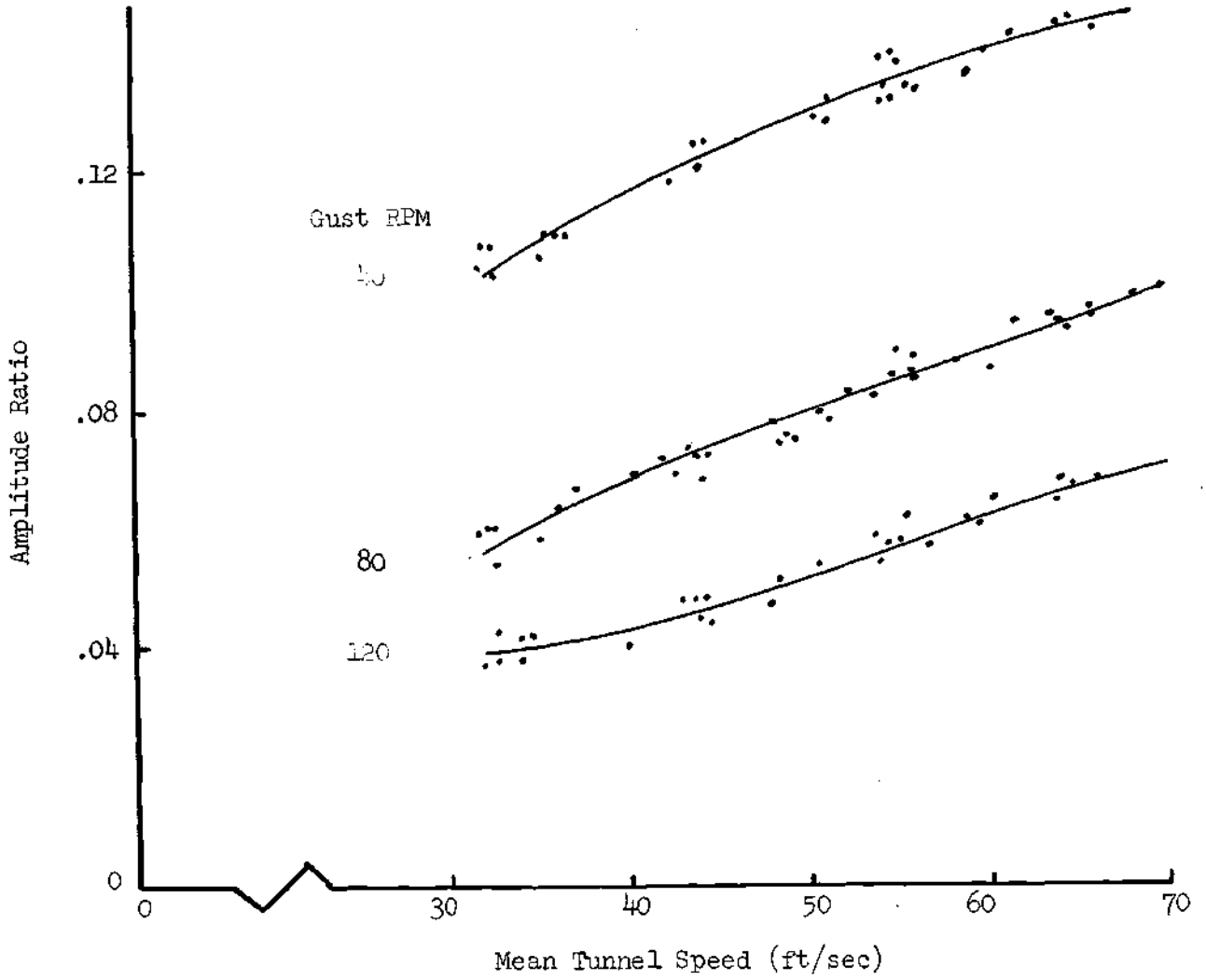

Figure 2-16. Gust Amplitude Ratio for the 25% Gust Generator Vanes

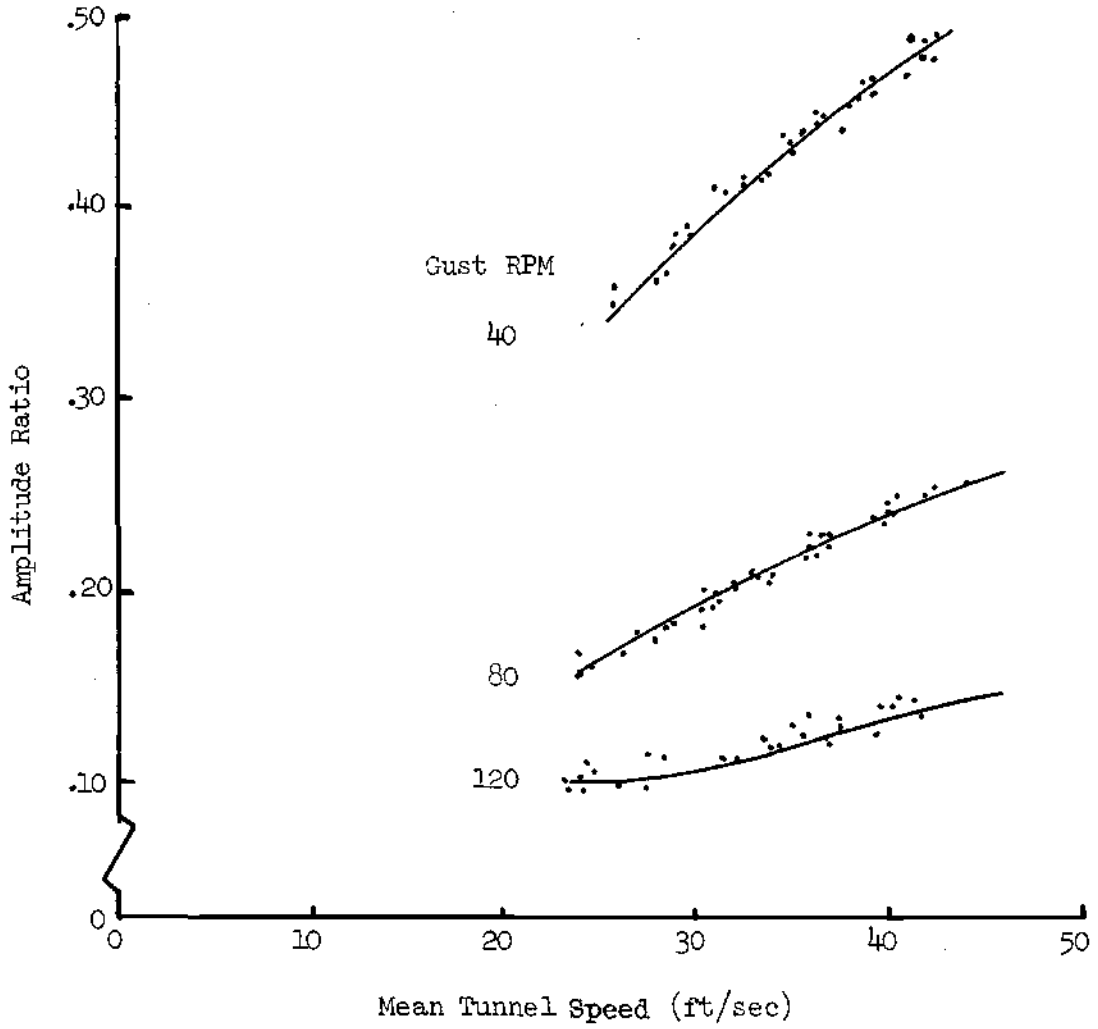

Figure 2-17. Gust Amplitude Ratio for the 50% Gust Generator Vanes

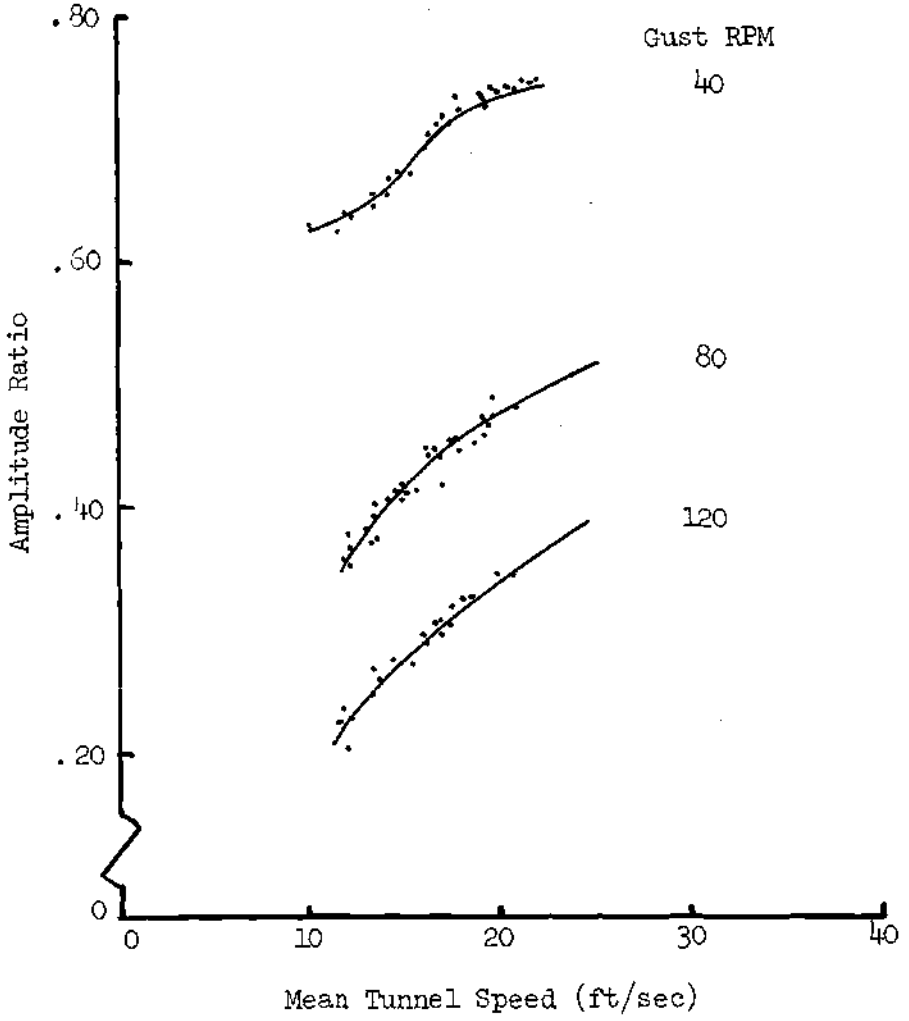

Figure 2-18. Gust Amplitude Ratio for 75% Vanes

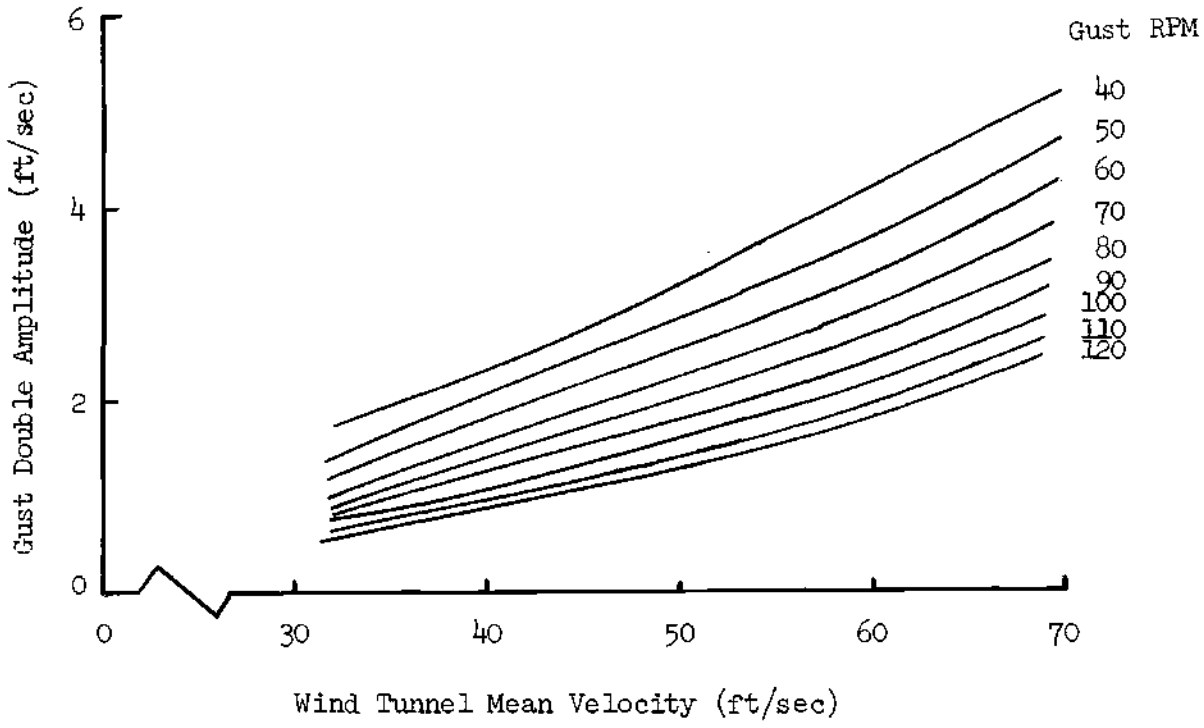

Figure 2-19. Gust Generator Calibration Curves for 25% Vanes Obtained from Cross-Plotted Data

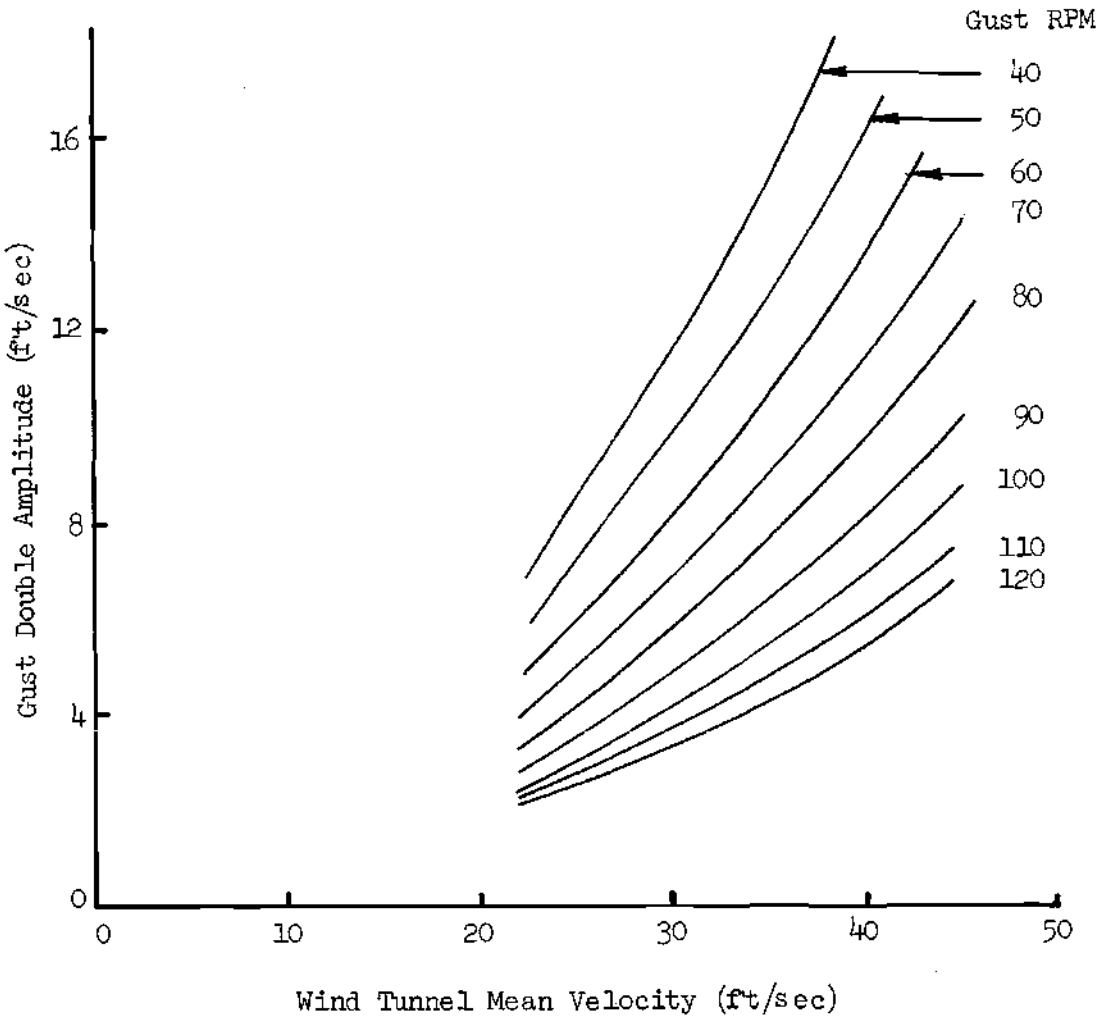

Figure 2-20. Gust Generator Calibration Curves for 50% Vanes Obtained from Cross-Plotted Data

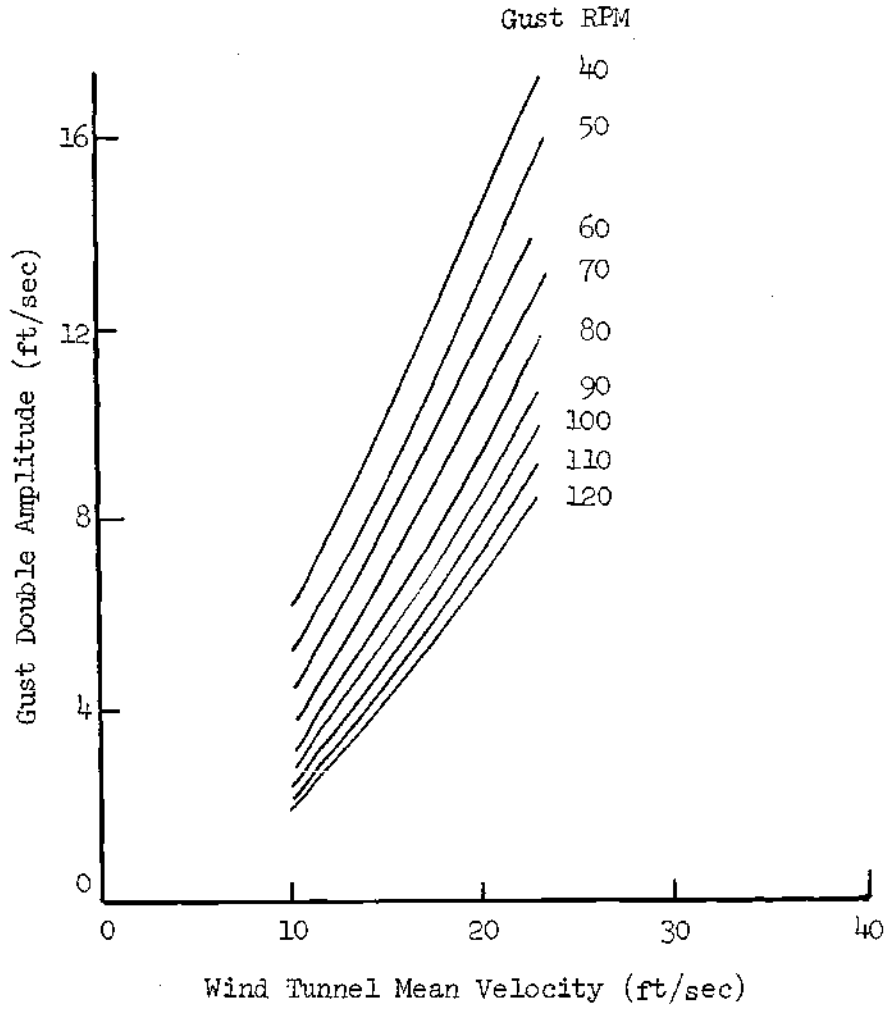

Figure 2-21. Gust Generator Calibration Curves for 75% Vanes Obtained from Cross-Plotted Data

Table 2-4. Operational Curves for Gust Generator Facility - 25% Vanes

Gust Freq.	Gust Double Amplitude as Function of Mean Velocity
20 RPM	$D_a(V_o) = -1.6430575 + .14115348 \times V_o + 4.3244 \times 10^{-4} \times V_o^2$
25 RPM	$D_a(V_o) = -1.4177886 + .11688832 \times V_o + 5.3495 \times 10^{-4} \times V_o^2$
30 RPM	$D_a(V_o) = -1.1897665 + .09440891 \times V_o + 6.2917 \times 10^{-4} \times V_o^2$
35 RPM	$D_a(V_o) = -.95894423 + .07371329 \times V_o + 7.1512 \times 10^{-4} \times V_o^2$
40 RPM	$D_a(V_o) = -.72554885 + .0548108 \times V_o + 7.927 \times 10^{-4} \times V_o^2$
45 RPM	$D_a(V_o) = .48938835 + .03768947 \times V_o + 8.6202 \times 10^{-4} \times V_o^2$
50 RPM	$D_a(V_o) = -.25032848 + .02235607 \times V_o + 9.2304 \times 10^{-4} \times V_o^2$
55 RPM	$D_a(V_o) = -.00866049 + 8.81026 \times 10^{-3} \times V_o + 9.7574 \times V_o^2$
60 RPM	$D_a(V_o) = .2357717 - 2.95025 \times 10^{-3} \times V_o + 1.02015 \times 10^{-3} \times V_o^2$

Table 2-5. Operational Curves for Gust Generator Facility - 50% Vanes

Gust Freq.	Gust Double Amplitude as Function of Mean Velocity
20 RPM	$D_a(V_o) = -4.0357683 + .37993857 \times V_o + 4.7643 \times 10^{-3} \times V_o^2$
25 RPM	$D_a(V_o) = - 3.3875274 + .30838328 \times V_o + 4.44674 \times 10^{-3} \times V_o^2$
30 RPM	$D_a(V_o) = - 2.6882441 + .23926974 \times V_o + 4.22114 \times 10^{-3} \times V_o^2$
35 RPM	$D_a(V_o) = - 1.9380393 + .1729055 \times V_o + 4.08737 \times 10^{-3} \times V_o^2$
40 RPM	$D_a(V_o) = - 1.1369947 + .10899578 \times V_o + 4.04536 \times 10^{-3} \times V_o^2$
45 RPM	$D_a(V_o) = - .28496543 + .04763146 \times V_o + 4.09525 \times 10^{-3} \times V_o^2$
50 RPM	$D_a(V_o) = .61782064 - .01117319 \times 4.23683 \times 10^{-3} \times V_o^2$
55 RPM	$D_a(V_o) = 1.5716553 - .0674365 \times V_o + 4.47036 \times 10^{-3} \times V_o^2$
60 RPM	$D_a(V_o) = 2.576344 - .12114626 \times V_o + 4.79566 \times 10^{-3} \times V_o^2$

Table 2-6. Operational Curves for Gust Generator Facility - 75% Vanes

Gust Freq.	Gust Double Amplitude as Function of Mean Velocity
20 RPM	$D_a(V_o) = -1.3002738 + .67473333 \times V_o + 5.35369 \times 10^{-3} \times V_o^2$
25 RPM	$D_a(V_o) = -1.8852429 + .6564481 \times V_o + 4.08432 \times 10^{-3} \times V_o^2$
30 RPM	$D_a(V_o) = -2.3227748 + .63088671 \times V_o + 3.18135 \times 10^{-3} \times V_o^2$
35 RPM	$D_a(V_o) = -2.6127845 + .59803768 \times V_o + 2.64515 \times 10^{-3} \times V_o^2$
40 RPM	$D_a(V_o) = -3.3495431 + .63540261 \times V_o + 8.548145 \times 10^{-5} \times V_o^2$
45 RPM	$D_a(V_o) = -2.7503898 + .5104972 \times V_o + 2.6724 \times 10^{-3} \times V_o^2$
50 RPM	$D_a(V_o) = -2.5980213 + .45581048 \times V_o + 3.2357 \times 10^{-3} \times V_o^2$
55 RPM	$D_a(V_o) = -2.2981115 + .39383368 \times V_o + 4.16584 \times 10^{-3} \times V_o^2$
60 RPM	$D_a(V_o) = -1.8464453 + .32421899 \times V_o + 5.46254 \times 10^{-3} \times V_o^2$

CHAPTER III

AIRFOIL MODEL AND DRIVE MECHANISM

Model Construction

The airfoil model was fabricated by bonding eleven balsa wood blocks, side by side, onto a 7/8 inch diameter shaft. Each block was four inches wide in the span direction, nine inches long in the chord direction, and $1\frac{1}{2}$ inches in thickness (see Figure 3-1).

The model was constructed by first drilling a 7/8 inch diameter clearance hole through each block in the spanwise direction, centered $2\frac{1}{2}$ inches aft of the leading edge. A keyway was then broached along each hole, facing the trailing edge of the model.

The steel shaft used for the model was 7/8 of an inch in diameter and 59 inches in length. A keyway was milled in the shaft along the whole length where the model was to be located. A mixture of polyester resin epoxy and chopped fiber glass filler was used to bond the balsa wood blocks to the steel shaft.

After coating the inside of the hole drilled in the block, the first piece of balsa wood was slipped over one end of the shaft. The block was positioned so that the wooden keyway was aligned with the keyway in the shaft. Epoxy was then poured into the rectangular hole formed by the two keyways. The remaining blocks were attached to the shaft, one at a time, in a similar manner. In addition, the interior blocks were coated with epoxy on both sides so that the adjoining

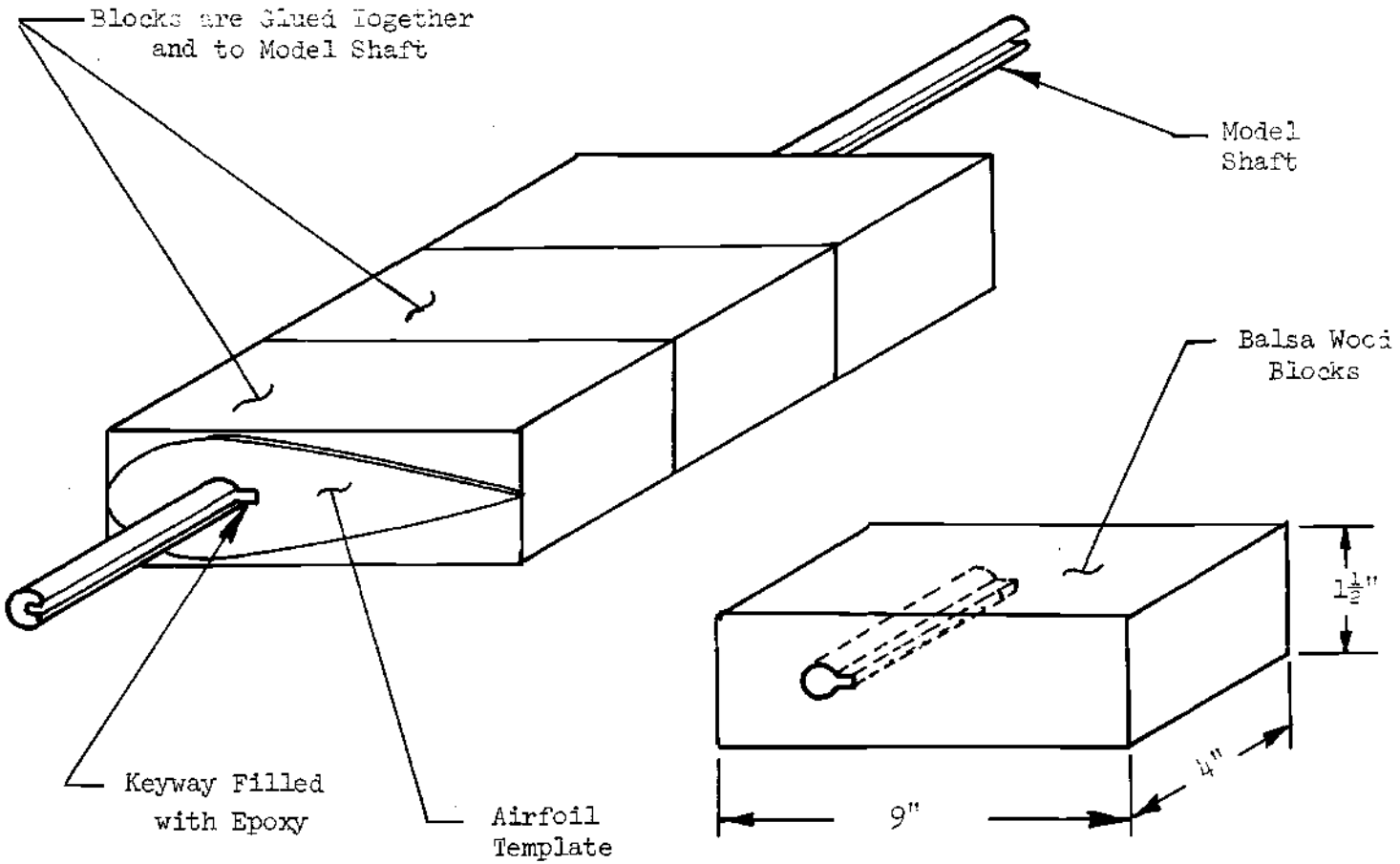

Figure 3-1. Airfoil Model Construction

surfaces of each block were bonded together.

The balsa wood was shaped to an NACA 0012 contour, with a nine inch chord and the shaft at the quarter chord point. This was accomplished by first bonding two 1/8 inch thick aluminum templates to each end of the model. Both templates had been shaped to the exact airfoil contour and keyed to the model shaft. The model was then placed in a lathe and the excess wood removed from the block using the templates as contour guides.

After the desired airfoil contour was obtained, the wooden surface was sealed with two coats of vinyl resin, sanded smooth, and then covered with two coats of flat black paint. The model was mass balanced by attaching two, rectangular brass bars to both ends of the model shaft. These bars were positioned so that they would be outside of the test section when the model was in the tunnel.

A B & K Model No. 306 accelerometer was installed in the model approximately $2\frac{1}{2}$ inches aft of the model shaft. This distance from the rotational axis was choosen so that the model accelerometer signal would be of the same approximate magnitude as the signal produced by the drive arm accelerometer. The airfoil accelerometer was secured in place by threading it into a small aluminum tab which had been inset into the balsa wood surface at one end of the model and welded to the aluminum template. The accelerometer cable was wrapped around the model shaft and taped securely into position to facilitate installation of the model into the wind tunnel.

Model Support System

Prior to installation of the airfoil in the wind tunnel, a portion of the plywood, west wall, where the model would be located, was replaced by a 4 x 7 foot section of one inch thick Plexiglas. While the main purpose of the Plexiglas was to permit flow visualization experiments, its greater thickness and rigidity also served to decrease tunnel wall deflections during testing. After the Plexiglas was in place, several steel braces were bolted to the top and bottom of the tunnel structure. The panel was held in position with inward pressure which was applied by threading screws horizontally through the steel braces. Finally, a 1-1/8 inch diameter clearance hole was drilled in the Plexiglas to accommodate the model shaft. This hole was located 63 inches upstream from the gust generator vanes and approximately 21 inches above the tunnel floor.

The model shaft was supported on both sides of the test section by main bearing assemblies located outside of the tunnel walls. Each bearing assembly consisted of two parts: a base and a center arm (see Figure 3-2). The center arm was pinned at one end of the base. At the opposite end a load cell was connected between the center arm and the base. The model shaft extended through a roller bearing which was located in the center arm, midway between the pin connection and the load cell. With the model supported in this manner, the output of each load cell represented approximately one quarter of the total lift force acting on the airfoil.

The lift acting on the airfoil was also obtained from strain

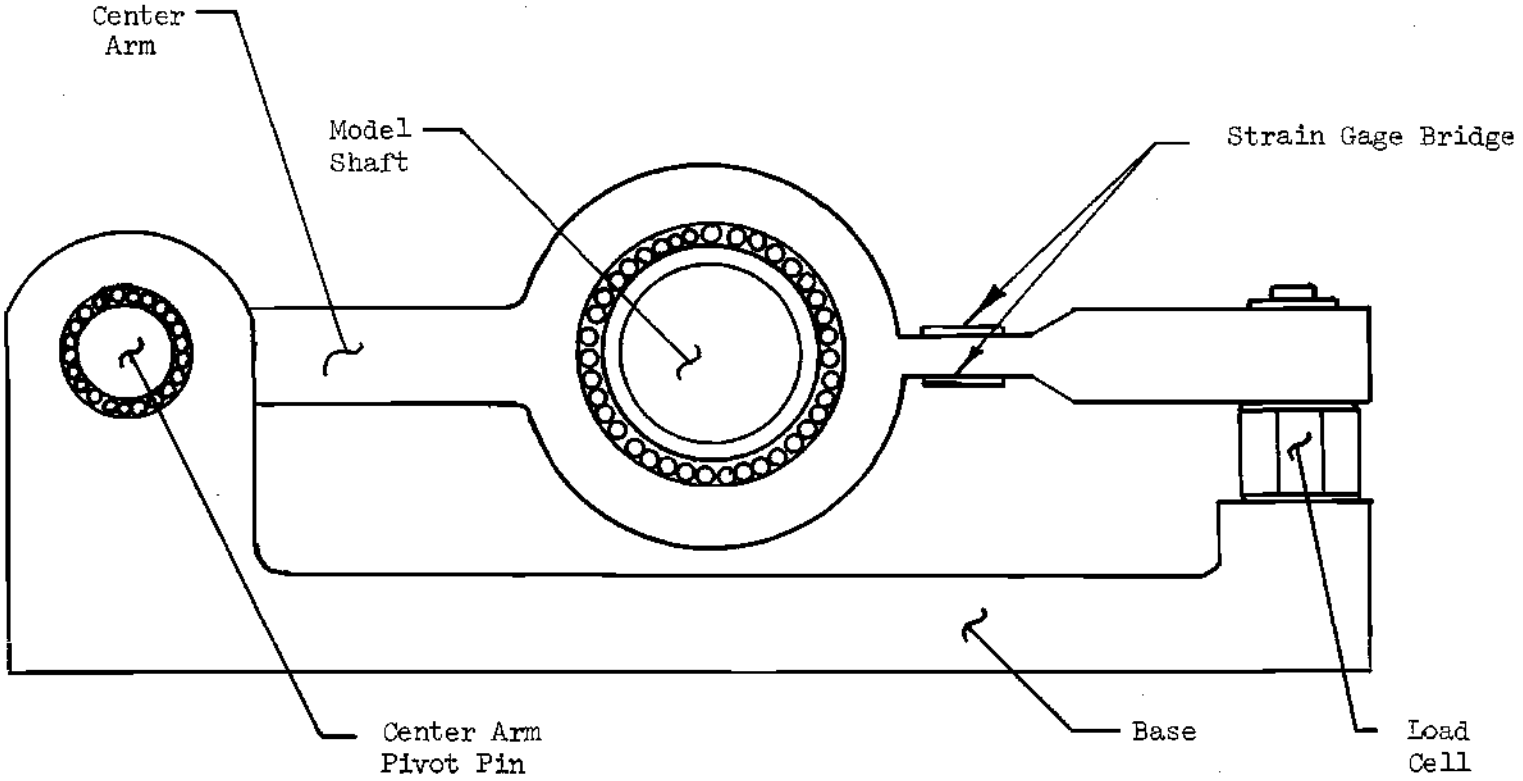

Figure 3-2. Main Bearing Assembly

gage bridges which were bonded to both center arms of the main bearing assemblies. Each bridge contained four active arms, two on top of the center arm, and two on the bottom (see Figure 3-2). The bridge circuit was connected so that the gages on the same side of the center arm were located on opposite arms of the strain gage bridge. This procedure produced the greatest sensitivity possible from the bridge circuit (see Figure 3-3).

A portion of both center arms was milled down to a thickness which would cause detectable surface strains during the aerodynamic loading. The strain gage bridges were located at this position on each center arm. The natural frequency of the knotched center arm was determined using a Galerkin technique to insure that oscillation frequencies of the airfoil would not excite a resonant condition in the main bearing assembly. In addition, the predicted vertical deflections of the center arms under maximum loading conditions were small enough to consider the model and supports as a one-degree-of-freedom system.

Due to the size of the tunnel wall deflections during certain operating conditions of the gust generator, the airfoil bearing supports and the oscillating mechanism could not be fastened directly to the test section walls. Consequently, the main bearing assemblies and the motor drive system were attached to the external tunnel structure in such a manner as to have a clearance on either side of the tunnel walls.

The base of the main bearing assembly on the west side (i.e., the idle side) was bolted to a trapizoidal frame constructed of welded, $2\frac{1}{2}$ x $2\frac{1}{2}$ inch steel angle iron (see Figures 3-4A and 3-4B). The frame

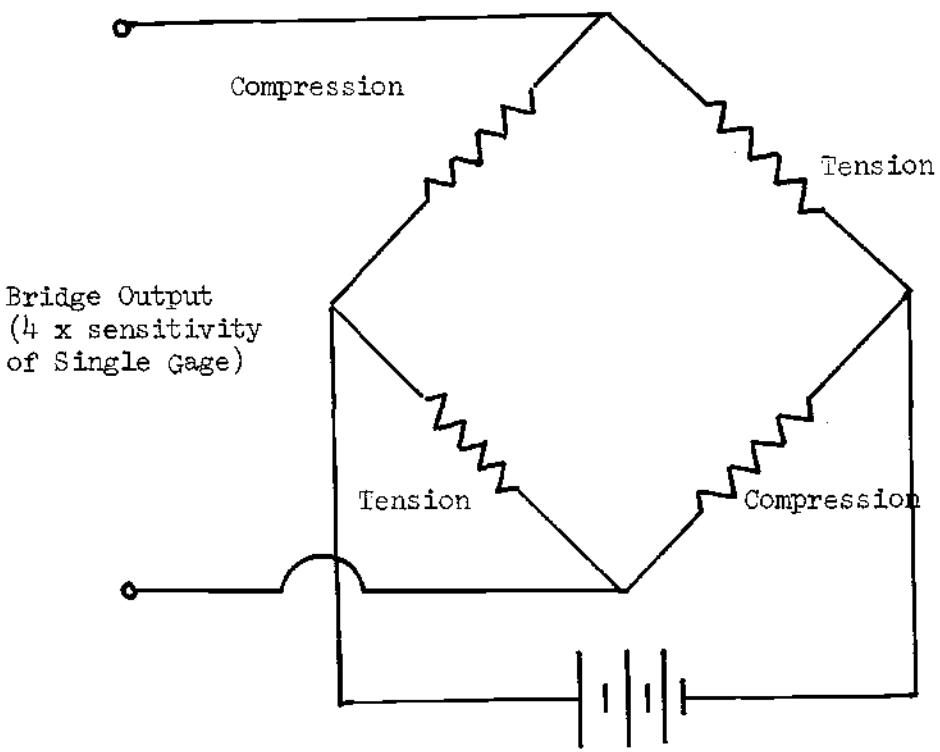

Figure 3-3. Strain Gage Bridge Circuitry

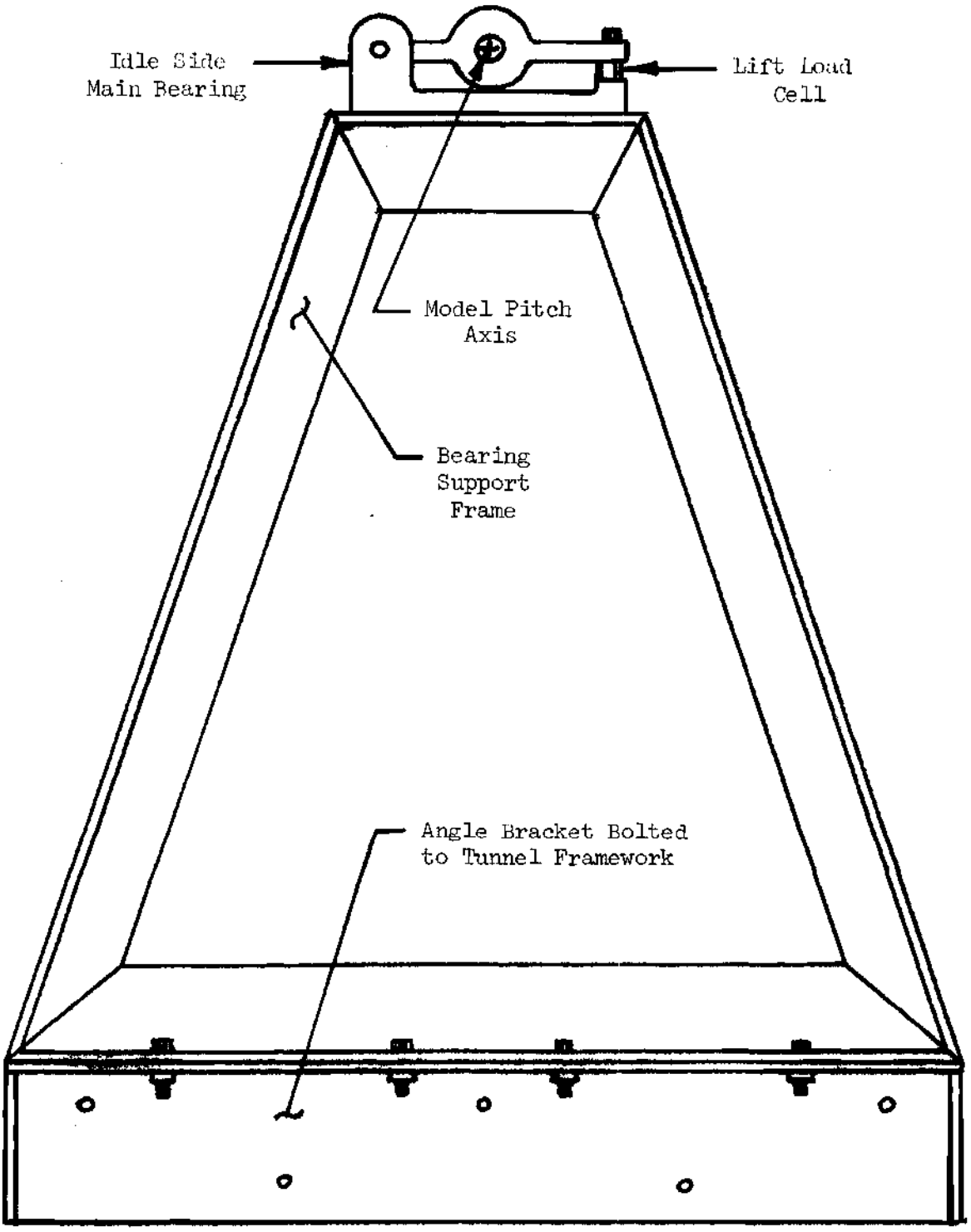

Figure 3-4A. Idle Side Support Frame (Front View)

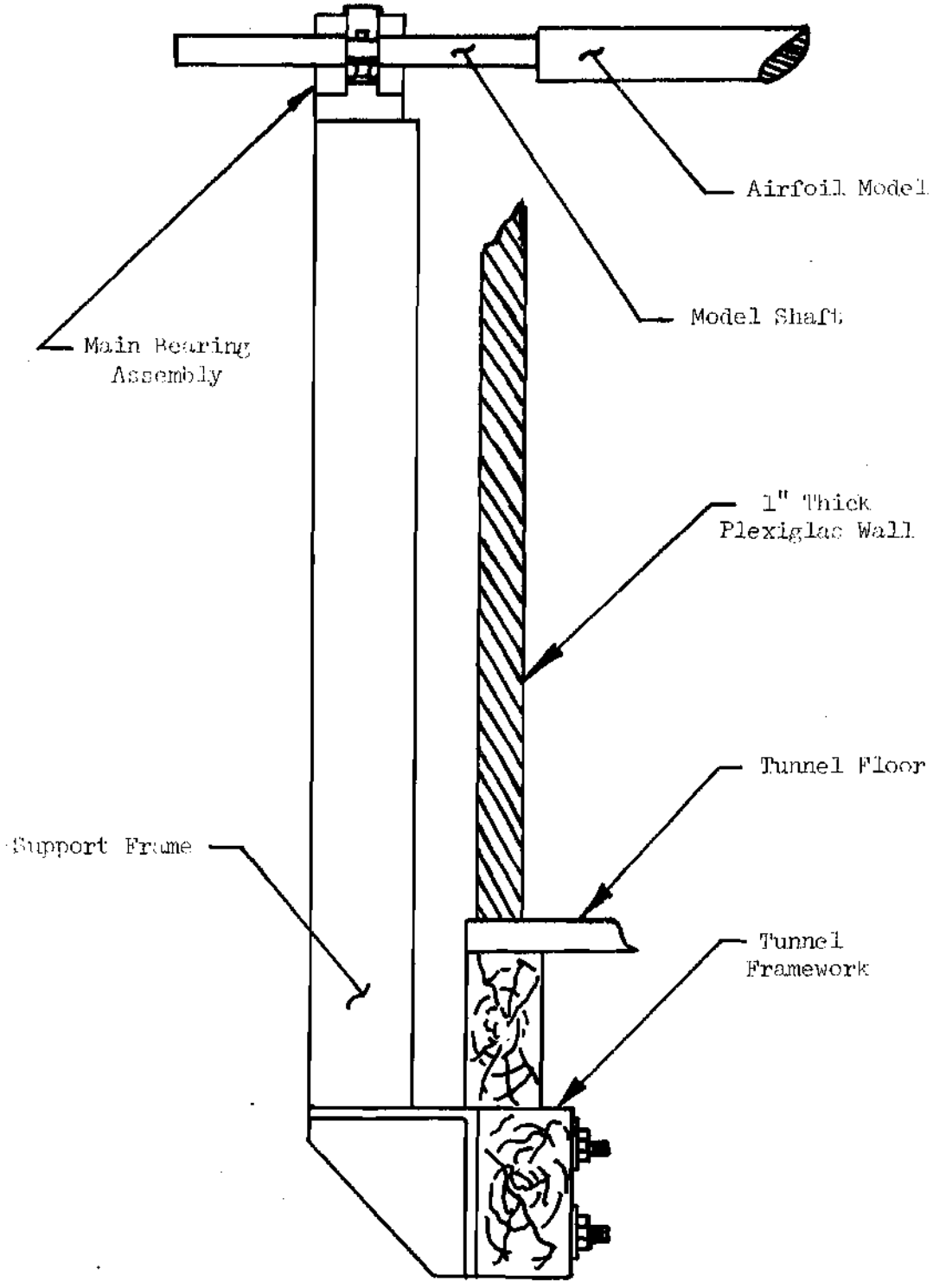

Figure 3-4B. Idle Side Support Frame (Side View)

in turn, was attached to a 4 x 4 inch piece of steel angle which had been bolted to the wind tunnel floor braces. The height of this supporting framework was adjusted so that the roller bearing located in the center arm of the main bearing assembly would be in line with the clearance hole in the Plexiglas.

The main bearing assembly on the east side (i.e., the drive side) and the motor drive system were both supported by a 20 x 24 x 1 inch aluminum base plate. The base plate was bolted to steel angles, which were then fastened to the external tunnel structure. The base of the bearing assembly was attached to a stand which had been constructed of one inch thick aluminum blocks, bolted to the base plate. The height of this stand and base plate combination from the tunnel floor, together with their location along the wind tunnel axis, assured that when the model was in position, the center line of the model shaft would be parallel to the tunnel floor and perpendicular with the tunnel axis.

The addition to the tunnel-wall clearance requirement, the airfoil model and its supporting system had to be designed so that the model could be removed from the wind tunnel or replaced when necessary with a minimum effort. To accomplish this, the model was installed and removed through a 3 x 10 inch rectangular hole cut out of the aluminum wall on the east side of the tunnel. When the airfoil was placed in the test section, the shaft was first guided through the clearance hole in the Plexiglas, and then through the roller bearing in the main bearing assembly. A 4 x 11 inch rectangular cover plate

with another 1-1/8 inch clearance hole was installed over the portion of the model shaft protruding outside of the east wall of the tunnel. Then the roller bearing in the second bearing assembly was slipped over the model shaft, and the base of this assembly was bolted to its base plate stand. The cover plate was designed so that when it was bolted in place, the surface of the plate inside of the tunnel was flush with the aluminum wall.

Model Oscillating Mechanism

The oscillating mechanism (see Figures 3-5A and 3-5B) for the airfoil model consisted of four major groups: the adjustment disks and linkages, the outer bearing assembly, the motor and crank group, and the drive rod and drive arm assembly. This drive system was designed to allow for variations in airfoil mean angle-of-attack, amplitude of oscillation, and frequency of oscillation. The oscillating mechanism was attached to the same base plate that supported the main bearing on the east side of the wind tunnel.

Two aluminum adjustment disks were used to change the model mean angle-of-attack. One disk was keyed directly to the end of the model shaft, while the other was attached to a linkage shaft. The two disks were mated using a recess and flange design in order to insure that the linkage shaft centerline was in exact alignment with the model shaft centerline. With the linkage shaft held in a reference position, the model angle-of-attack could be changed by first loosening four connecting screws between the adjustment disks, then setting the new mean angle, and finally clamping the disks together by retightening

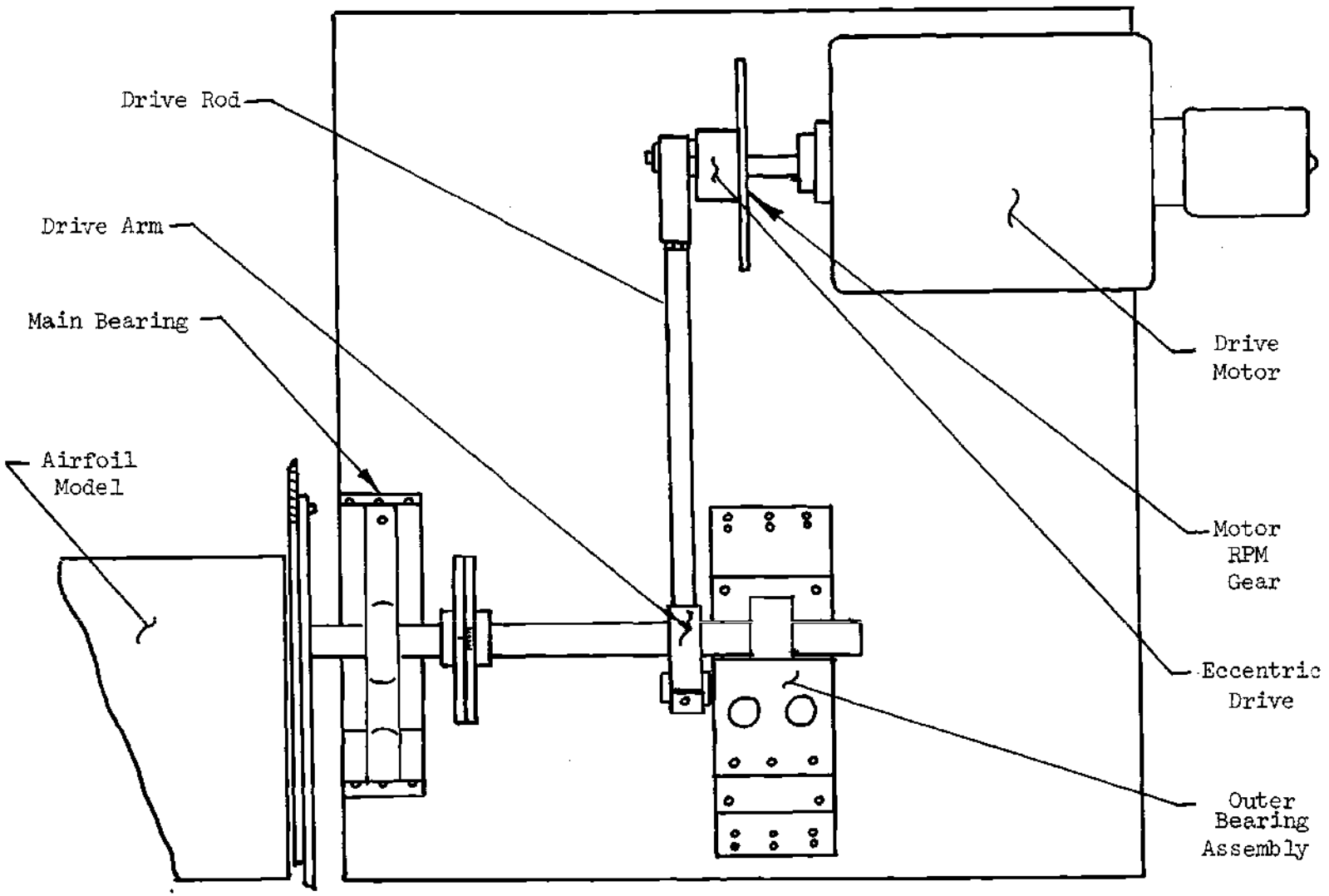

Figure 3-5A. Airfoil Oscillating Mechanism (Top View)

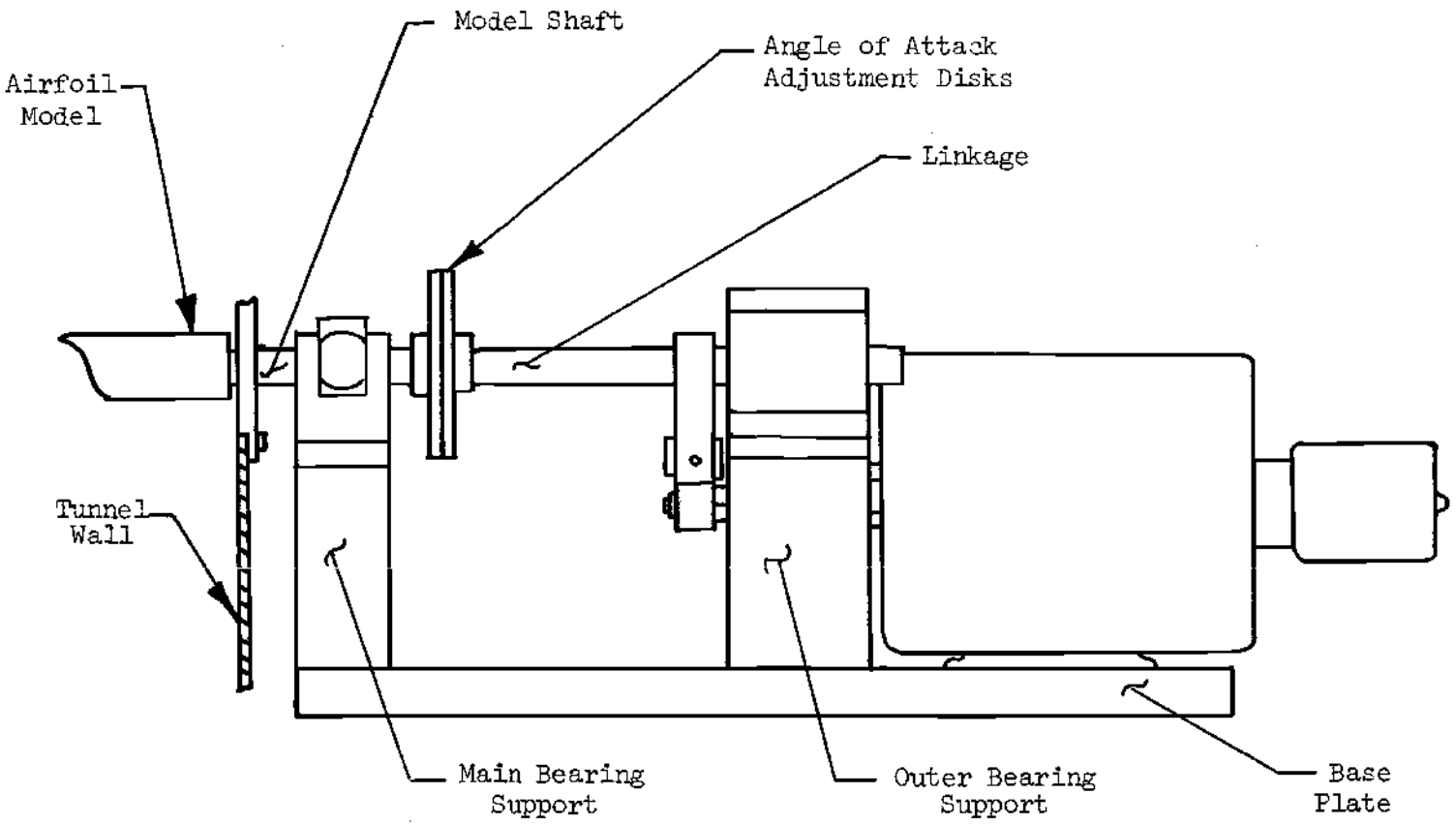

Figure 3-5B. Airfoil Oscillating Mechanism (Front View)

the connecting screws. This arrangement allowed variations of mean angle between minus twenty and plus twenty degrees.

Two types of linkages, each seven inches long and 7/8 of an inch in diameter, were used during the experiments. One linkage was a solid steel shaft which was used for rigid, forced oscillations of the airfoil. The other type of linkage consisted of elastic couplings, each formed from an aluminum shaft by milling away the center material to leave four connecting ribs (see Figure 3-6). The length, width, and thickness of the ribs determined the spring constant for each elastic linkage. An analytical method was used to estimate the values of these dimensions which would produce a specified natural frequency in pitch of the airfoil-linkage combination (see Appendix B). These elastic links were used during decaying oscillations and forced, elastic oscillations of the model.

With a linkage shaft installed in the drive system, the end of the linkage furtherest from the tunnel was supported by an outer bearing assembly (see Figure 3-7). This assembly prevented bending of the linkage about an axis perpendicular to the tunnel floor during forced oscillations of the airfoil. At the same time, the outer bearing permitted vertical motions of the shaft. The vertical motion allowed the main bearing assemblies to absorb the total lift force on the airfoil, assuming no frictional losses during vertical motion in the outer bearings.

The motor used to oscillate the airfoil was a Minarik, $\frac{1}{2}$ H.P., shunt motor with a maximum speed of 2500 RPM. The rotational motion

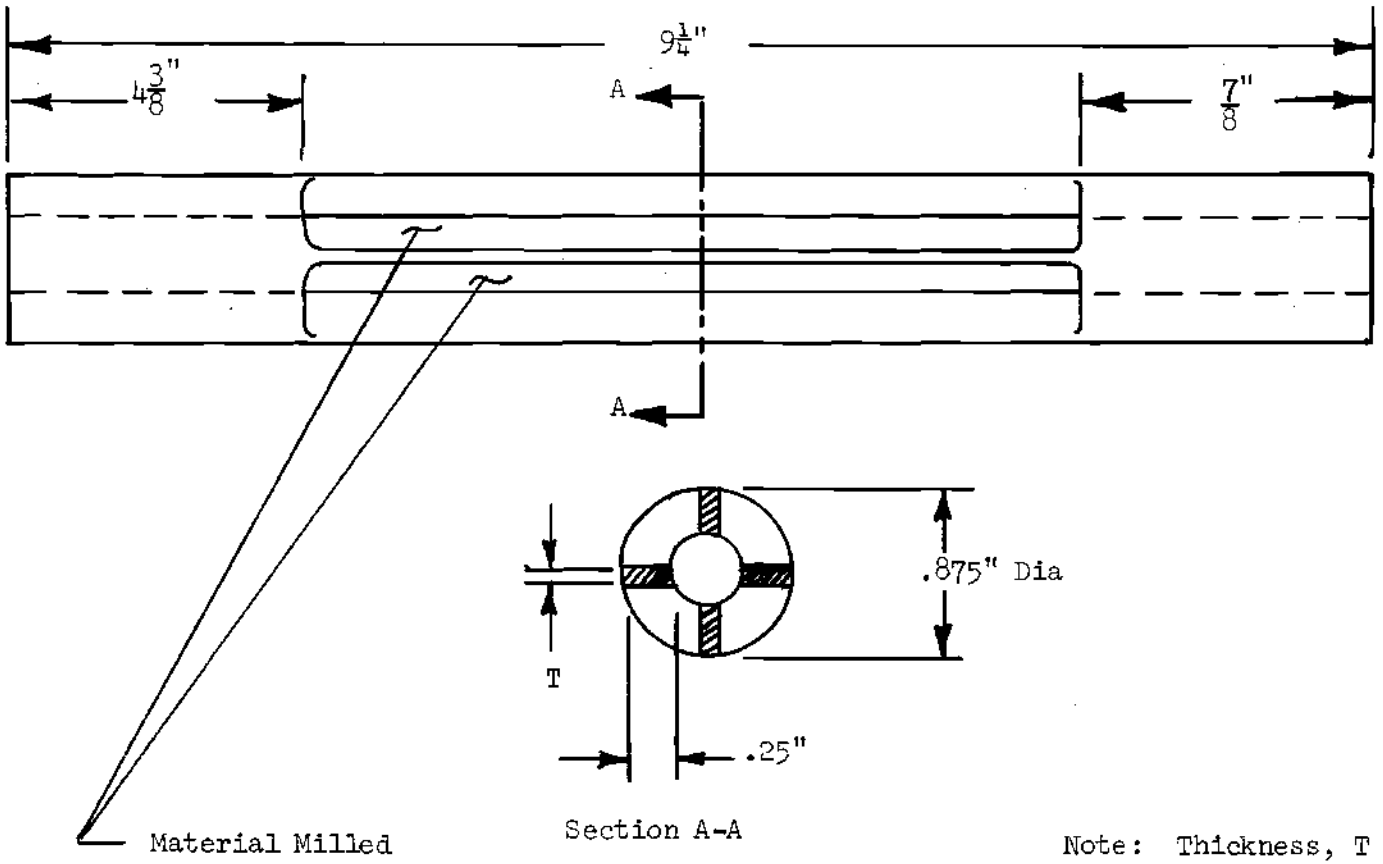

Figure 3-6. Typical Elastic Linkage

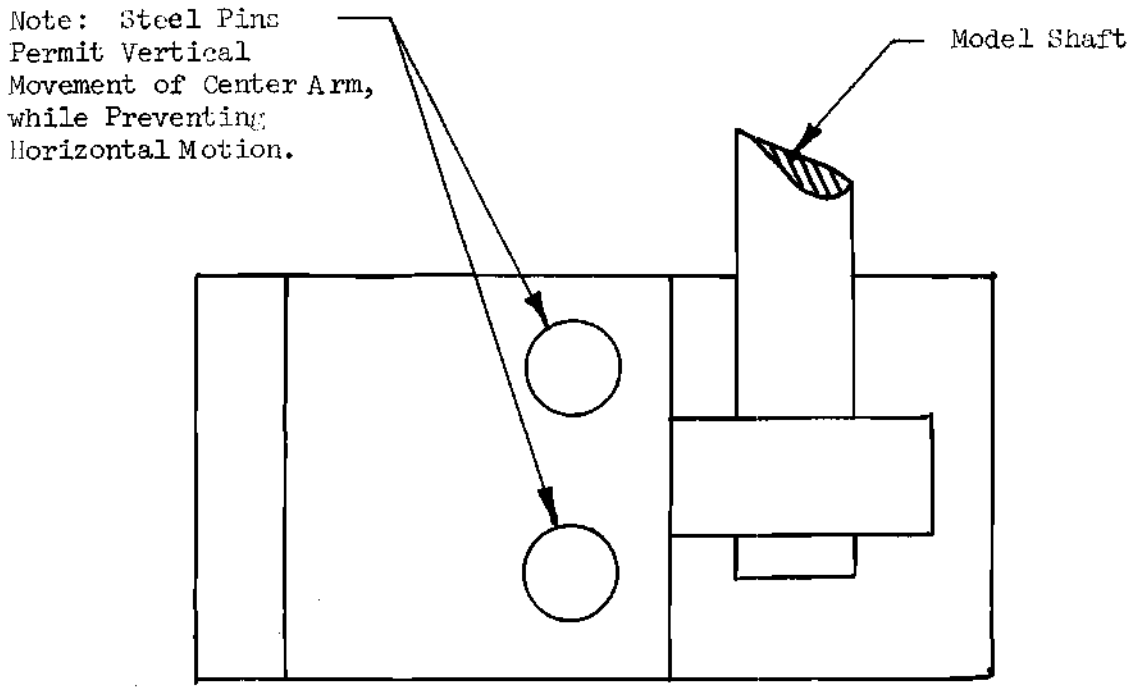

Top View

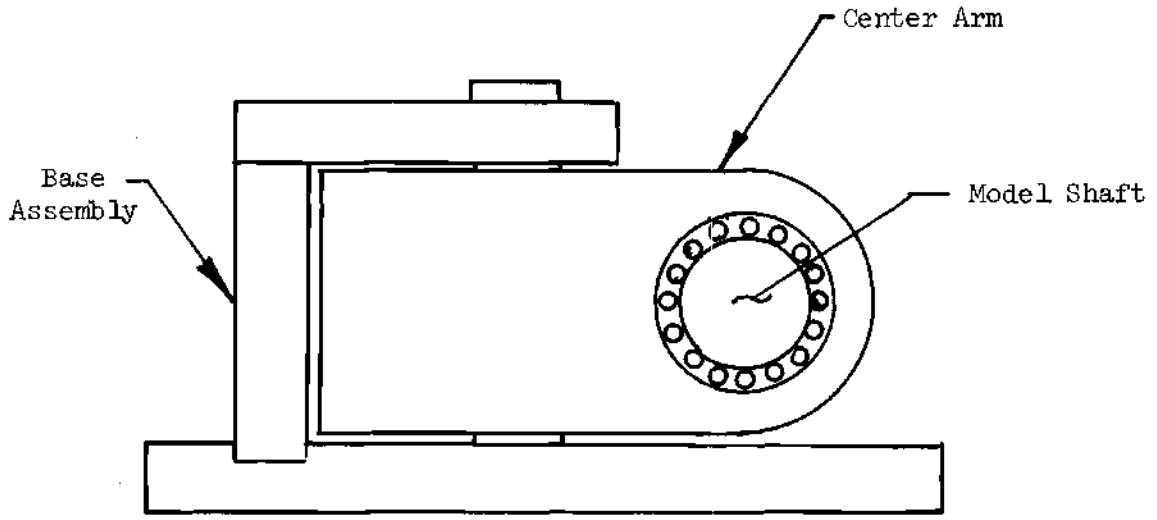

Side View

Figure 3-7. Outer Bearing Assembly

of the motor shaft was transformed into oscillatory motion of the airfoil through the use of a motor shaft crank with an eccentrically mounted drive rod. Four different crank cylinders with differing amounts of eccentric offset were used during the tests. The four different offsets, combined with the length of the drive arm, produced amplitudes of oscillation at the airfoil of ± 2, ± 4, ± 6, and ± 8 degrees.

A Minarik Torque Generator, Model WTF-73, was used to regulate the motor speed. The actual operating frequency was obtained in a manner similar to that used to determine the gust generator vane frequency. A sixty-tooth gear was attached to the back of the motor shaft crank. A magnetic detection unit was located on the drive mechanism base-plate, close to the gear. The signal from the detection unit was then filtered with a Krohn-Hite model #3343, low pass filter, and then applied to an electronic counter. The airfoil oscillation frequencies that were used during the tests ranged from two to twenty Hertz.

The drive rod and drive arm assembly were connected between the motor crank and the linkage shaft. The drive arm was keyed to the linkage shaft and located on the outward section of the linkage between the main and outer bearing assemblies (see Figure 3-5A). A second B & K accelerometer was attached to the bottom of this drive arm (see Figure 3-8).

The oscillatory driving force from the motor was applied to the linkage shaft through a load cell which was connected on one side to the

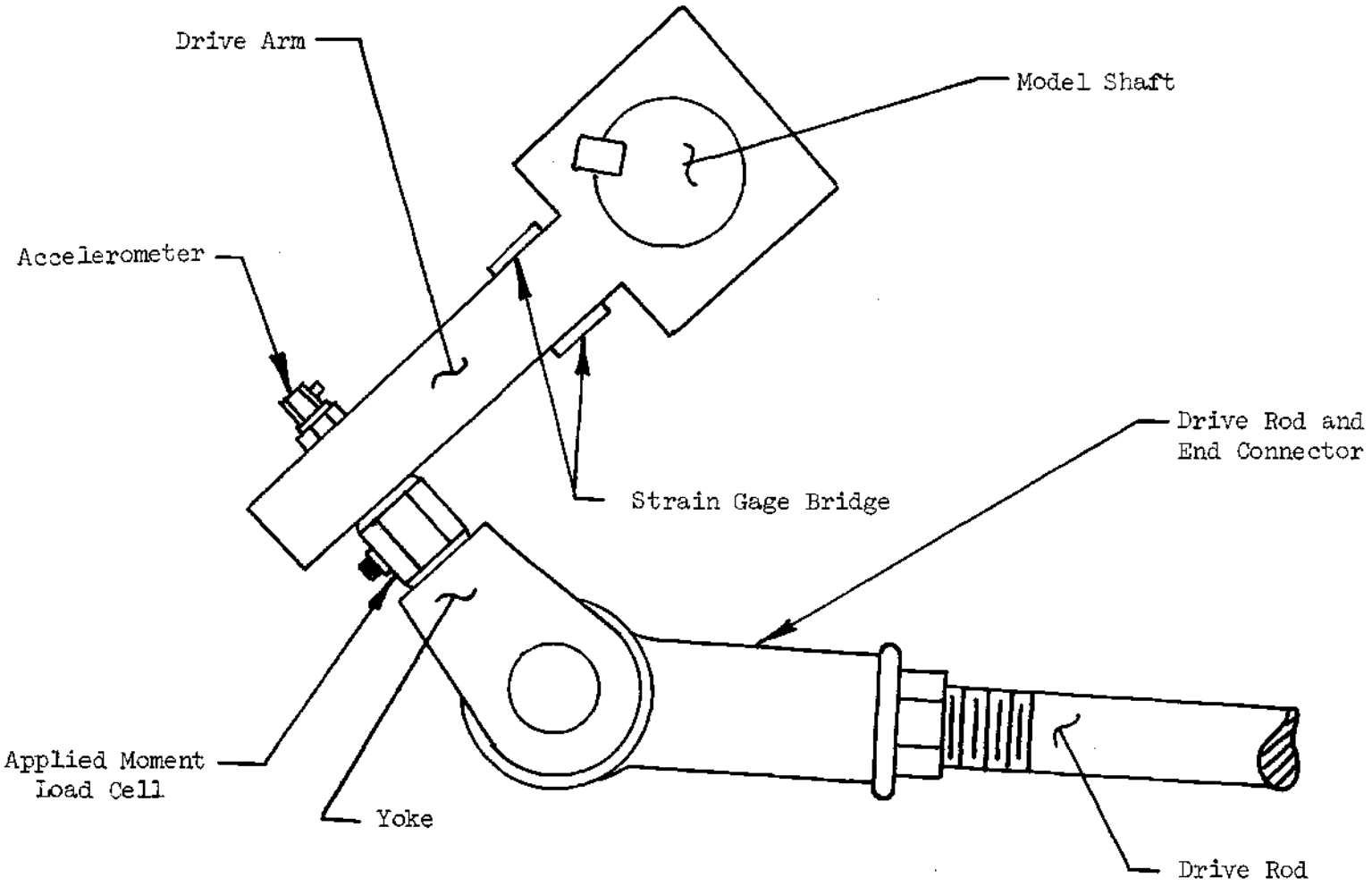

Figure 3-8. Drive Arm and Drive Rod Assembly

bottom of the drive arm and on the other side to a drive rod yoke. One end of the drive rod was pinned to this yoke, while the other end was connected to a crank pin attached to the motor shaft crank. The line of action of the load cell was always at right angles to the drive arm, and at a fixed distance from the center-line of the linkage shaft. Thus, the load cell signal, together with the moment arm distance, determined the total applied moment to the airfoil.

The applied moment was also obtained from a third strain gage bridge, which was bonded to the drive arm at the position of maximum bending moment (see Figure 3-8). This bridge contained four active arms, connected in a manner similar to the lift bridges attached to the main bearing assemblies. The drive arm dimensions were designed to provide adequate strain gage sensitivity, while at the same time keeping the natural frequency of the system well above the airfoil oscillation frequencies.

Calibration of Load Cells

Three Kistler, #912, quartz load cells were installed in the model support and drive system. The devices were each connected to M-B voltage line drivers, and then to three M-B Model N400 amplifiers. Because these piezoelectric load cells are charge devices, the use of voltage line drivers eliminated any D.C. level from the load cell signals. Thus it became necessary to calibrate each load cell in a dynamic manner.

The calibration method made use of the model support and drive system. A dummy shaft was placed inside the wind tunnel, through both

of the main bearings. The rigid linkage was also installed, together with the drive arm, in the model oscillation system. The load cell to be calibrated was then installed in the drive system, between the drive arm and the drive yoke (see Figure 3-8).

The load cell was calibrated by oscillating the drive mechanism at a known frequency and amplitude. The load cell output signal then became a measure of the force required to overcome the rotational inertia of the dummy shaft. Hence the maximum, or peak voltage represented the maximum value of inertial torque on the system. The actual force acting on the load cell was calculated by dividing the maximum value of inertial torque by the distance between the load cell line of action and the shaft axis of rotation. The equation that was used is given below.

$$F_{max} = \frac{I|\ddot{\theta}_{max}|}{r} \qquad (3\text{-}1)$$

or

$$F_{max} = \frac{I|\omega^2 \Delta\theta|}{r} \qquad (3\text{-}2)$$

where

$$\theta = \Delta\theta \cos \omega t \qquad (3\text{-}3)$$

The three quantities that could be varied during the calibration were moment of inertia, amplitude of oscillation, and the frequency of oscillation. The moment of inertia was changed by attaching steel disks to the dummy shaft. The amplitude of oscillation could be varied

by using motor cranks with different crank pin eccentrics. The frequencies of oscillation used for the calibration were kept within the range of frequencies to be used during the subsequent tests.

The maximum value of the load cell output voltage during each cycle of oscillation was obtained using two different techniques. The first method made use of a Textronics memory oscilloscope, with the peak values of voltage being read directly off the scope for each test condition. The second, and more accurate method, made use of an operational analog computer which was used during the experimental work described in Chapter IV. This computer is an Electronic Associates, Inc. TR-48 analog computer with a DES-30 parallel logic unit.

The analog computer mechanization that was used during the load cell calibrations is shown in Figure 3-9. The circuit consists of two parts. The DES-30 was used to determine the slope of the load cell signal at very short time intervals. When the slope became zero, a logic signal to one of the two track and store units caused the peak voltage to be stored. One track and store unit was used for the positive portion of the signal, while the second unit was used to obtain the negative portions. These two peak values were then added algebraically and averaged to obtain the final maximum voltage.

The calibration data for the three load cells were plotted in graphs of calculated force versus load cell output voltage (see Figures 3-10 through 3-12). A least squares linear fit equation was obtained from this force versus voltage data. These straight lines were then used as the calibration curves for each respective load cell.

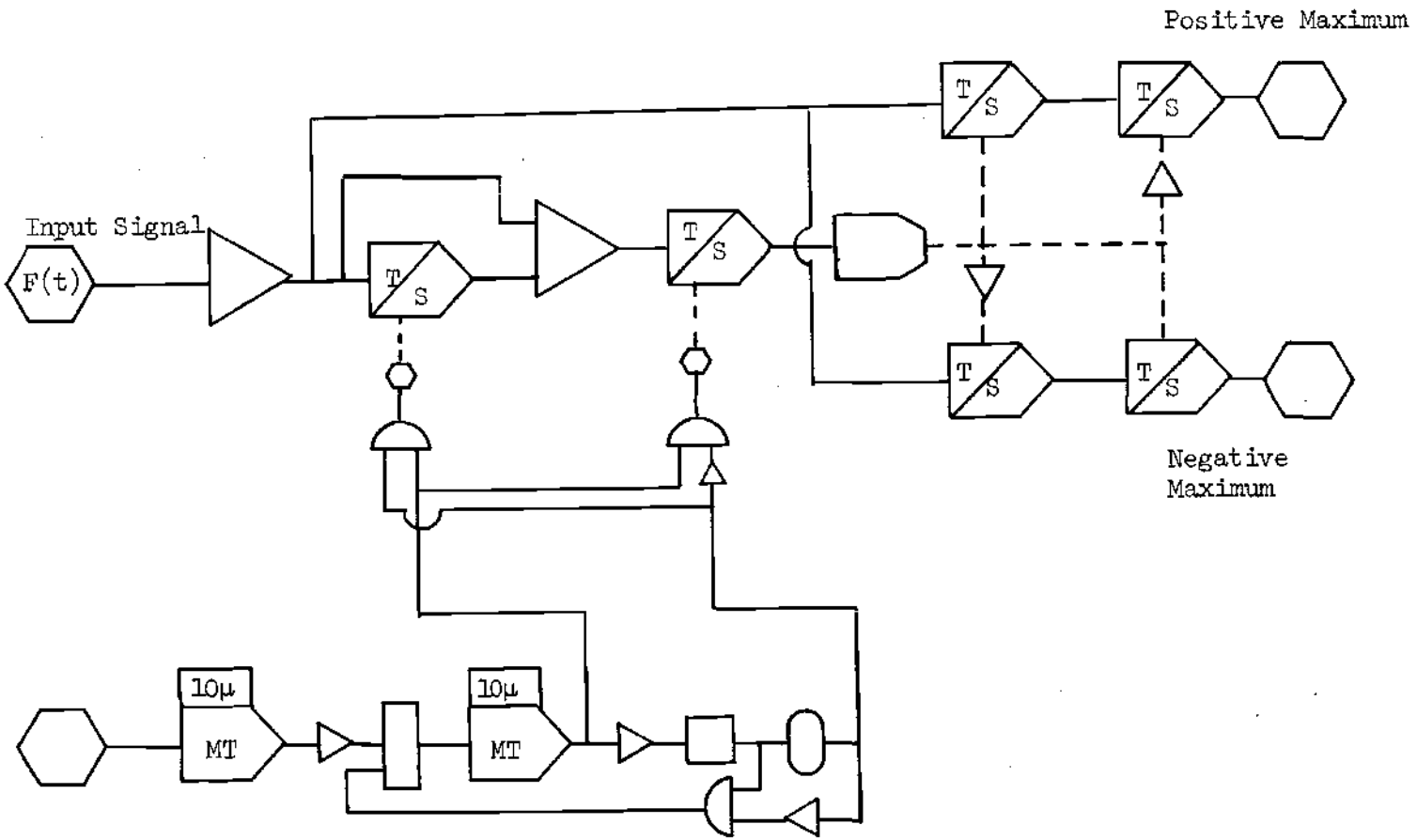

Figure 3-9. Mechanization Used to Determine Relative Maximum and Minimum Values of Input Signal

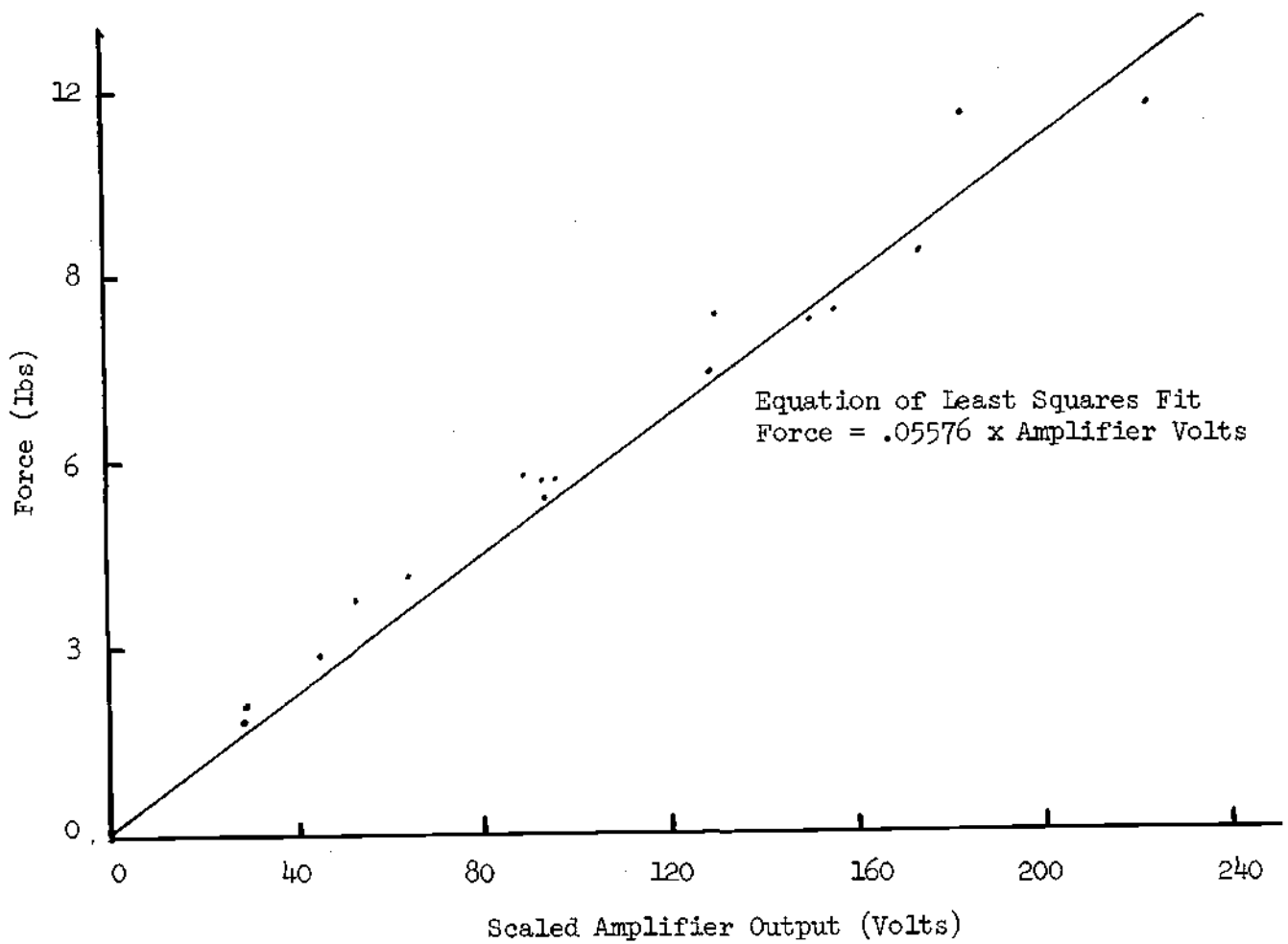

Figure 3-10. Moment Arm Load Cell Calibration Data

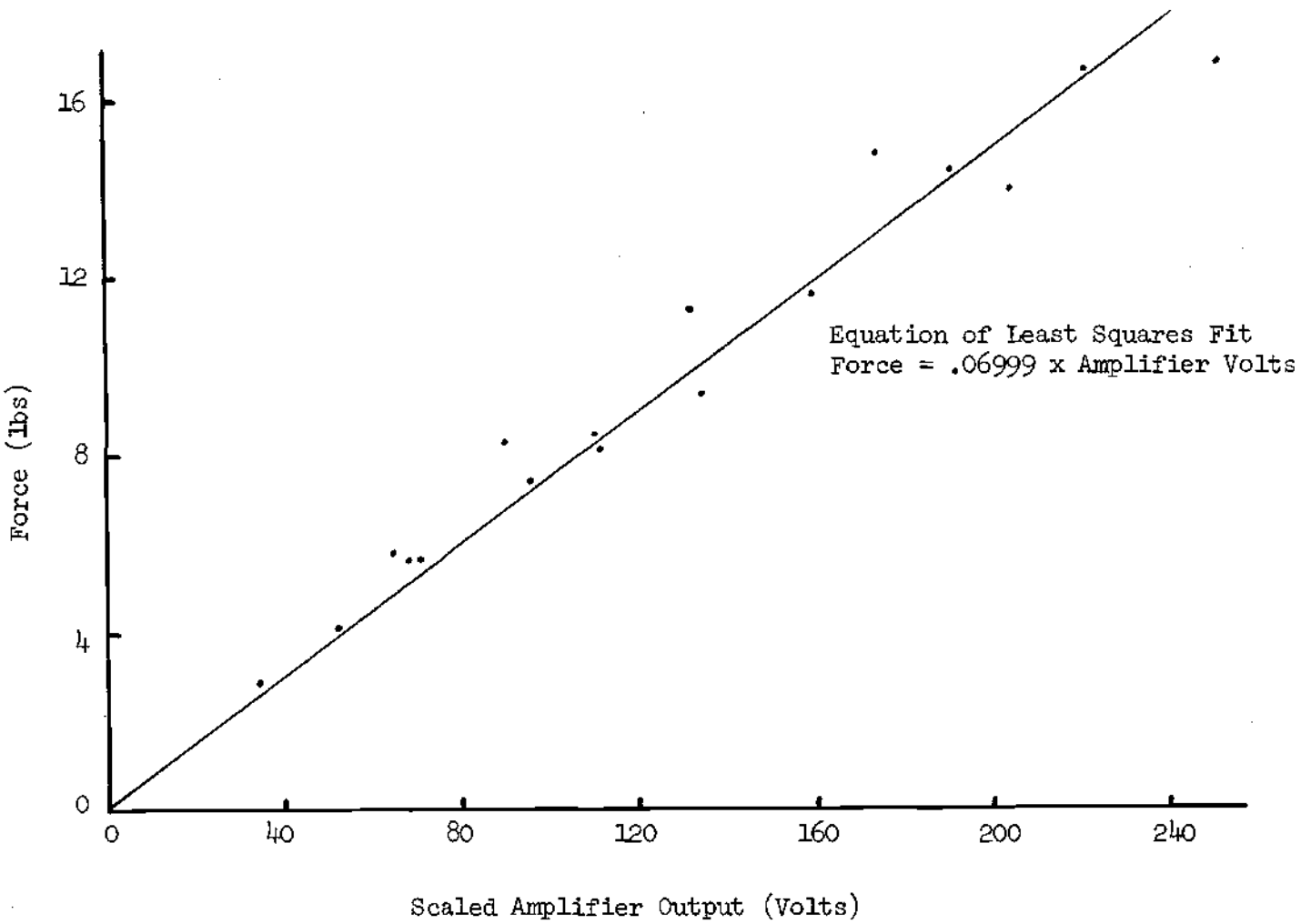

Figure 3-11. Idle-Side Lift Load Cell Calibration Data

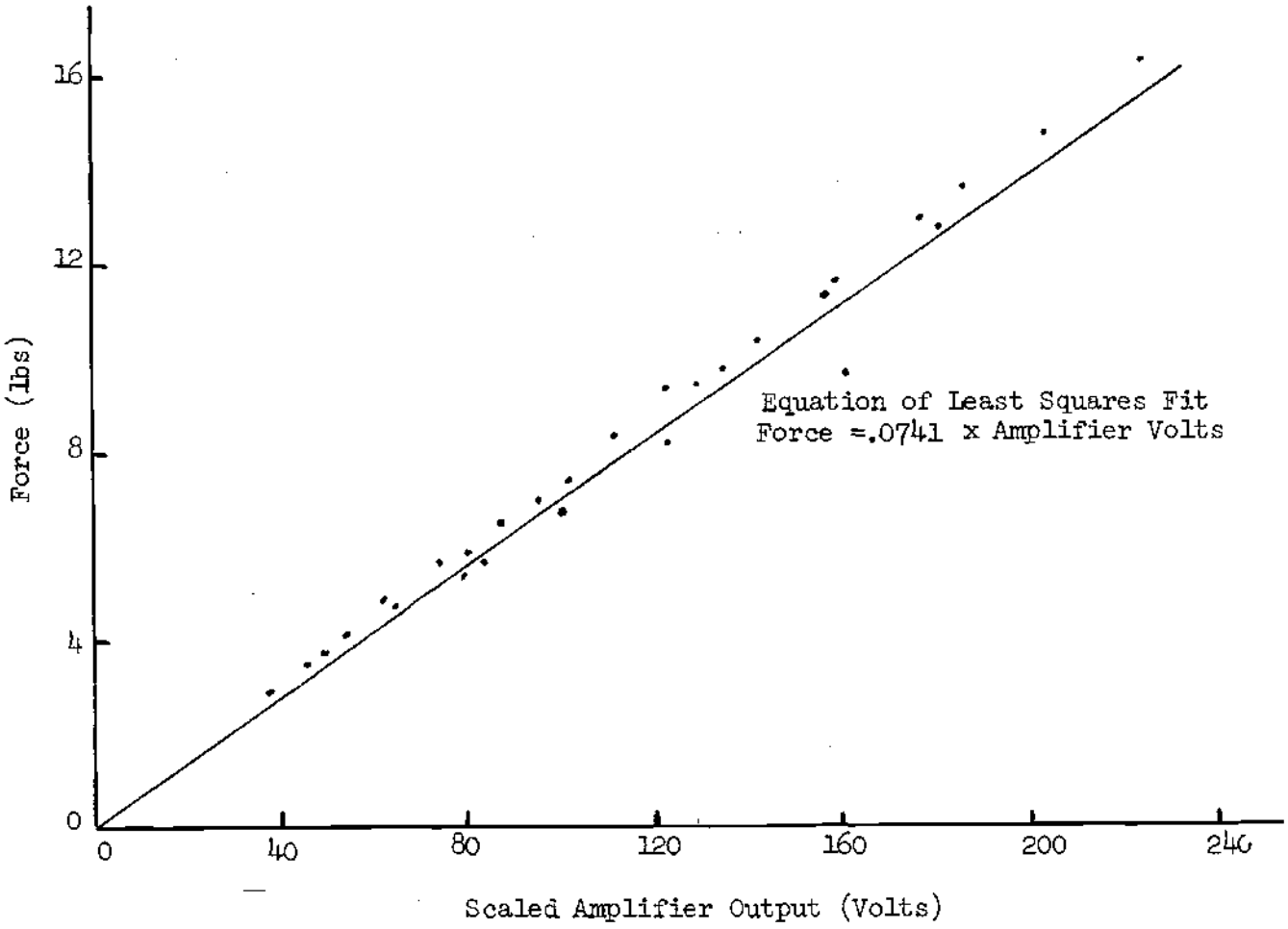

Figure 3-12. Drive Side Lift Load Cell Calibration Data

Calibration of Strain Gage Bridges

For the strain gage calibrations, the rigid linkage was installed in the model drive system. The drive rod was connected between the drive rod yoke and the motor shaft crank. A calibration rig was designed which could be installed on the model by bolting the two halves of the rig together around the airfoil surface. The rig allowed for the placement of a weight pan at various chordwise stations. By varying the pan location and the amounts of dead weight used, it was possible to apply a wide range of downward loads and pitching moments to the airfoil.

During the calibration, the voltage signal from each strain gage bridge was recorded from a digital voltmeter. The combined signal from the two lift bridges represented the total lift force. The signal from the drive arm bridge represented the total applied moment to the airfoil. The calibration curves for lift force (positive down) and applied moment (positive nose down) are shown in Figures 3-13 and 3-14.

Calibration of Accelerometers

The two accelerometers were calibrated by oscillating the airfoil model at known amplitudes and frequencies with the rigid linkage installed in the drive system. Different amplitudes were obtained by changing the motor shaft crank. Each accelerometer was connected first to an M-B voltage line driver unit, and then to an M-B Model N400 amplifier. As in the load cell calibration, the analog computer was used to obtain the maximum value of the accelerometer signal during each cycle of oscillation.

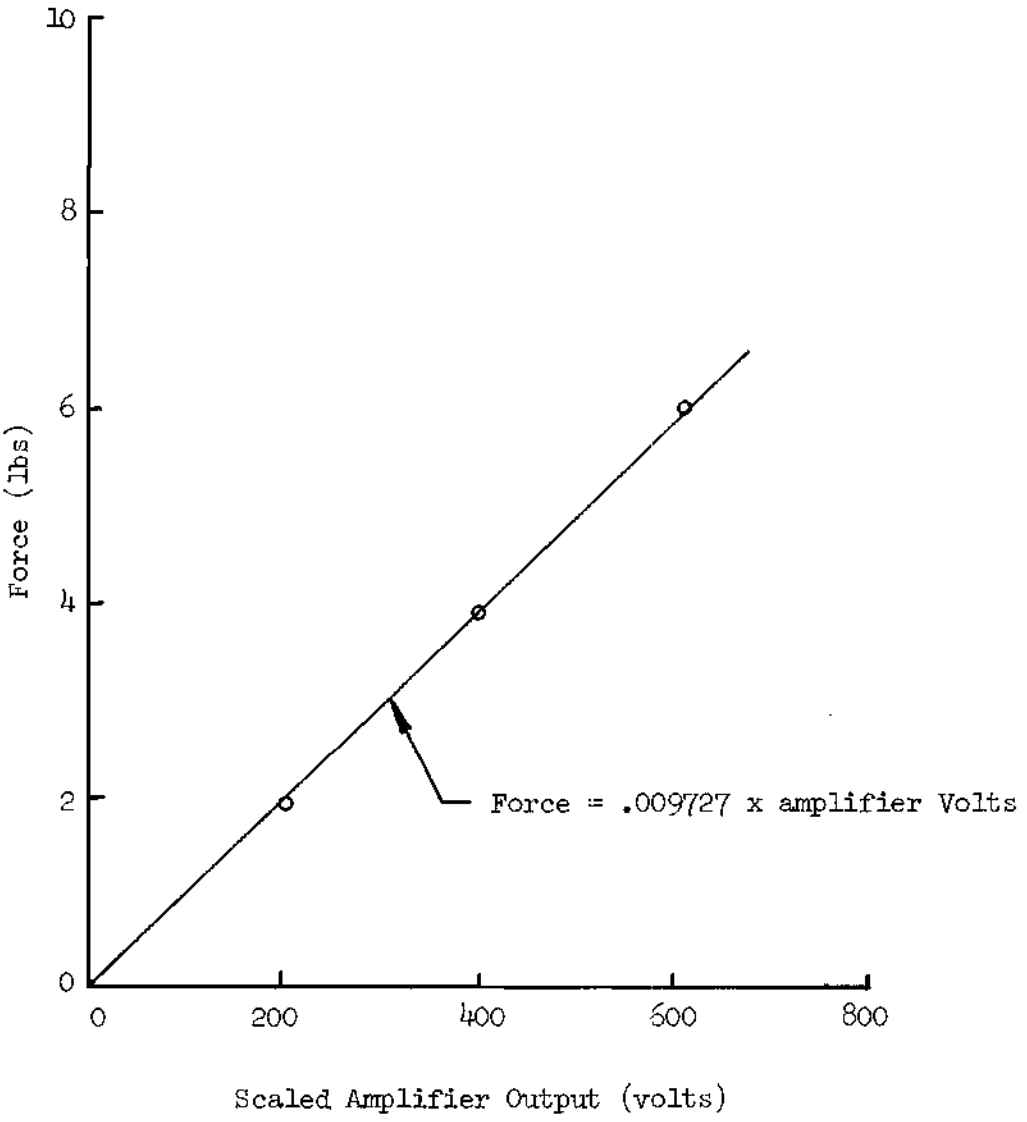

Figure 3-13. Calibration Curve for Lift Strain Gage Bridges

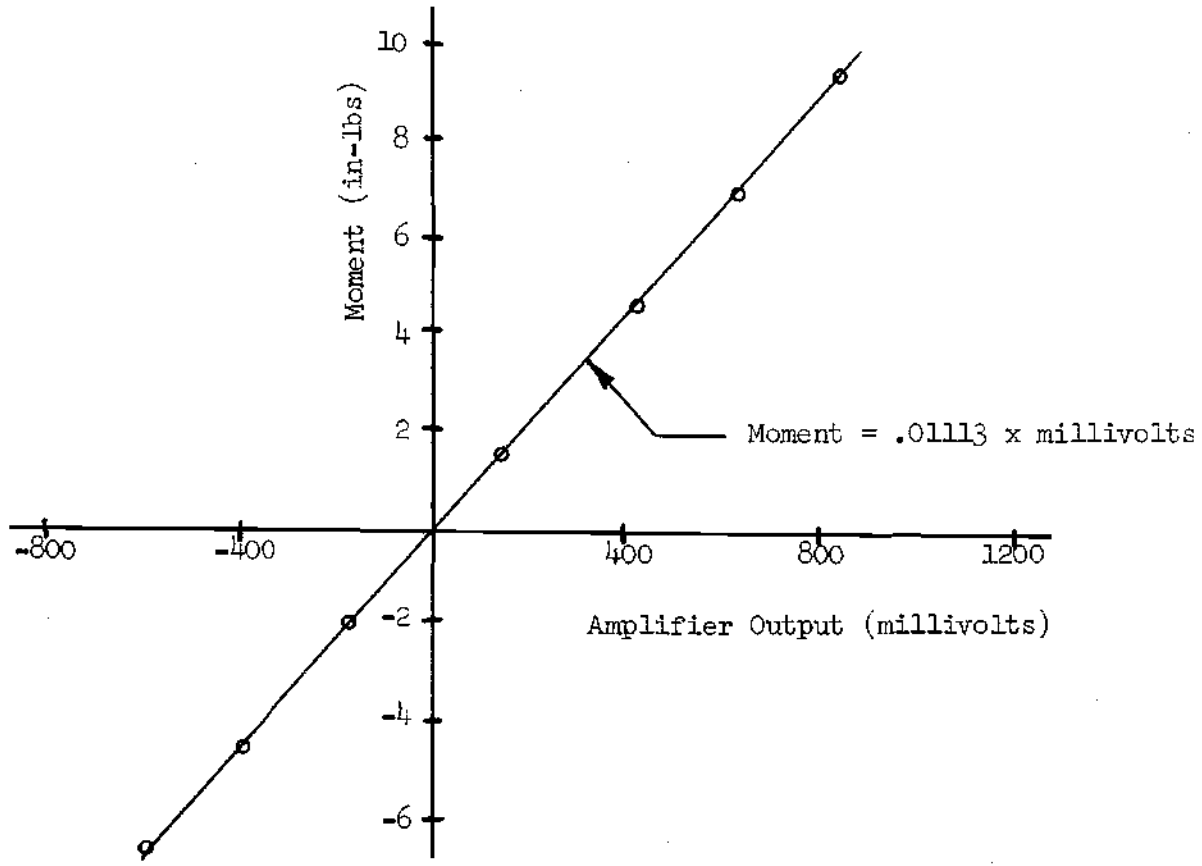

Figure 3-14. Calibration Curve for Moment Strain Gage Bridge

The maximum acceleration for each test condition was obtained from the following equations

$$\theta = \theta_o + \Delta\theta \sin \omega t \tag{3-4}$$

$$|\theta|_{max} = \omega^2 \Delta\theta \tag{3-5}$$

The calibration curves for each accelerometer were obtained by plotting each maximum voltage versus the corresponding maximum acceleration and then using the least squares method to determine the beat linear fit for this data. The curves for both the model and the drive arm accelerometer are shown in Figures 3-15 and 3-16.

Physical Properties of Model and Linkages

Three elastic linkages were constructed for use in the model drive assembly. Each was designed to give a specified natural frequency of oscillation to the airfoil and linkage combination. Initially, the mass moment of inertia of the airfoil model was estimated analytically, and then used as described in Appendix B to calculate the web dimensions for a 10 Hz elastic linkage. The original estimate for I_m did not include the additional mass inertia of the airfoil mass-balancing bars.

The actual torsional spring constant, K, for this linkage was next determined experimentally by the force-deflection method. The weight-pan rig described previously was used to apply a known torque to the airfoil spring combination. Airfoil deflections at the trailing

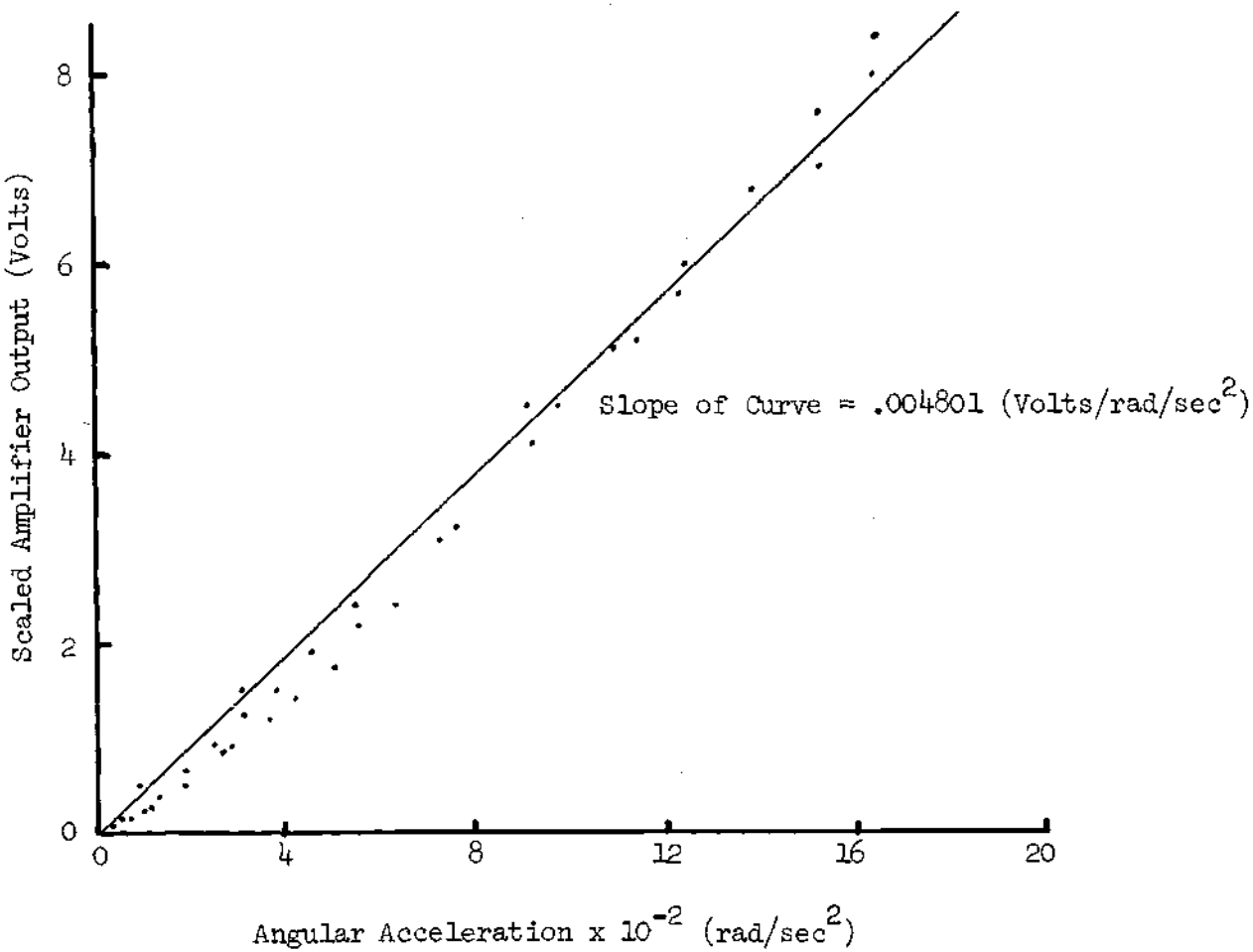

Figure 3-15. Calibration Curve for the Model Accelerometer

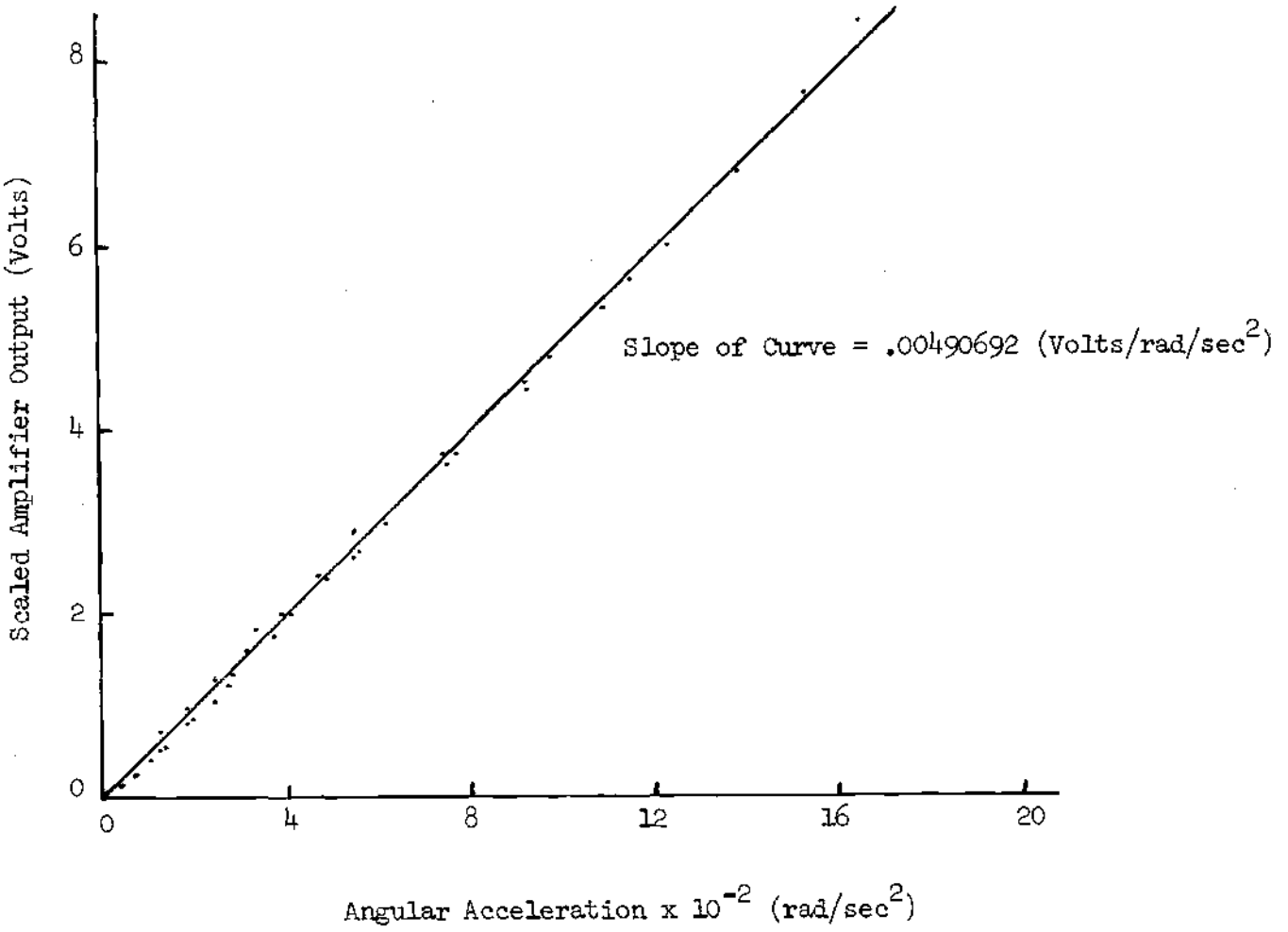

Figure 3-16. Calibration Curve for the Drive Arm Accelerometer

edge were measured with a dial gage. The trailing edge deflections were converted into angular rotations using the following relation.

$$\sin \alpha \doteq \alpha = \text{T.E. deflection}/\ell_T \tag{3-6}$$

where ℓ_T = distance between axis of rotation and the trailing edge.

The values of applied torque versus angular rotation were plotted, and a straight line drawn through the data points. The slope of this line was used as the torsional spring constant for the elastic linkage. The load deflection curve for this linkage is shown in Figure 3-17.

The mass moment of inertia of the airfoil model was determined experimentally using the logarithmic-decrement technique. The output signal from the drive-arm load cell was monitored on an oscilloscope and then photographed as the model was released from a deflected position. From this photograph, the following information was obtained.

$$f_d = 8.7 \text{ Hz} \tag{3-7}$$

$$\delta = \ell n(1.25) \tag{3-8}$$

$$\zeta = \sqrt{\frac{1}{4\pi^2 + \delta^2}} \tag{3-9}$$

$$\omega_n = \frac{2\pi \times \omega_d}{\sqrt{1 - \zeta^2}} \tag{3-10}$$

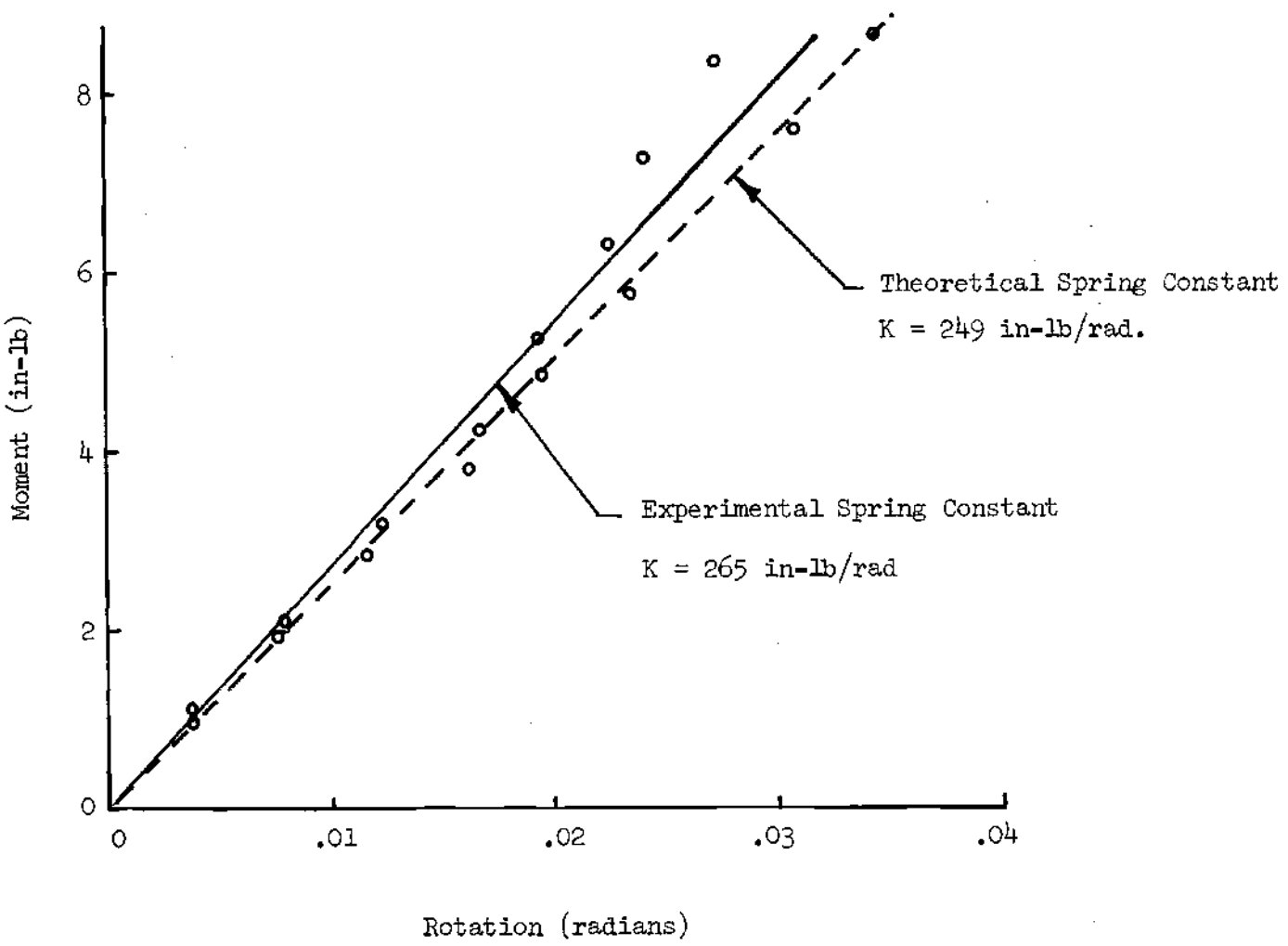

Figure 3-17. Load Deflection Curve for First Elastic Linkage

$$I_m = K/\omega_n^2 = 0.0813 \text{ lb-sec}^2\text{-in} \qquad (3\text{-}11)$$

Using the value of I_m given in Equation (3-11), the web-dimensions for the two remaining elastic linkages were designed to produce natural frequencies of thirteen and twenty Hertz. Then, the logarithmic-decrement method was used to determine the actual value of natural frequency. The relationship given in Equation (3-11) was rearranged and used to determine the actual values of the torsional spring constants. Table 3-1 lists both the actual and the predicted values of K for the three elastic linkages.

Static Lift and Moment Curves

The static lift and moment curves for the airfoil model were obtained using the strain gage bridges. The transducer output signals were converted to airfoil lift and moment using the strain gage bridge calibration curves (Figures 3-13, 3-14). This data was then non-dimensionalized in the usual manner.

$$C_L = \frac{\text{Lift}}{\frac{1}{2}\rho V_o^2 \text{ b. x c}} \qquad (3\text{-}12)$$

$$C_m = \frac{\text{Moment}}{\frac{1}{2}\rho V_o^2 \text{ bc}^2} \qquad (3\text{-}13)$$

Table 3-1. Theoretical and Actual Values for Spring Constant for Three Elastic Linkages

	Spring #1	Spring #2	Spring #3
Theoretical K (in-lb/rad)	246	508	914
Actual K (in-lb/rad)	265	580	1098

These curves were developed for a Reynolds number of 150,000, and are shown in Figures 3-18 and 3-19. The value of the static stall angle was then obtained from the lift curve as approximately twelve degrees.

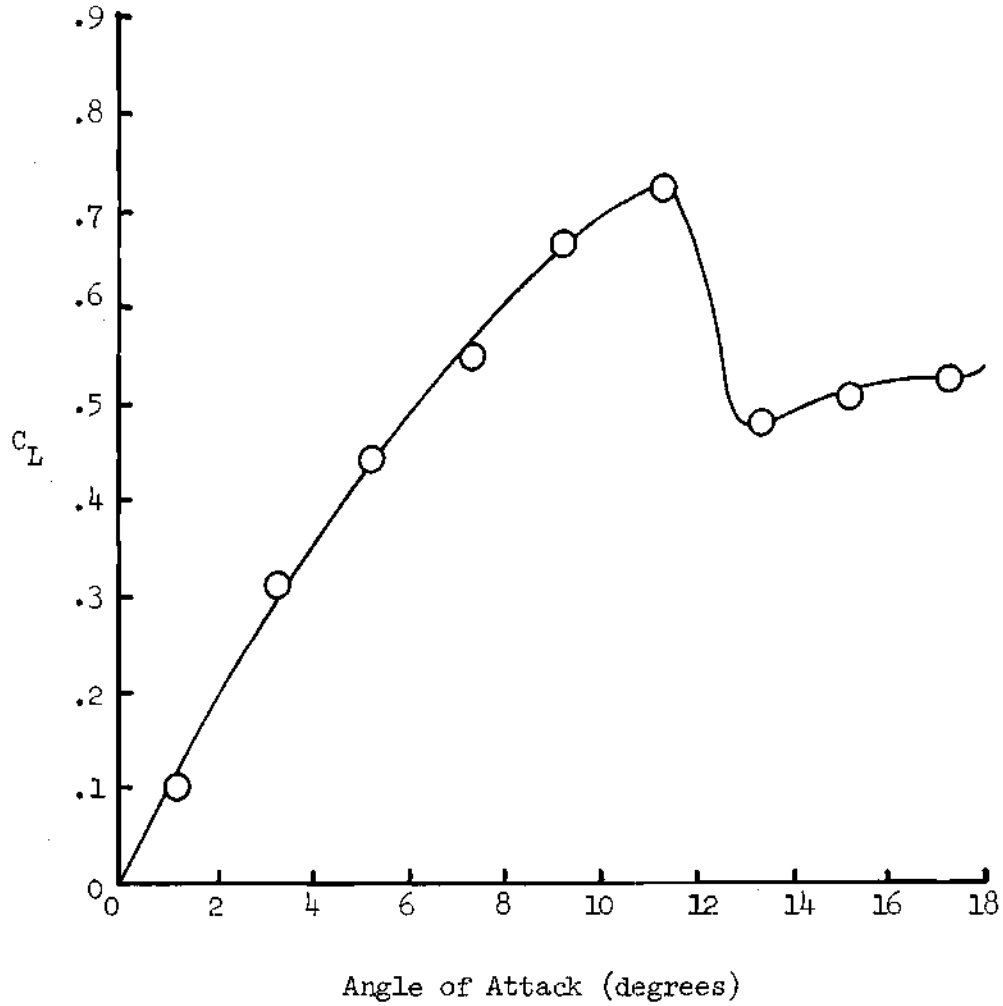

Figure 3-18. Static Lift Curve

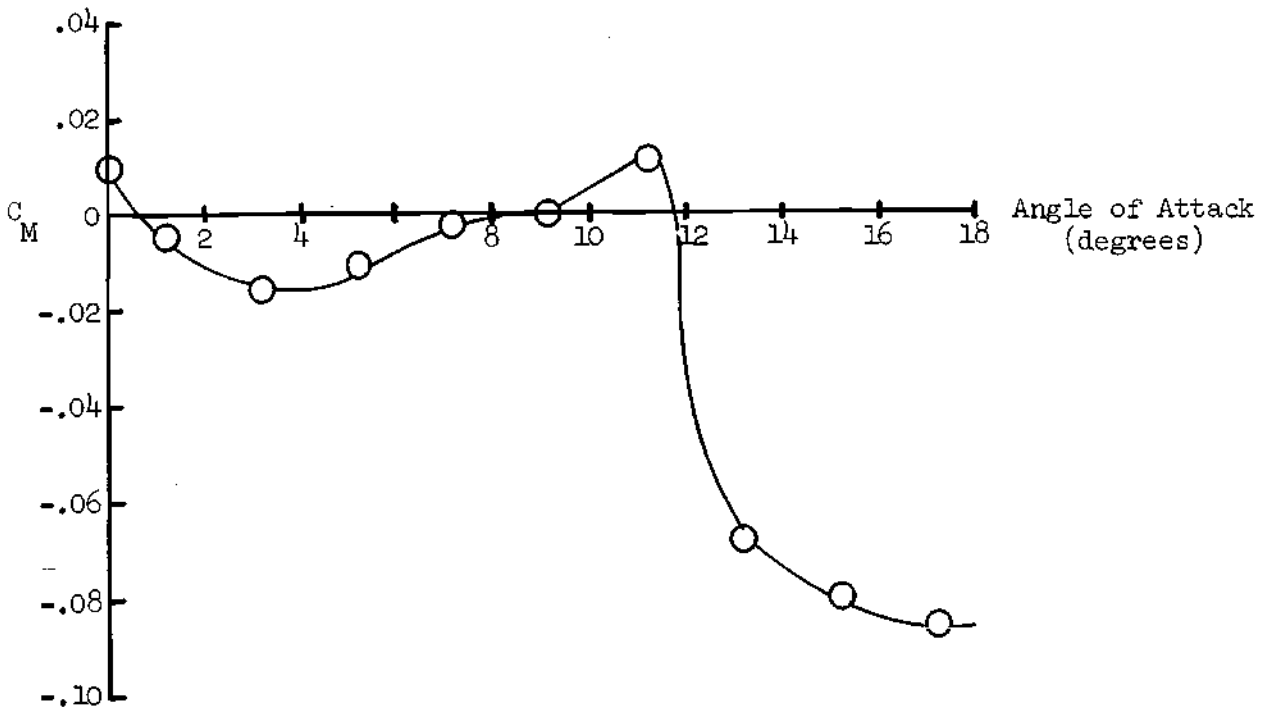

Figure 3-19. Static Moment Curve

CHAPTER IV

DATA ACQUISITION

During the present experimental investigation, an analog computer was used to determine the lift, moment, and aerodynamic work done on an oscillating airfoil. An extensive literature survey has revealed no references to the previous use of an analog computer in a similar manner. Therefore, the following paragraphs discuss in some detail the analog mechanizations that were used to obtain the aerodynamic characteristics of the model airfoil.

Rigid Drive Pitching Moment

The total forcing moment applied to the airfoil by the motor drive system was obtained from the moment load cell and from the strain gage bridge located on the drive arm (see Figure 3-8). During oscillations of the airfoil with the rigid linkage installed in the drive system, the applied moment signal consisted of contributions from several sources. The signal contained not only the wind on, aerodynamic moment, but also the inertial moment and the wind off aerodynamic moment due to the apparent mass of the air.

In order to obtain the desired aerodynamic loading, it was necessary first to determine the instantaneous inertial moment acting on the model and drive system, and then to subtract this contribution from the total moment. Both steps of the procedure were performed on an

operational analog computer by using the airfoil equations of motion to solve for the inertial moment. The output signal from the analog computer was an aerodynamic moment which contained both the wind on and wind off aerodynamic loadings on the airfoil.

Analog Computer Mechanization

The operational analog computer and a parallel logic unit described in Chapter III were used to extract the airfoil aerodynamic moment from the total applied moment. The airfoil equation of motion for pitching oscillations was used to determine the instantaneous value of inertial moment acting on the system. The form of the equation that was used is given below.

$$I_t\ddot{\theta} = M + M_R \qquad (4\text{-}1)$$

This relation neglects any frictional damping arising from the bearing supports. A schematic of the forces acting on the system is shown in Figure 4-1.

Rearranging the equation to solve for the aerodynamic moment gives

$$M = I_t\ddot{\theta} - M_R \qquad (4\text{-}2)$$

Because of the locations of the moment load cell and strain gage bridge, the total pitch inertia, I_t, used in the equation was the sum of pitch inertias for the model and shaft, the adjustment disks, the rigid linkage, and the drive arm. The value of I_t was obtained from the

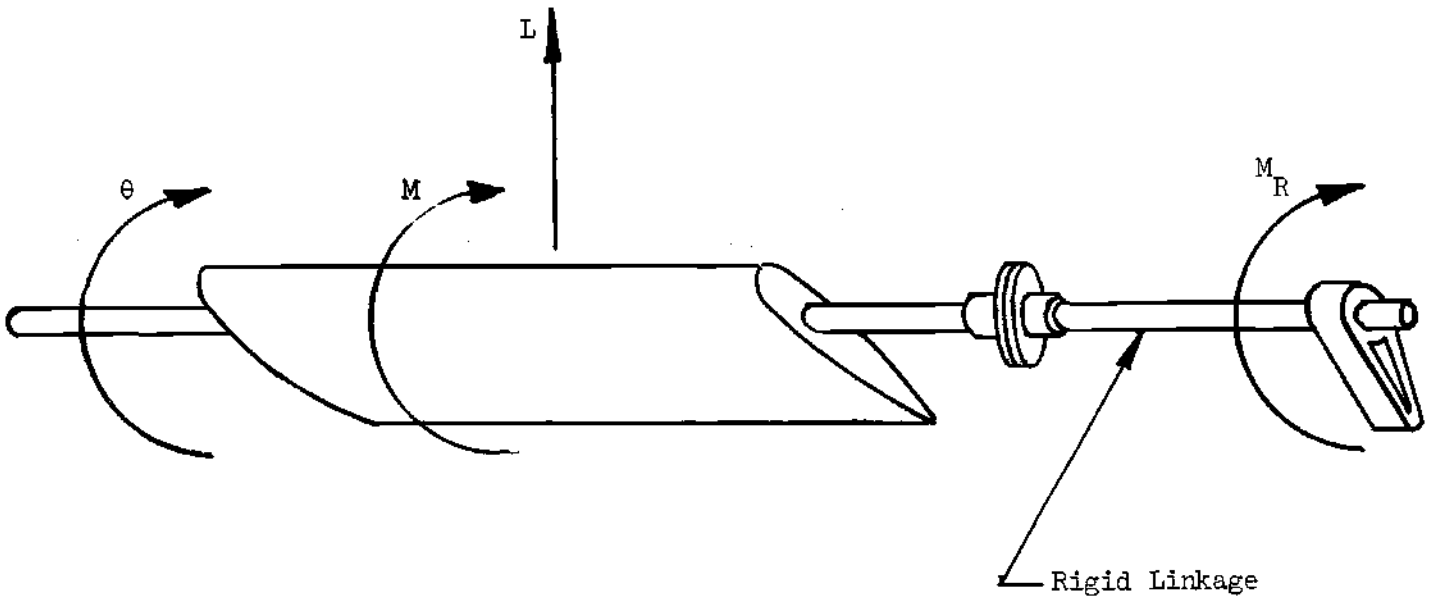

Figure 4-1. Schematic of Forces and Moments Acting on Model and Drive-Arm During Rigid-Forced Airfoil Oscillations

following Equations.

$$I_t = I_m + I_{R.L.} + I_{D.A.} \tag{4-3}$$

$$I_t = .0812732 + .0012149 + .0007677 \tag{4-4}$$

$$I_t = .0832558 \ (lb\text{-}in\text{-}sec^2) \tag{4-5}$$

The mechanization for Equation (4-2) is shown in Figure 4-2. The only input signals to the analog computer required for this mechanization were the airfoil acceleration and the total moment applied to the system.

The total forcing moment, M_R, was first applied to amplifier A01, together with a bias voltage. The level of bias was controlled by potentiometer P01. This bias voltage was used to zero the output of the moment strain gage bridge prior to oscillation of the airfoil. When the applied moment signal was obtained from the drive arm load cell, potentiometer P01 was set to give a zero bias voltage.

The model accelerometer signal was applied to amplifier A05, and then multiplied by the value of I_t to obtain the instantaneous inertial moment acting on the system. Amplifier A03 was then used to subtract this inertial moment from the total applied moment.

The output voltage from amplifier A03, which represented the airfoil aerodynamic moment acting on the airfoil, was scaled using potentiometers P02 and P03. When these potentiometers were set to the calibration constants obtained from Figures 3-9, 3-13, and 3-15, the

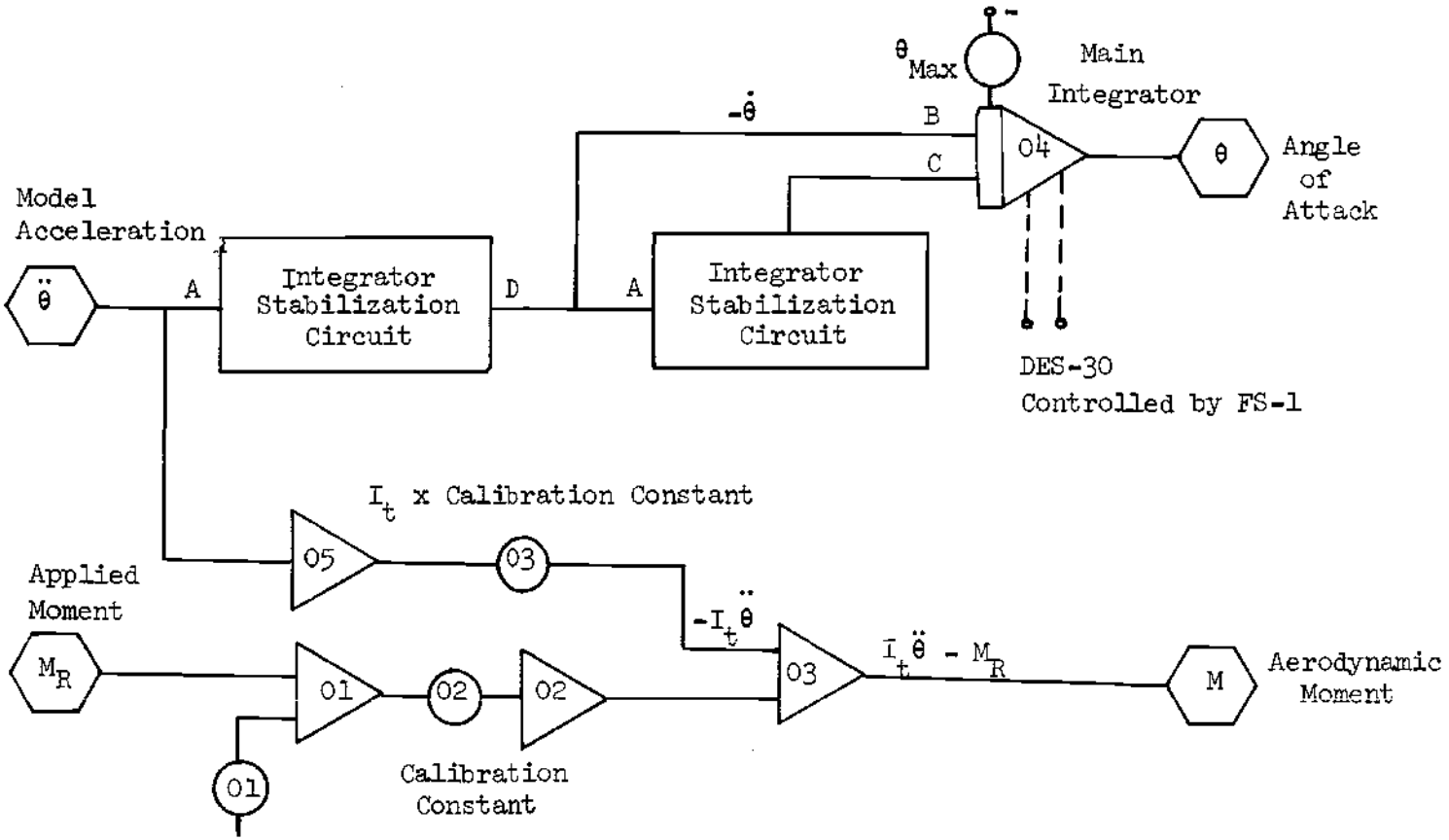

Figure 4-2. Analog Mechanization for Rigid-Forced Airfoil Oscillations

output of A03 could be interpreted directly in terms of aerodynamic moment with units of in-lbs.

The angle-of-attack of the airfoil was obtained from the analog computer by integrating the model acceleration signal twice with respect to time. The integrations were performed by applying the acceleration signal to a series of integrating amplifiers (see Figures 4-2 and 4-3) whose initial conditions represented the model velocity and displacement at the instant t = 0. The initial conditions that were used for this mechanization are given below.

$$\dot{\theta}(o) = 0 \tag{4-3}$$

$$\theta(o) = \theta_o + \Delta\theta = \theta_{max} \tag{4-4}$$

An instability inherent in open end integration on the TR-48 caused the output signal from each integrator to drift with time. Thus, stabilization circuits were needed for the integrating amplifiers to insure that the final signal representing the model angle-of-attack would oscillate about a mean value without drifting.

Two identical stabilization circuits were used to control the output signals of the integrators. Since the main integrator, I04 of Figure 4-2, required a non-zero initial condition, accurate output signals from this amplifier were obtained by holding the integrator in the initial condition mode until the necessary stabilizing voltages could be generated.

The mechanization for a typical stabilization circuit is shown in Figure 4-3. The dummy integrator generated a signal that was applied to both an electronic comparator and a pair of track and store

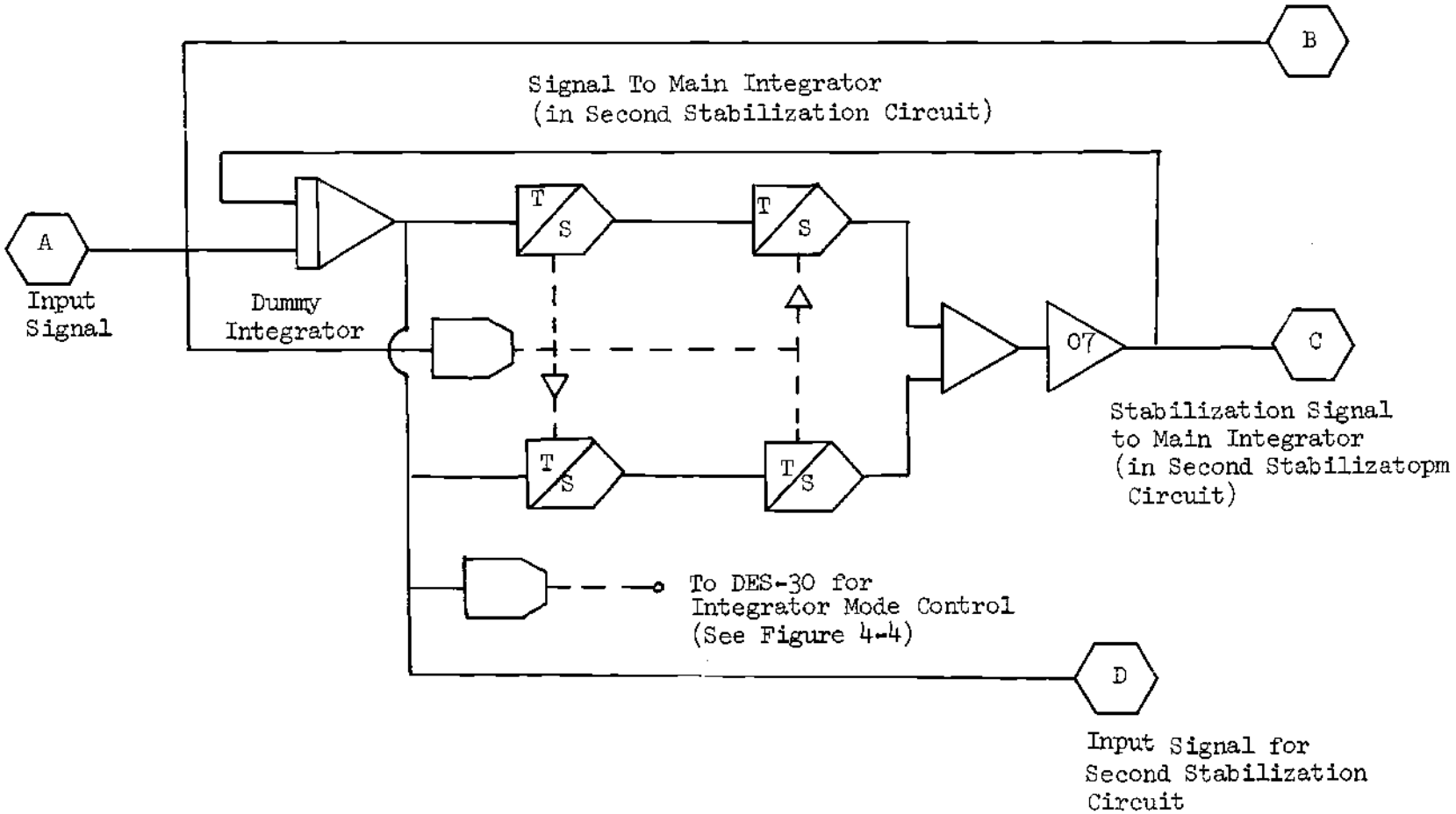

Figure 4-3. Integrator Stabilization Circuit

units. The comparator produced a square wave logic signal that controlled the track and store units. One unit stored the maximum, while the other stored the minimum values of the integrator output signal momentarily during each cycle. These two voltages were added together and then fed back to the dummy integrator.

Two amplifiers, A07 and the corresponding amplifier in the second stabilization circuit, were used to monitor the level of feedback signal to the dummy integrators. When these signals had reached a steady level, the main integrator could be switched into the operate mode. This switching operation was controlled by logic from the DES-30.

The mechanization for the DES-30 is shown in Figure 4-4. The circuit consisted of two general purpose registers, patched as dual flip-flops in series. Two electronic signals were inputed to the DES-30 from the TR-48. The first was a starting signal which could be applied to the DES-30 through a manual function switch. The second was a square wave logic signal generated by one of the comparators used in the integration feedback circuit described previously.

The comparator signal was connected to the enable and load contacts of the two flip-flops, thus insuring that the flip-flops would respond to the starting signal only when the square wave changed from a zero to a unit one level. This condition occurred whenever the model acceleration attained a maximum value.

The output logic of the second flip-flop was connected to the bus lines which controlled the main integrating amplifier, I06, used to obtain the model angle-of-attack. This logic held the main

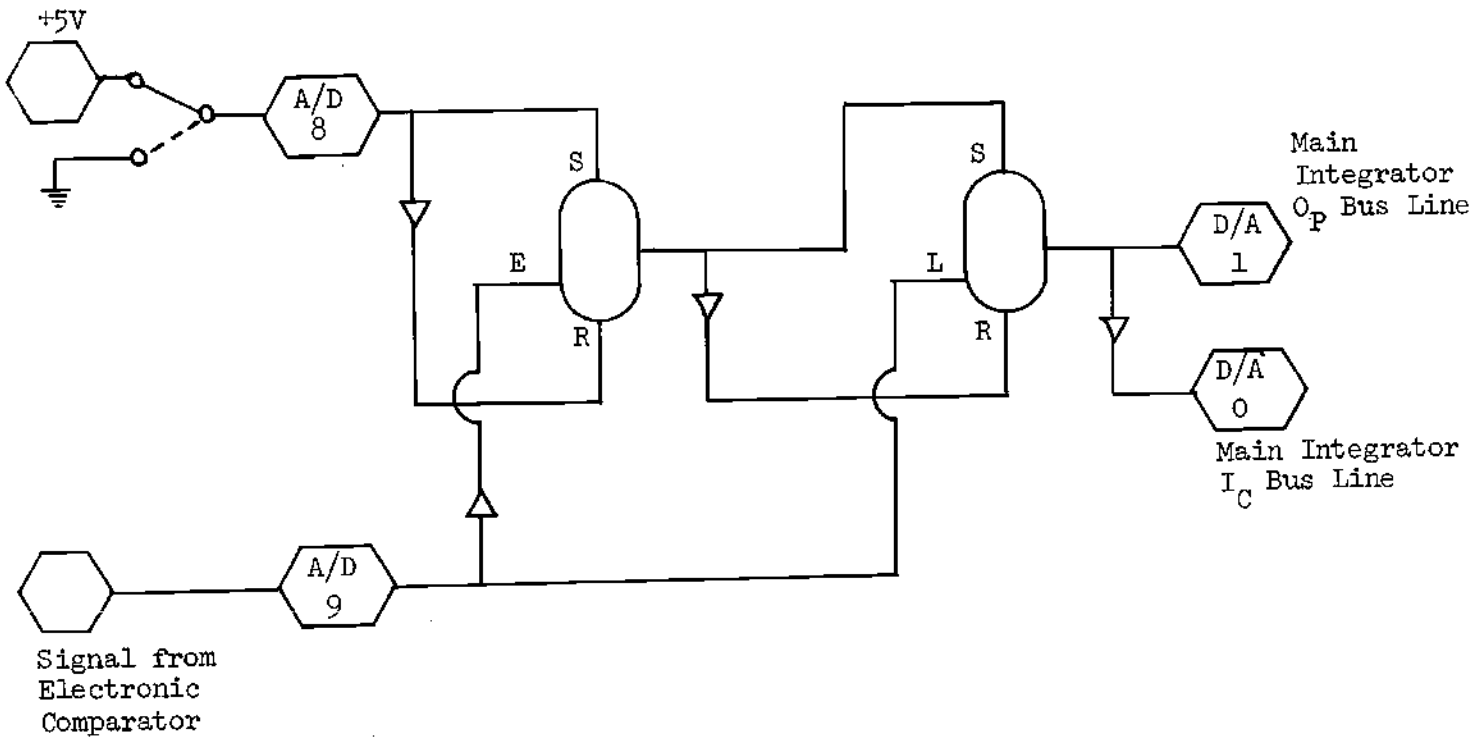

Figure 4-4. Mechanization for DES-30 to Provide Main Integrator Mode Control

integrator in the initial condition mode until the starting signal was applied and the model acceleration reached a maximum. At this point, the second flip-flop changed the logic input to the integrator bus lines. This caused the integrator to switch to the operate mode and to remain in this mode for as long as the manual function switch remained closed.

Elastic Drive Pitching Moment

In the analog mechanization for rigid airfoil oscillations, the aerodynamic moment was obtained as the difference between two signals: the applied moment and the inertial moment. Due to the fact that the maximum inertial moment is proportional to the square of the frequency, this difference signal becomes a small percentage of the total input signal at the higher oscillation frequencies. This situation, together with the error tolerances of the analog computer, increased the amount of possible error present in the determination of the aerodynamic moment at higher frequencies.

To decrease the magnitude of this experimental error, a second type of forced oscillation test was conducted with the airfoil model. For these tests, the rigid linkage was replaced with the elastic linkages described in Chapter III. These linkages acted as a torsional spring for the model. The motor drive system was then used to produce forced oscillations of the airfoil through each of these elastic linkages.

For each elastic linkage, the model was oscillated at a frequency near the natural frequency of the airfoil and spring

combination. This near resonant condition decreased the total amount of motor torque required to sustain the airfoil oscillations. The decrease in inertial moment with respect to the total moment produced a more accurate determination of the aerodynamic moment acting on the airfoil model.

With this test procedure, the number of model oscillation frequencies that could be used was limited by the total number of elastic linkages that were available. In order to increase the number of test frequencies that could be used with each elastic linkage, several steel disks were attached to the idle side of the model shaft in varying combinations. Each disk was eight inches in diameter and approximately 1/4 inch in thickness. The additional amounts of mass inertia that were added to the system by the disks caused a change in the value of the natural frequency of each airfoil-spring combination. Therefore, a new resonant frequency, and consequently a new model oscillation frequency, was created for each inertia disk that was added to the model shaft.

Analog Computer Mechanization

A schematic of the forces acting on the model and drive system during forced elastic oscillations is shown in Figure 4-5. From this schematic, equations of motion can be written for both the airfoil model and the drive arm. The equation for the airfoil model is given below.

$$I_m \ddot{\theta} = M - K(\Delta\theta - \theta_d) \qquad (4\text{-}5)$$

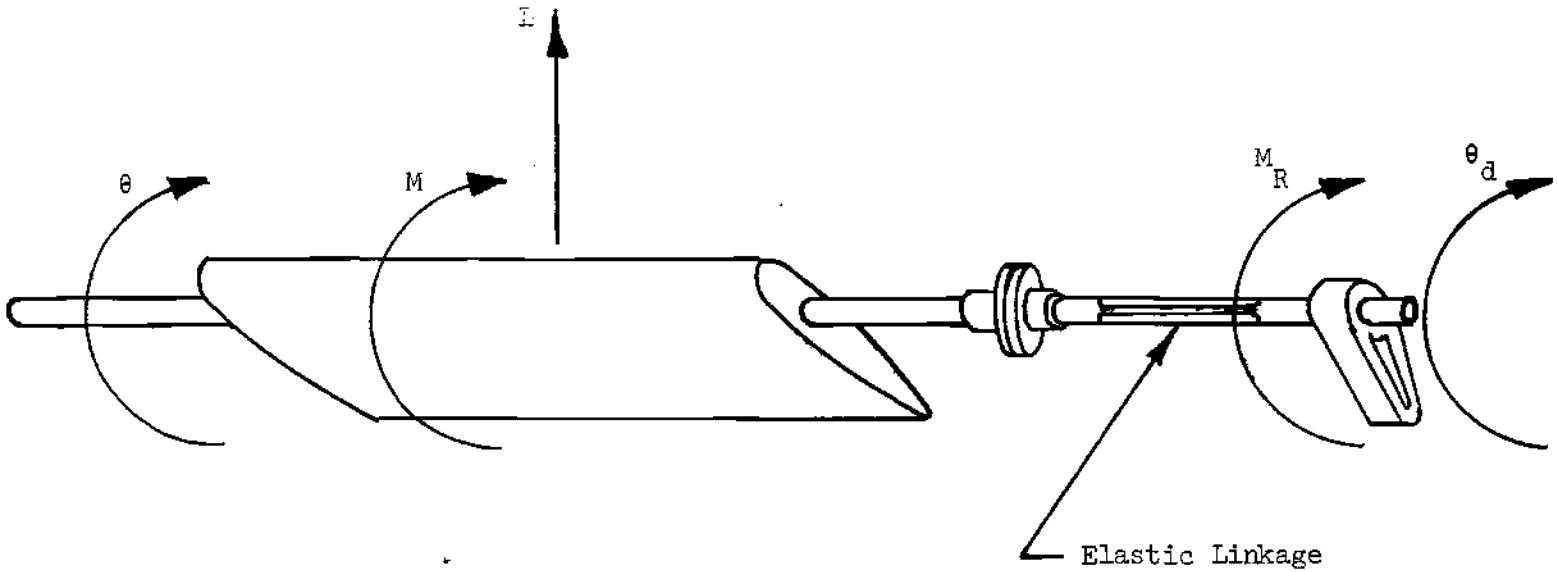

Figure 4-5. Schematic of Forces and Moments Acting on Model and Drive System During Forced Elastic Airfoil Oscillations

For this equation, I_m is the mass moment of inertia of the airfoil, adjustment disks, elastic linkage, and inertia disks. Similarily, the equation for the drive arm is:

$$I_d\ddot{\theta}_d = M_d - K(\theta_d - \Delta\theta) \tag{4-6}$$

where I_d is again the mass moment of inertia for the drive arm. Both of these equations assume that there is no frictional damping and that the inertia of the elastic linkage is equally divided between I_d and I_m. The values of K for each linkage are listed in Table 3-1.

Equation (4-5) can be arranged and solved for the applied moment.

$$M = I_m\ddot{\theta} + K(\Delta\theta - \theta_d) \tag{4-7}$$

The second term on the right side of the equation is replaced using Equation (4-5).

$$M = I_m\ddot{\theta} + I_d\ddot{\theta}_d - M_d \tag{4-8}$$

The mechanization for Equation (4-8) is given in Figure 4-6. The signals required as inputs for the mechanization are the model acceleration, the drive arm acceleration, and the total applied moment. The functions of the bias potentiometer, P01, and the three scaling potentiometers, P02, P03, and P04 are the same as described for the previous mechanization (see Figure 4-2).

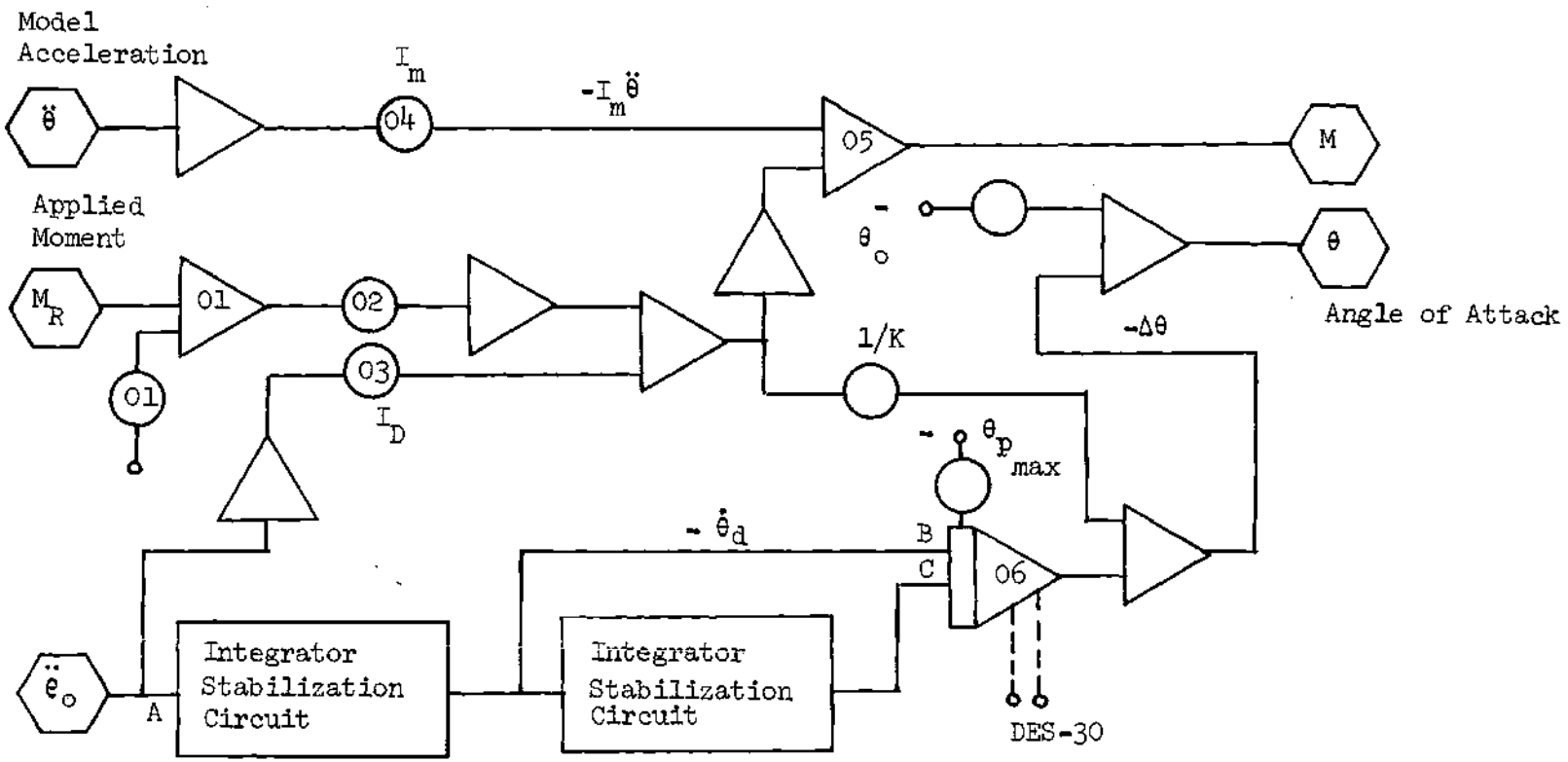

Figure 4-6. Analog Mechanization for Forced Elastic Airfoil Oscillations

The airfoil angle-of-attack, θ , was determined from

$$\theta = \theta_o + \Delta\theta \tag{4-9}$$

where $\Delta\theta$ was obtained by rearranging Equation (4-6) as

$$\Delta\theta = \theta_d + \frac{1}{K}\left(I_d \ddot{\theta}_d - M_d\right) \tag{4-10}$$

The drive arm angle, θ_d , was obtained by performing two integrations of the drive arm acceleration, $\ddot{\theta}_d$. As in the case of rigid oscillations, the integrations were performed using two integrating amplifiers (see Figure 4-6). The initial conditions that were used with these amplifiers were the same as given in Equations (4-3) and (4-4). The DES-30 was again used to start the main integrator and, as in the previous analog mechanization, a feedback circuit was connected to each integrating amplifier to prevent drifting of the output signal.

The change in airfoil angle-of-attack, $\Delta\theta$, was obtained by multiplying the signal $I_d\ddot{\theta}_d - M_d$, which was needed in the determination of the aerodynamic moment, by the reciprocal of the elastic linkage spring constant, K. This signal was then combined with the drive arm angle, θ_d , by using a summing amplifier. The model angle-of-attack was finally obtained by applying the $\Delta\theta$ signal, together with a bias signal representing the mean angle-of-attack, θ_o , to another summing amplifier (see Figure 4-6).

Elastic Free Pitching Moment

A third type of experimental test was conducted with the model in an effort to obtain information concerning the aerodynamic damping generated during free oscillations of the airfoil. With these experiments, the elastic linkages and the inertia disks were installed in the drive system in varying combinations. Each of these combinations provided the system with a different natural frequency during torsional oscillations.

For each test, the drive arm was clamped in position, while the airfoil was secured in an initially deflected position. Then the model was released and permitted to oscillate freely in the airstream. The analog computer was again used to determine the aerodynamic moment and the airfoil angle-of-attack during each test.

Analog Computer Mechanization

A schematic of the force system acting on the model and linkage is shown in Figure 4-7. Using this force diagram, the equation of motion for the airfoil can be written as:

$$I_m \ddot{\theta} = M - K\Delta\theta \qquad (4\text{-}11)$$

Solving for the aerodynamic moment gives:

$$M = I_m \ddot{\theta} + K\Delta\theta \qquad (4\text{-}12)$$

where I_m is the mass moment of inertia for the model, adjustment disks, and the inertia disks described previously. As before, the spring stiffness for the elastic linkages are in Table 3-1.

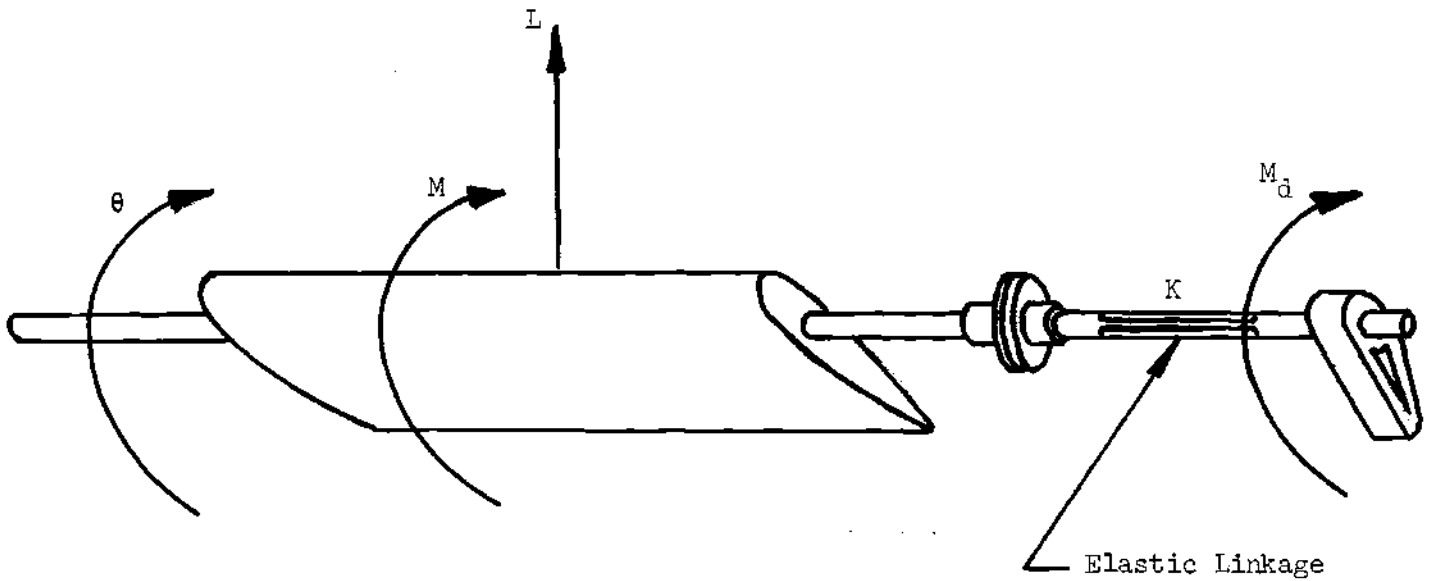

Figure 4-7. Schematic of Forces and Moments Acting on Model and Drive System During Free Elastic Airfoil Oscillations

The equation of the spring moment reaction can also be written using the force schematic.

$$M_d = K\Delta\theta \tag{4-13}$$

The aerodynamic moment is then written in terms of the spring moment reaction using Equations (4-12) and (4-13).

$$M = I_m\ddot{\theta} - M_d \tag{4-14}$$

The airfoil angle-of-attack was obtained from the following equation.

$$\theta = \theta_o + \Delta\theta \tag{4-15}$$

where $\Delta\theta$ is the change in angle-of-attack from the undeflected mean angle-of-attack, θ_o. The use of Equation (4-13) to replace the second term on the right side of Equation (4-15) gives the airfoil angle in terms of the spring moment reactions.

$$\theta = \theta_o - \frac{1}{K} M_d \tag{4-16}$$

The mechanization used for these equations is shown in Figure 4-8. The only input signals required for the analog computer were the model acceleration and the spring moment reaction.

During free, elastic oscillations of the model, only the drive arm load cell was used to produce a voltage signal corresponding to the moment reaction on the elastic linkage. This load cell signal was

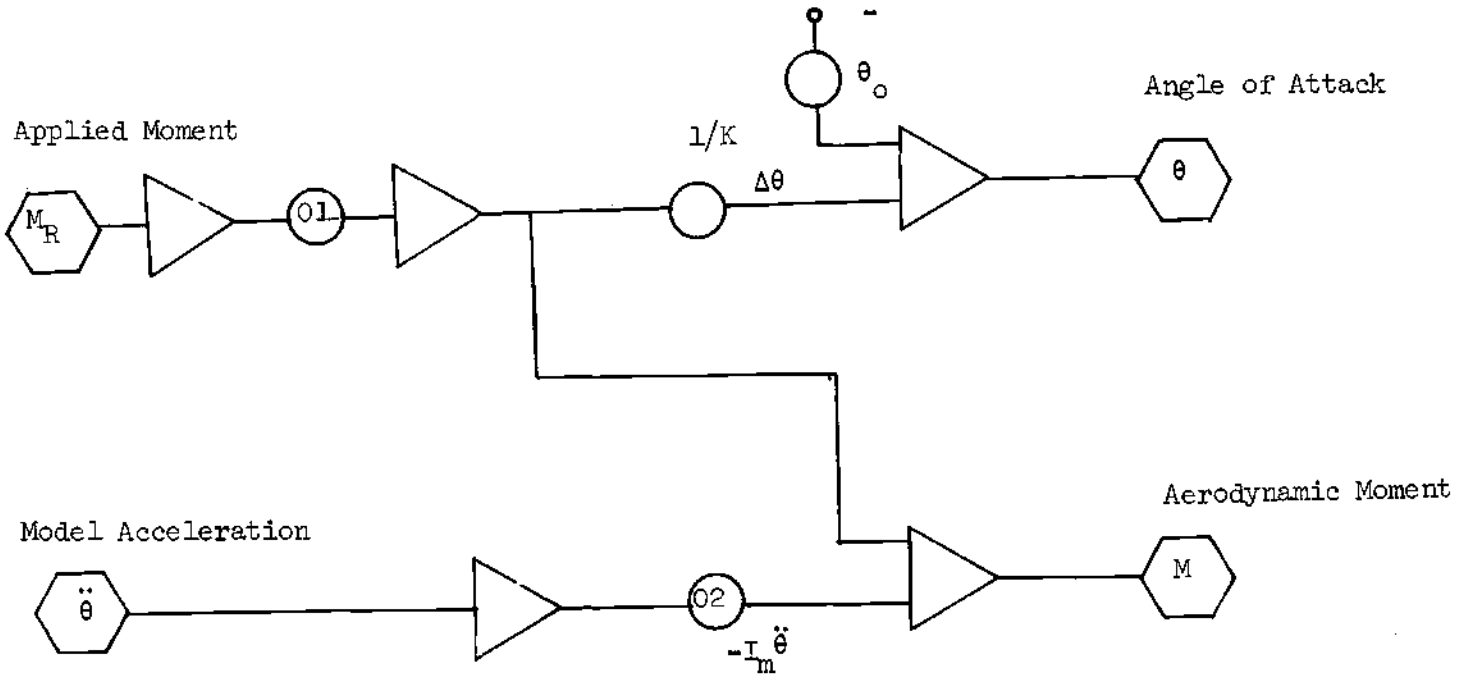

Figure 4-8. Mechanization for Free Elastic Airfoil Oscillations

multiplied by the load cell calibration constant using a grounded potentiometer, P01 (see Figure 3-9). The model angle-of-attack was determined by multiplying the spring moment by the reciprocal of the spring constant, and then using a summing amplifier to combine this signal with a voltage corresponding to the airfoil mean angle-of-attack.

As in the previous mechanization, the model accelerometer signal was applied to a potentiometer, P02, which was set to the calibration constant obtained from Figure 3-9. The inertial moment on the airfoil was obtained by including the value of I_m for the given test in the potentiometer setting. The aerodynamic moment was then obtained by using a summing amplifier to combine the negative of the inertial moment, $-I_m\ddot{\theta}$, with the spring reaction moment, $-K\Delta\theta$.

Aerodynamic Work

The work on the airfoil during forced pitching oscillations was determined using the analog computer. Following the equation,

$$\text{Work} = \int_{\text{cycle}} M d\theta = \int_{\text{cycle}} M\left(\frac{d\theta}{dt}\right) dt = \int_{\text{cycle}} M\dot{\theta}\, dt \quad , \qquad (4\text{-}17)$$

the aerodynamic work was obtained by multiplying together signals generated on the analog computer. These signals represented the aerodynamic moment and the airfoil angular rate. Then, this product was integrated over a time interval which covered a complete cycle of airfoil oscillation.

Figure 4-9 shows the analog and DES-30 mechanizations which

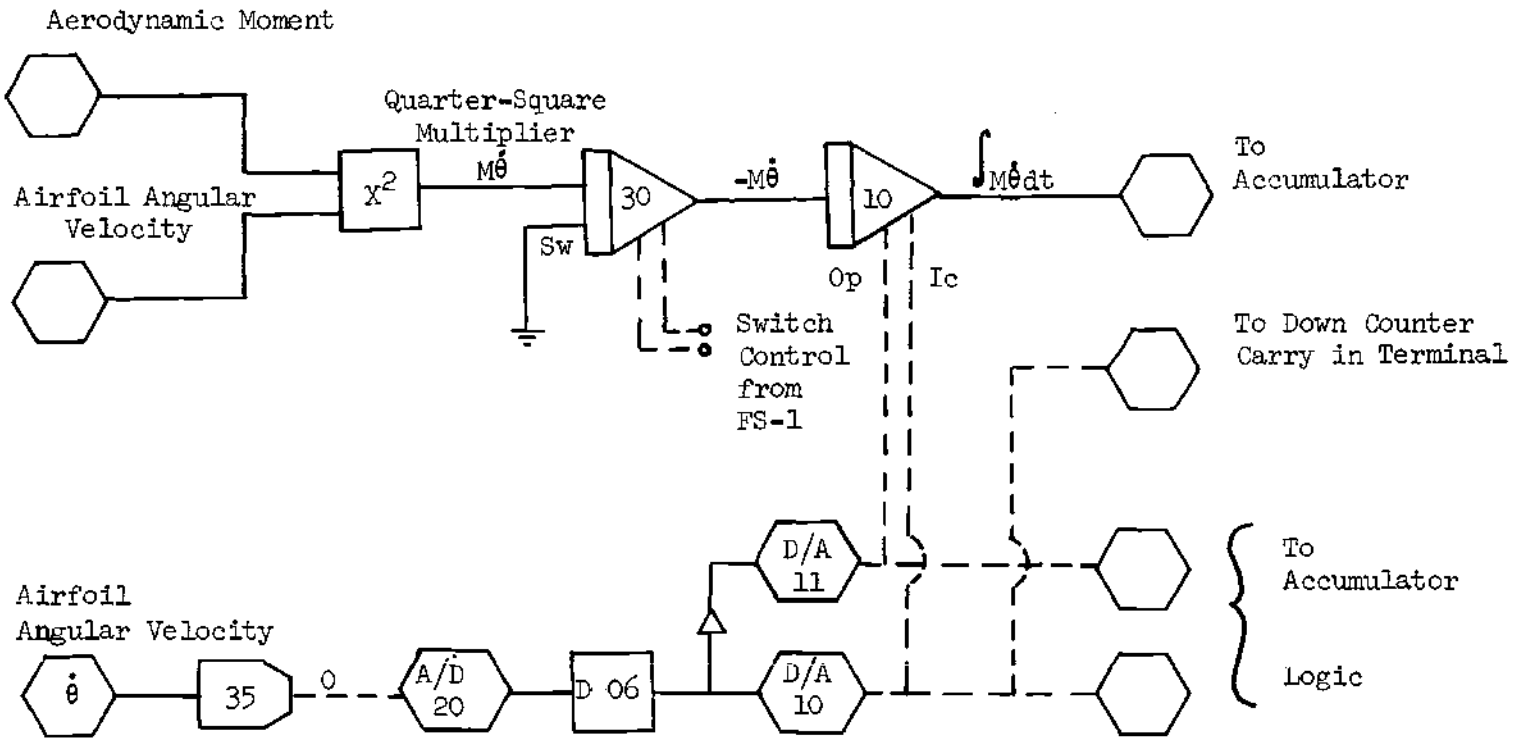

Figure 4-9. Mechanization Used to Determine Airfoil Work per Cycle

were used to generate the aerodynamic work per cycle. The moment and angular rate signals were multiplied using a quarter-square multiplier. This signal was then applied to an integrating amplifier, I10, whose output represented the work done on the airfoil during each cycle.

Logic signals generated by the DES-30 were used to switch the work integrator momentarily from the operate mode into the initial condition mode each time the airfoil passed through its maximum angle of attack. To accomplish this, a differentiator unit, D06, in the DES-30 was used to create a pair of blip trains which provided the proper switching logic to the integrator OP and IC bus lines. Figure 4-10 illustrates the timing relationships between the differentiator input signals and the airfoil accelerometer signal.

At the end of each cycle of oscillation, the output of integrator I10 was stored in an accumulator circuit. This circuit consists of two track and store units connected in series, together with a feedback connection from the output of the second, to the input of the first track and store unit (see Reference 21). Since all of the track and store units available on the TR-48 were used for other circuits, two integrating amplifiers had to be patched as track and store units for the accumulator unit (see Figure 4-11).

The accumulator circuit was mechanized as shown in Figure 4-12. The same logic signals which controlled the work integrator were used to control the accumulator unit. The feedback input to track and store unit I09 was obtained by patching the IC resistor network of an unused integrator into the IC network of I09.

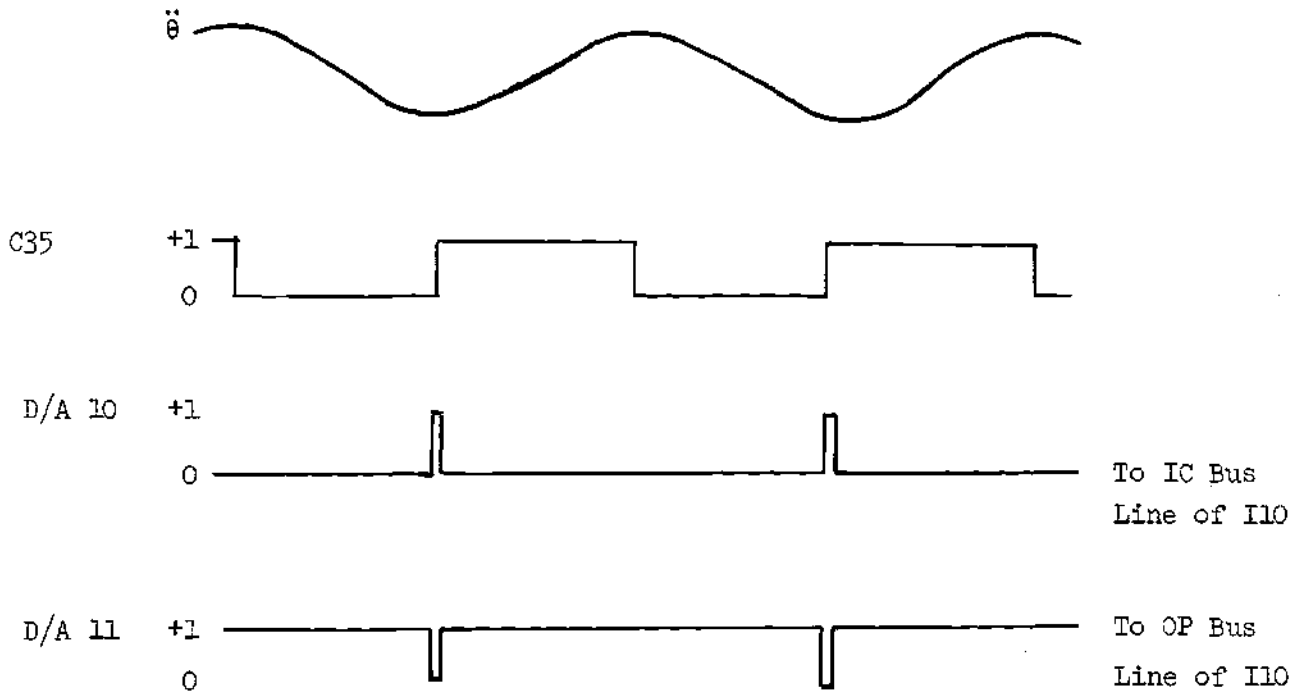

Figure 4-10. Timing Sequences Used to Control Work Integrator and Accumulator Unit

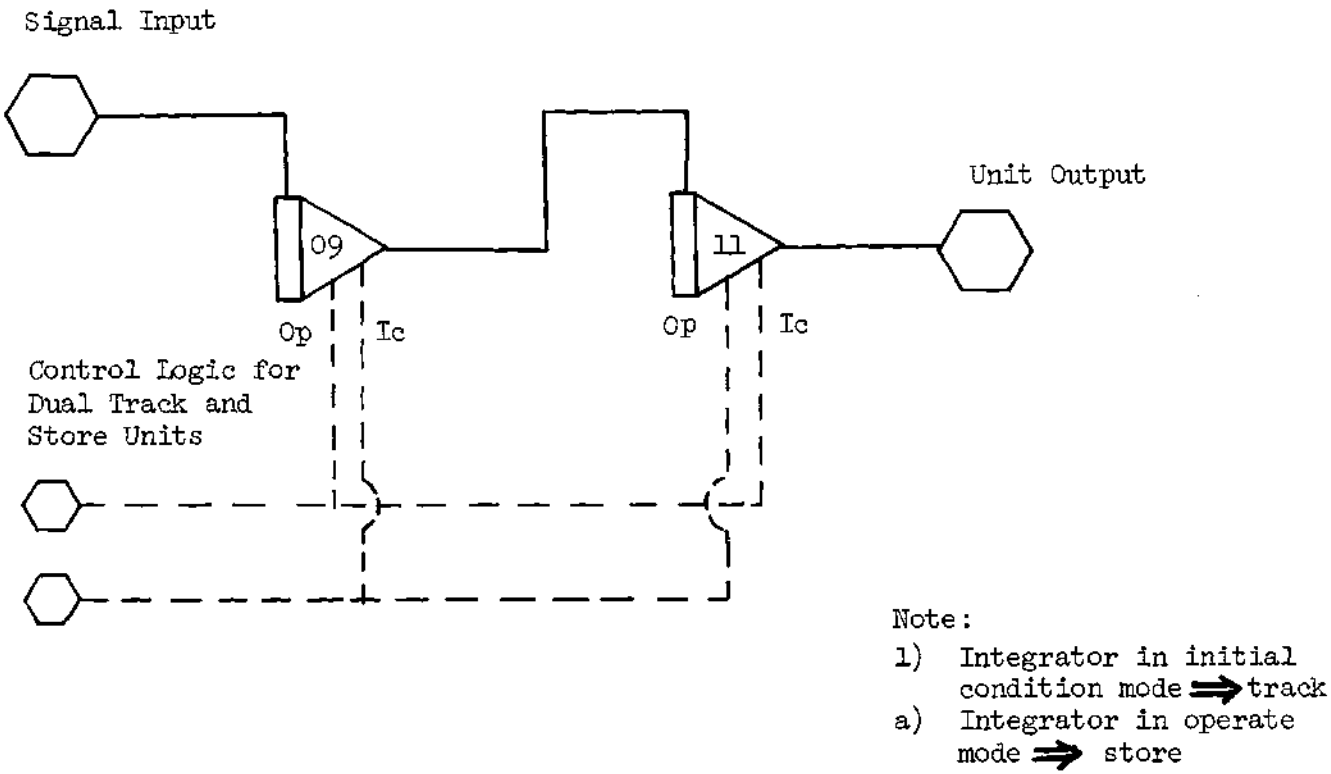

Figure 4-11. Two Integrators Patched as Dual Track and Store Units

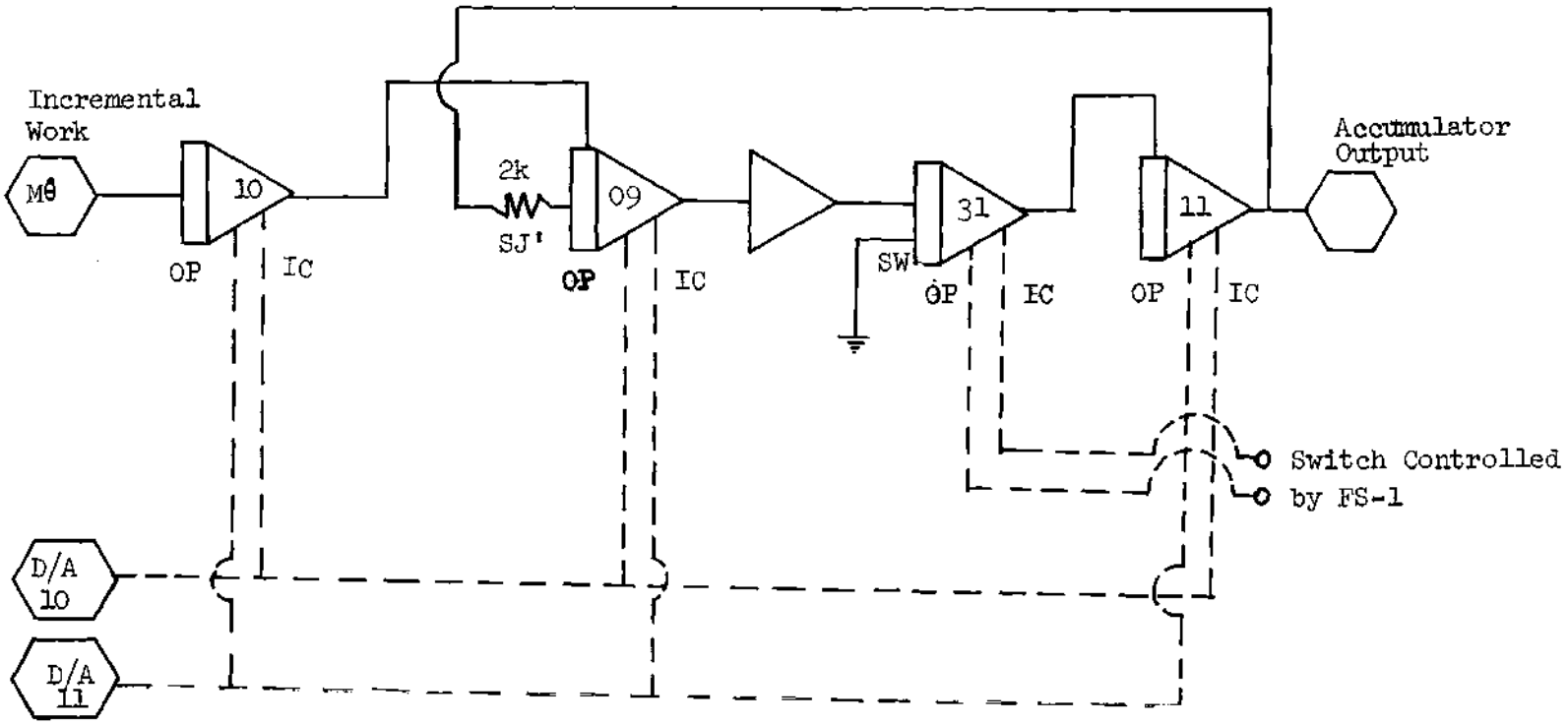

Figure 4-12. Mechanization for Accumulator Circuit Used to Determine Average Airfoil Work per Cycle

During operation of the accumulator, the output of I11 was incremented by a voltage of equal to the work done on the airfoil during each cycle of oscillation. The output of I11 was then monitored on a digital voltmeter. However, since this voltage reading changed at the same rate as the airfoil oscillation frequency (5 to 20 Hz), the individual values of the work per cycle could not be recorded. Therefore, it became necessary to control the operation of the accumulator unit by starting the accumulator at the beginning of a cycle, and then stopping it after a specified number of completed cycles. The final voltage displayed on the digital voltmeter then represented the sum of the work done per cycle, over a given number of airfoil cycles of oscillation.

The electronic switches in integrators I30 and I31 were used to start the accumulator at a specific instant of time. These switches were activated by logic signals from the main integrator mode control circuit (see Figure 4-4). On activation, one switch applied the signal representing incremental work, $M\dot{\theta}$, to the integrator I10, while the other switch completed the circuit path for the accumulator unit (see Figures 4-9 and 4-12).

The DES-30 was used to stop the accumulator after a given number of cycles. This was accomplished by using a second pair of electronic switches, I02 and I03, to control the mode logic for the work integrator and the accumulator unit. When deactivated, these switches admitted the control logic from the differentiator D06 (see Figure 4-9) directly to the OP and IC bus lines of the work integrator and the accumulator, thus allowing these units to cycle

periodically. However, when I02 and I03 were activated, both the OP and IC logic signals dropped to zero, placing integrating amplifiers, I09, I10, and I11 in the hold mode. While in this hold mode, the final output of the accumulator could be read directly off the digital voltmeter.

A down counter and a pair of flip-flop units were used to activate switches I02 and I03 after a specified number of cycles. The patching for these units is shown in Figure 4-13. The down counter was first set to a specific number of cycles, N. A blip train was then applied to the down counter through an electronic switch, I32. After N + 1 input blips, a carryout blip from the down counter caused the pair of flip-flops to set. The output signals from the second flip-flop unit then activated the electronic switches in I02 and I03, placing the accumulator and work integrator in the hold mode.

Airfoil Lift Force

The lift acting on the airfoil model was obtained using both the lift load cells and the two lift strain gage bridges. The analog mechanization which was used with the load cells is shown in Figure 4-14. The calibration constants for potentiometers P01 and P02 were obtained from Figures 3-11 and 3-12. Potentiometer P03 was used to eliminate the inertial lift contribution by zeroing the lift signal during wind off airfoil oscillations.

The mechanization which was used with the strain gage bridges is shown in Figure 4-15. Potentiometer P01 was used to eliminate the D.C. signal corresponding to the model weight. The calibration constant for P02 was obtained from Figure 3-13. As in the previous mechanization,

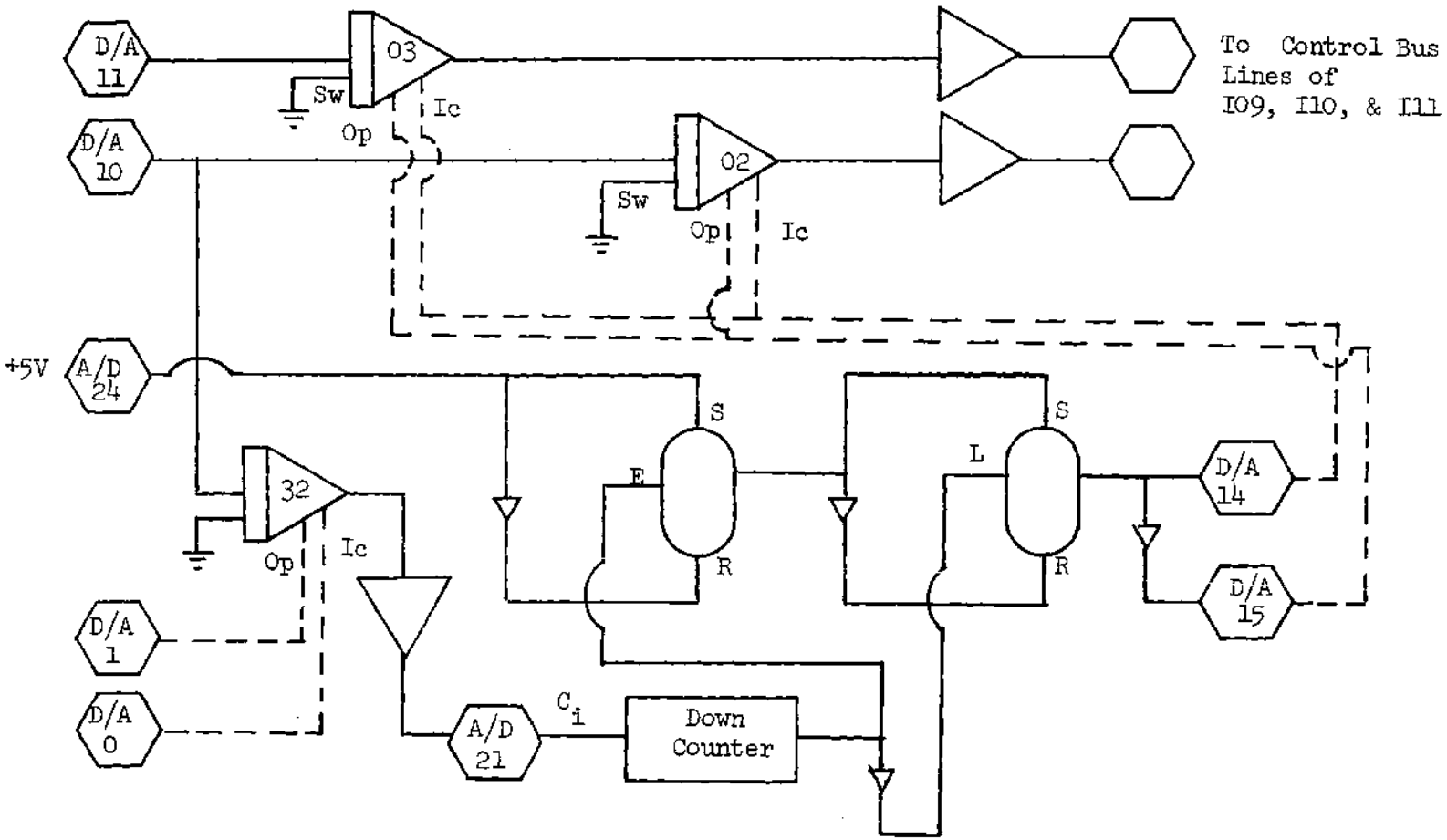

Figure 4-13. Mechanization for Down Counter and Switching Control for Work Integrator and Accumulator Unit.

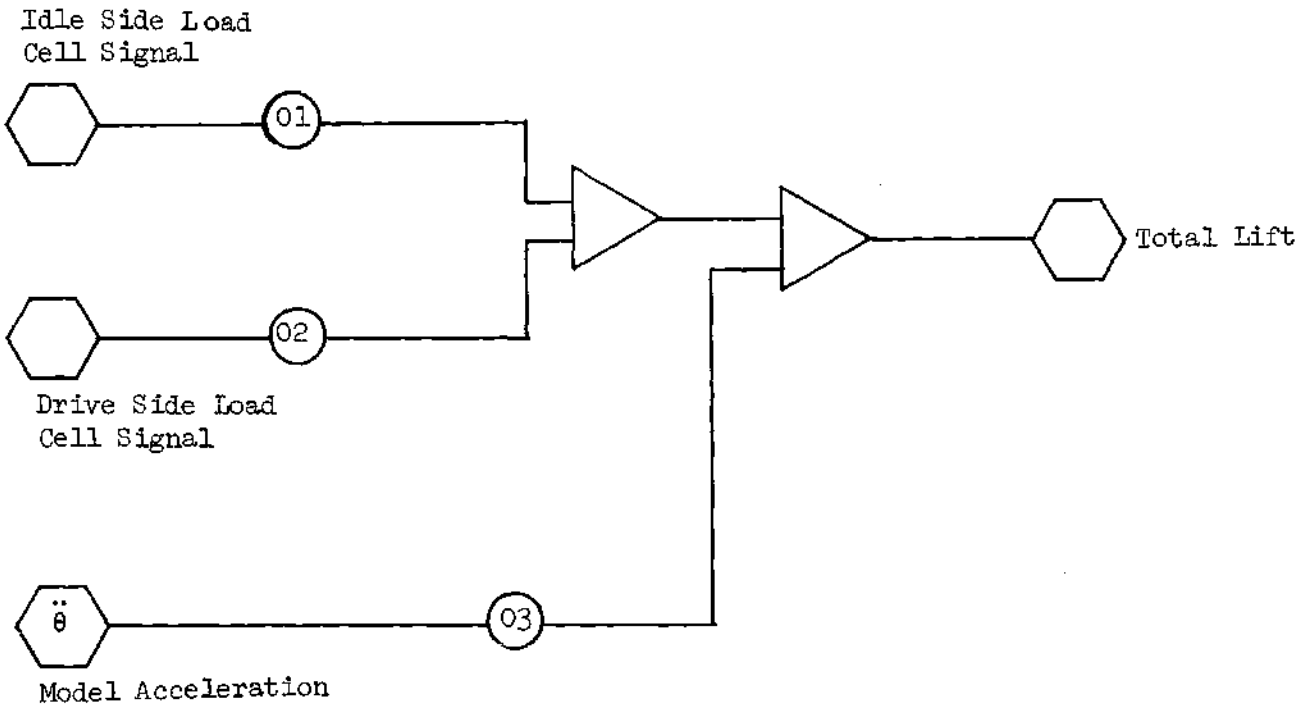

Figure 4-14. Mechanization Used with Lift Load Cells

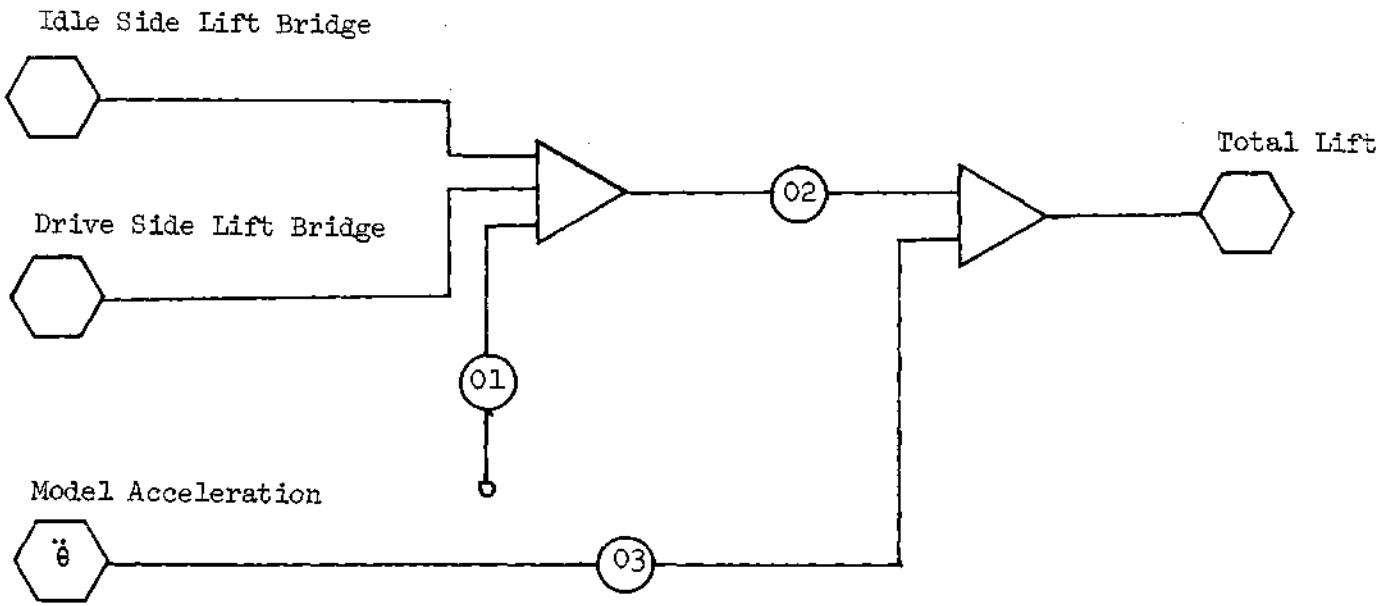

Figure 4-15. Mechanization Used with Lift Strain Gage Bridges

P03 was used to cancel out the inertial contributions to the lift signal.

Determination of Mean Freestream Velocity

During the experimental work performed in the gust generator facility, the wind tunnel velocity was determined using a hot wire located upstream of the tunnel test section (see Figure 2-1). Figure 4-16 shows the calibration data obtained for this hot wire, together with the second order least squares fit for the data.

In order to prevent damage to the gust generator mechanism from steady aerodynamic loading, the vanes were set in motion prior to turning on the wind tunnel. Using this starting procedure, the hot wire output continuously fluctuated with the velocity. This made it impossible to set the wind tunnel to a predetermined mean speed using only the instantaneous hot wire output.

Therefore, it became necessary to use the analog computer to determine the wind tunnel mean speed. The mechanization that was used (see Reference 22) is shown in Figure 4-17. With the instantaneous hot wire signal applied to potentiometer P01 , the output of integrator I01 increased with time until it reached the value of the mean hot wire voltage. The potentiometer settings for P01 and P02 were set to equal values. These settings determined how fast the output of I01 reached the mean value of the input signal.

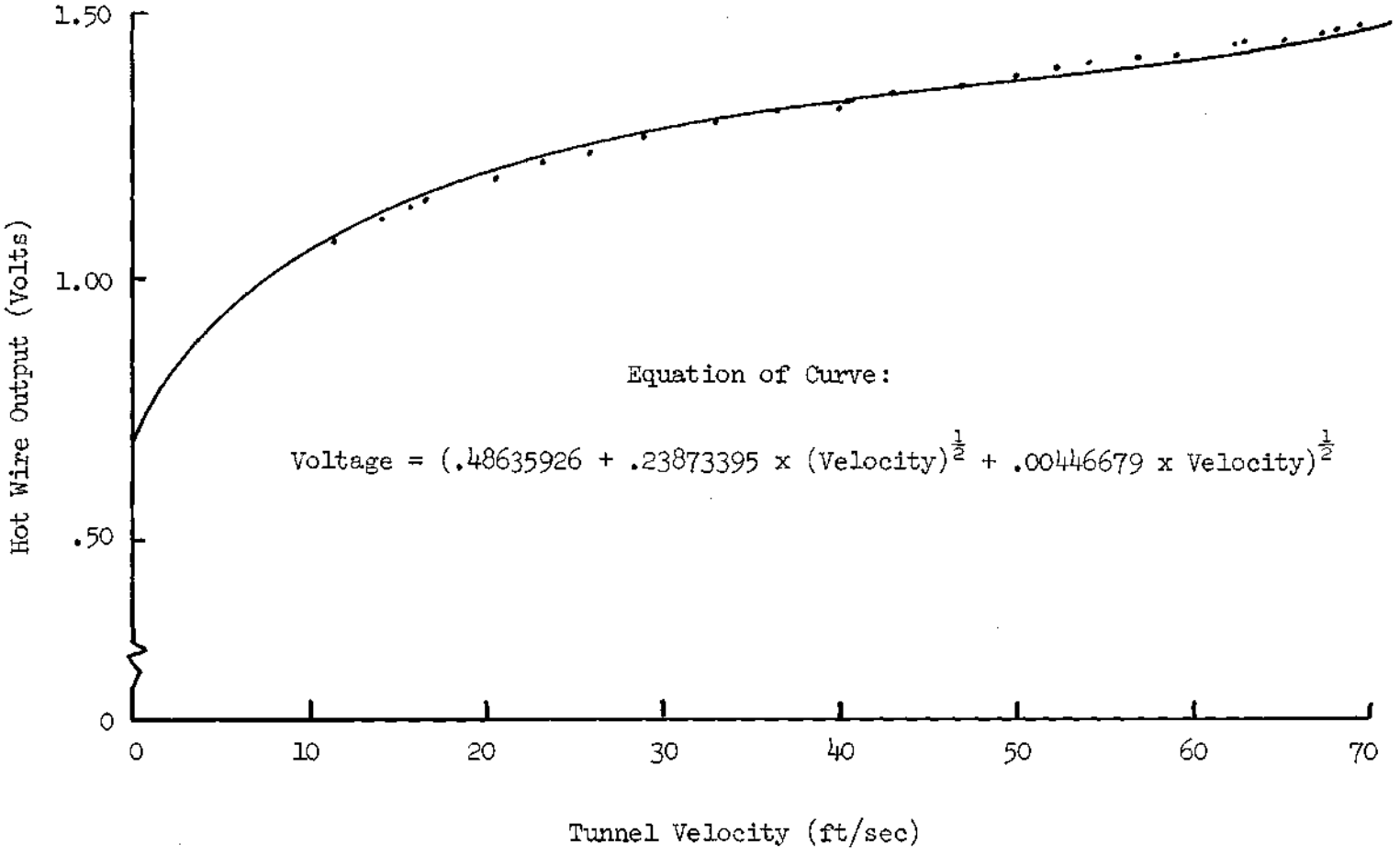

Figure 4-16. Calibration Curve for Tunnel Speed Hot Wire

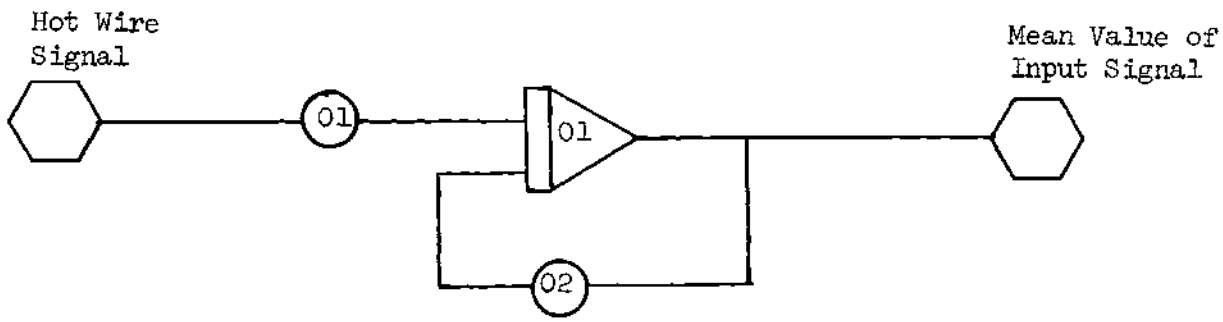

Figure 4-17. Mechanization Used to Determine Mean Wind Tunnel Velocity

CHAPTER V

DATA REDUCTION

The purpose of the experimental work performed for these studies was to investigate the effects of an unsteady freestream on the aerodynamic characteristics of an oscillating airfoil. The lift force and aerodynamic moment acting on the oscillating airfoil were determined, both for the case of a steady freestream, and for the case of a harmonically varying freestream. In addition, the average work per cycle acting on the airfoil during pitching oscillations was determined for each cycle of airfoil oscillation.

Experimental Procedures

Prior to taking data in the gust generator facility, the airfoil oscillating mechanism was tested using both the rigid and elastic linkages. During these tests, the signals from the load cells and the strain gage bridges were monitored on an oscilloscope. The waveforms obtained from these two types of transducers were then compared at various frequencies of airfoil oscillation.

The results of the forced-rigid oscillation tests indicated that both the load cell and strain gage output signals were distorted by high frequency noise. The waveforms from the moment strain gage bridge were less erratic than those produced by the corresponding moment load cell and both lift signals. Results of tests conducted with the elastic linkage installed in the mechanism showed a large improvement

in both the moment load cell and moment bridge signals, without however, a corresponding improvement in the signals from the lift transducers.

These preliminary tests indicated that the elastic linkage isolated the drive arm transducers from the high frequency vibrations which affected the lift transducers. Because of this isolation effect, it was concluded that the most likely sources of the signal distortions in the system were the main bearings used to support the model shaft.

An amplitude modulation of the applied moment signal was noticed during forced-elastic oscillations of the airfoil. This effect occurred even with the gust generator vanes held motionless and in a horizontal position. The modulation was quite apparent in the load cell and strain gage bridge outputs, and appeared during both wind off and wind on tunnel operation. From a search of experimental literature, it was concluded that this phenomena might possibly be caused by either viscous damping or spring inertia effects [23-24].

From the results of the preliminary testing conducted with the airfoil oscillating mechanism, it was decided to use only the rigid linkage during forced airfoil oscillations to obtain the data for this investigation. A flow chart of the electronic equipment used in the experiment is shown in Figure 5-1.

The applied moment signal was obtained from the strain gage bridge and then filtered through a Krohn-Hite low-pass filter to eliminate the high frequency noise present. The model acceleration signal was also filtered through a Krohn-Hite low-pass filter and a Special Dynamics narrow (10 Hertz) bandpass filter, Model SD 101B. The acceleration signal from the Krohn-Hite unit was used to continuously

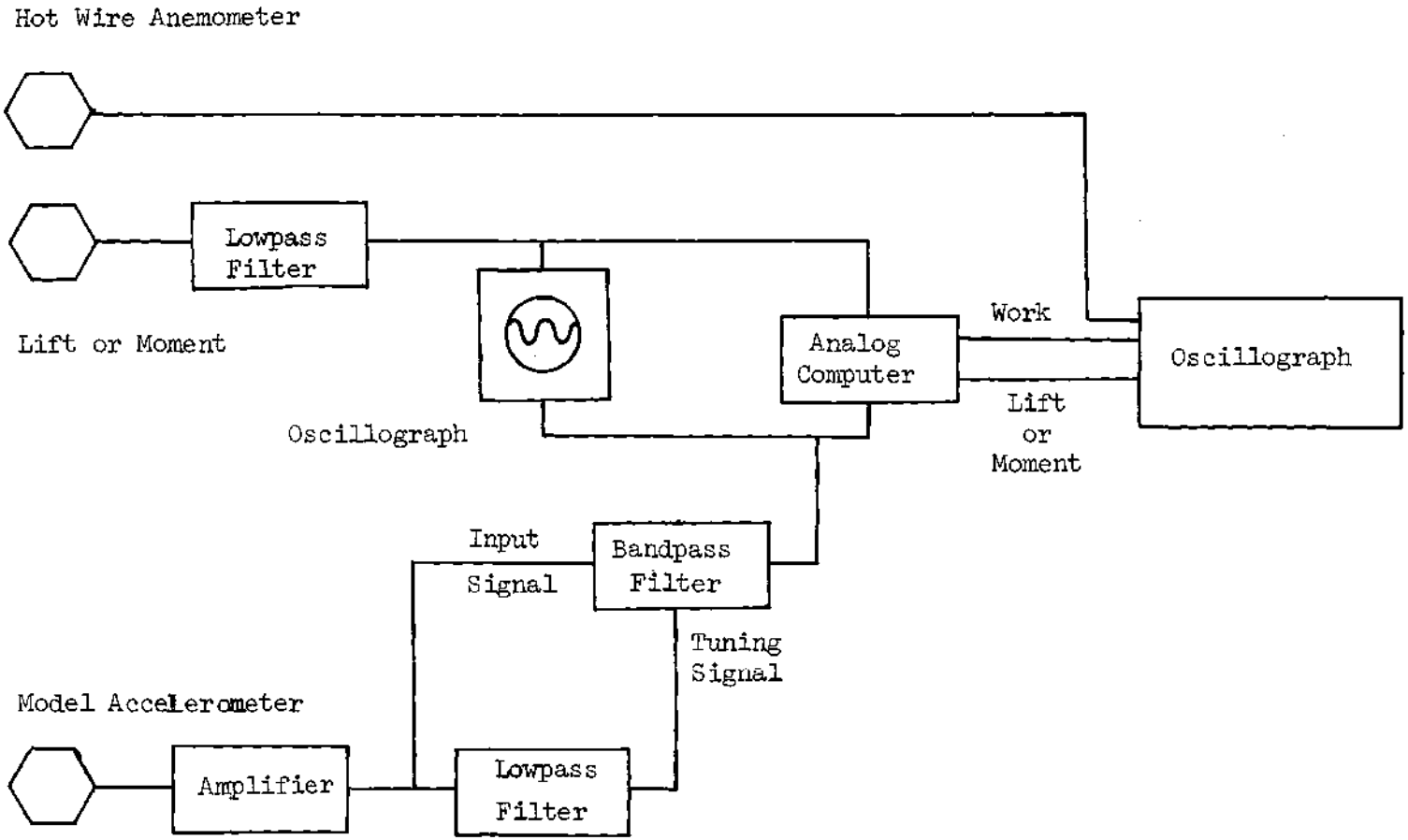

Figure 5-1. Electronic Equipment Used for Rigid-forced Airfoil Oscillation Tests

in both the moment load cell and moment bridge signals, without however, a corresponding improvement in the signals from the lift transducers.

These preliminary tests indicated that the elastic linkage isolated the drive arm transducers from the high frequency vibrations which affected the lift transducers. Because of this isolation effect, it was concluded that the most likely sources of the signal distortions in the system where the main bearings used to support the model shaft.

An amplitude modulation of the applied signal was noticed during forced-elastic oscillations of the airfoil. This effect occurred even with the gust generator vanes held motionless and in a horizontal position. The modulation was quite apparent in the load cell and strain gage bridge outputs, and appeared during both wind off and wind on tunnel operation. From a search of experimental literature, it was concluded that this phenomena might possibly be caused by either viscous damping or spring inertia effects [23-24].

From the results of the preliminary testing conducted with the airfoil oscillating mechanism, it was decided to use only the rigid linkage during forced airfoil oscillations to obtain the data for this investigation. A flow chart of the electronic equipment used in the experiment is shown in Figure 5-1.

The applied moment signal was obtained from the strain gage bridge and then filtered through a Krohn-Hite low-pass filter to eliminate the high frequency noise present. The model acceleration signal was also filtered through a Krohn-Hite low-pass filter and a Spectral Dynamic narrow (10 Hertz) bandpass filter, Model SD 101B. The acceleration signal from the Krohn-Hite unit was used to continuously

center the narrow bandpass filter at the airfoil oscillation frequency. The output signal from this filter could also be phase shifted up to 180 degrees with respect to the input signal.

To subtract the inertial contribution from the signal representing the total applied moment, it was necessary to first match the phase of the strain gage bridge signal and the accelerometer signal. The phase difference between these two signals was the result of two factors: the Kistler amplifier used with the accelerometer produced a phase shift at frequencies below twenty Hertz; and, the output of the strain gage bridge was proportional to the drive arm bending stresses, whereas the accelerometer output was proportional to the model acceleration.

The phase difference between the acceleration and applied moment was minimized by applying the two signals to the horizontal and vertical inputs of an oscilloscope. Thus, a Lissajous diagram obtained which could be used in aligning the signals. The phase of the output signal from the narrow bandpass filter was then adjusted until the Lissajous diagram formed a straight line, indicating that the strain gage output was in phase with the accelerometer output. This same procedure was used to match the phase of the lift strain gage outputs and the model accelerometer signal.

The analog computer was used as described in Chapter IV to obtain the airfoil aerodynamic moment and work per cycle of oscillation. The signals representing these quantities were recorded on a Honeywell, fourteen track oscillograph. In addition, the output signal from the hot wire anemometer was recorded so that the phase between the free-stream velocity and the aerodynamic forces could be determined.

The airfoil model and the gust generator vanes were operated using separate motors and drive mechanisms. Because of this, the phase relationship between the airfoil displacement and the tunnel velocity could not be directly controlled at any time during the experiments. In addition, the operation of the analog computer was coordinated with airfoil displacement, and not with the tunnel velocity. Since the work integrator, I10, was operated with a manual switch, the value of the tunnel velocity at the instant the integrator was started, could only be determined after the test run.

To minimize the effects that this velocity-displacement phase angle might have on the aerodynamic work, average values of work per cycle of airfoil oscillation were determined over several cycles of freestream fluctuation. The analog computer accumulator circuit was used to sum the individual values of work per cycle. Then, the final accumulator output was divided by the total number of cycles of airfoil oscillation to obtain a voltage which represented the average value of work per cycle.

During operation of the analog computer, the machine voltages were kept within the required levels by the use of scaling factors. The actual values of lift, moment, and work could then be obtained by multiplying the analog output voltages times the appropriate scaling factors.

The aerodynamic work data were non-dimensionalized in the usual manner using the airfoil model dimensions. The reference dynamic pressure used for these tests was based on the mean tunnel airspeed, V_o. The equation for the work coefficient is given below

$$C_W = \frac{\text{Work}}{\frac{1}{2}\rho V_o^2 bc^2} \qquad (5\text{-}1)$$

Typical Results

Figures 5-2 through 5-6 illustrate the effects of frequency ratio, F_R, and mean angle of attack on the shape of the characteristic aerodynamic moment versus angle-of-attack curve for the airfoil. For this investigation, the frequency ratio is defined as

$$F_R = \frac{\text{frequency of airfoil oscillation}}{\text{frequency of freestream oscillation}} \qquad (5\text{-}2)$$

The area enclosed by the curve in each plot represents the work done on the airfoil. A counter-clockwise rotation as the curve is traversed denotes negative work, while a clockwise rotation represents positive work. When the aerodynamic moment does positive work on the airfoil, an unstable condition exists since energy can be absorbed from the freestream by the structure. Thus, it is important to determine the conditions which produce a positive value of work coefficient for the airfoil.

During the experimental tests, it was not always possible to completely cancel out in the analog computer the inertial moment contribution to the total applied moment signal. This was due to the signal distortions caused by bearing friction and low frequency noise (i.e., noise frequencies less than the airfoil oscillation frequency). Thus, in the wind off condition, a small value of work was at times recorded on the analog computer. To account for this condition, the actual, or net,

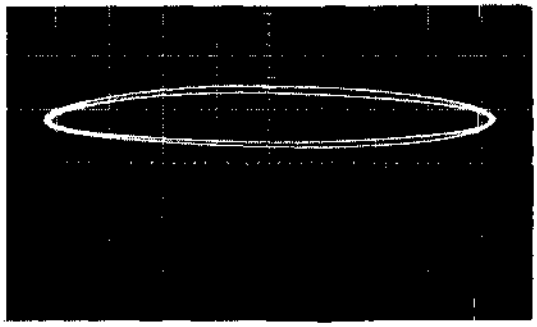

a) $F_R = \infty$; $\theta_o = 0^\circ$

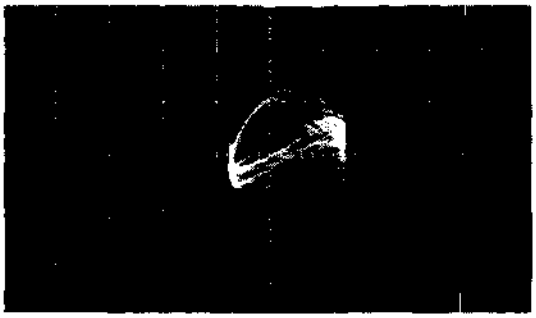

b) $F_R = 10$; $\theta_o = 4^\circ$

Figure 5-2. Aerodynamic Moment versus Angle of Attack for $\Delta\theta = \pm 2^\circ$

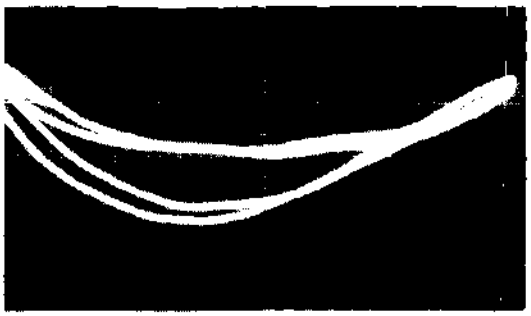

a) $F_R = \infty$; $\theta_o = 2^\circ$

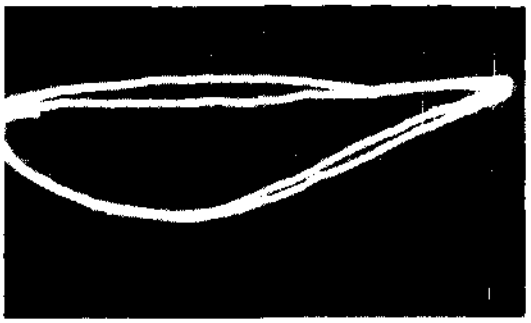

b) $F_R = 6$; $\theta_o = 2^\circ$

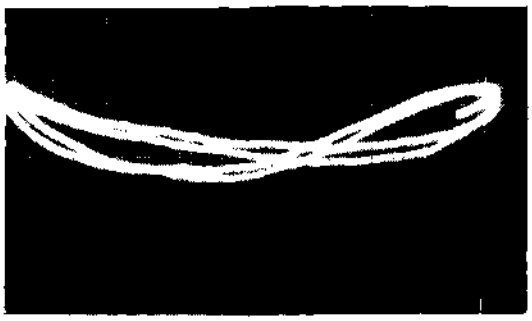

c) $F_R = 10$; $\theta_o = 2^\circ$

Figure 5-3. Aerodynamic Moment versus Angle of Attack for $\Delta\theta = \pm 4^\circ$

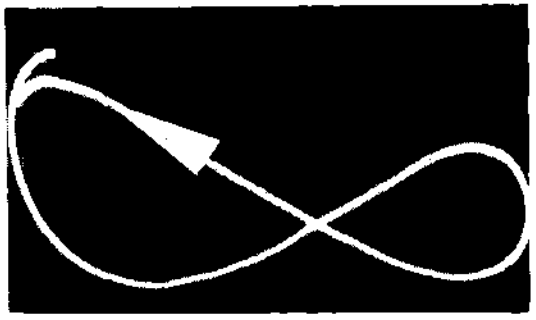

a) $F_R = \infty$; $\theta = 12^\circ$

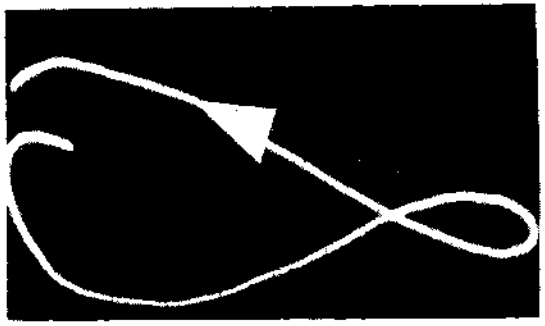

b) $F_R = 15$; $\theta_o = 12^\circ$

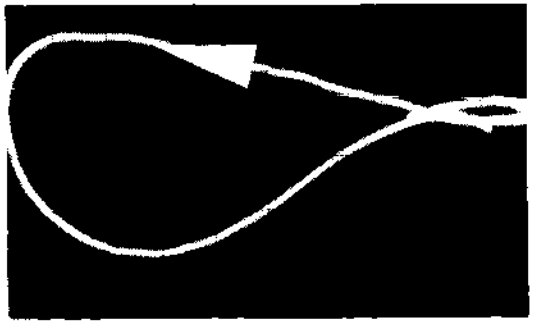

c) $F_R = 15$; $\theta_o = 12^\circ$

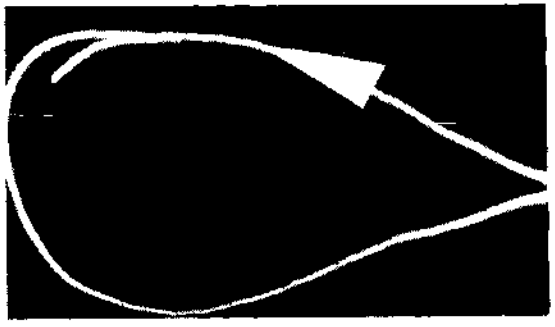

d) $F_R = 15$; $\theta_o = 12^\circ$

Figure 5-4. Aerodynamic Moment versus Angle of Attack for $\Delta\theta = \pm 4^\circ$

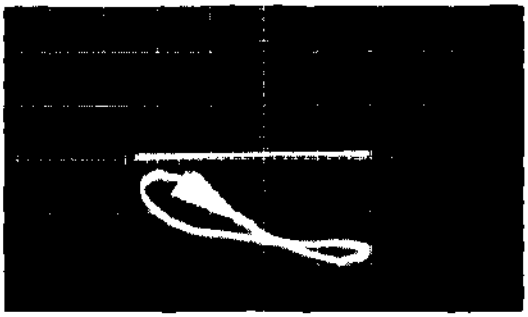

a) VELOCITY = 19.1 ft/sec

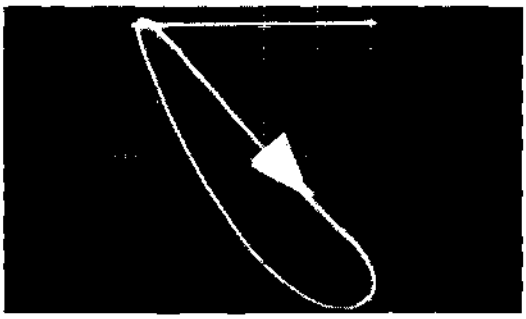

b) VELOCITY = 32.4 ft/sec

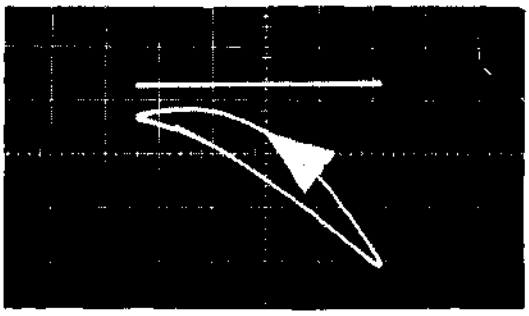

c) VELOCITY = 45.3 ft/sec

Figure 5-5. Moment versus Angle of Attack Loops for Constant Freestream Velocities. ($\theta_o = 16^\circ$, $\Delta\theta = \pm 4^\circ$, Airfoil Frequency = 600 RPM)

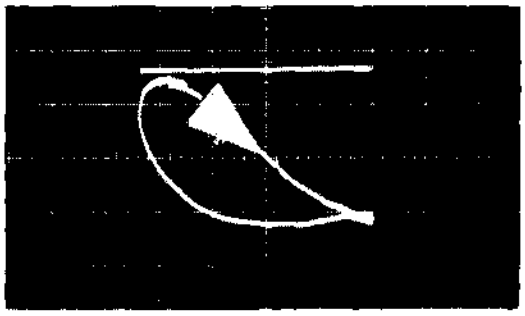

a) VELOCITY = 19.1 ft/sec

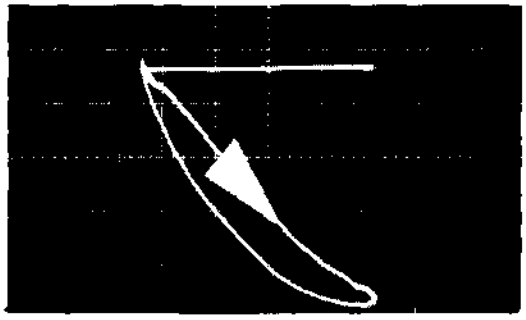

b) VELOCITY = 32.4 ft/sec

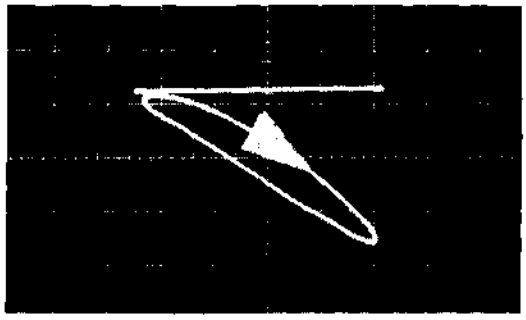

c) VELOCITY = 45.3 ft/sec

Figure 5-6. Moment versus Angle of Attack Loops for Axial Gust Frequency of 40 RPM, ($\theta_o = 16^\circ$, $\Delta\theta = \pm 4^\circ$, Airfoil Frequency = 600 RPM)

value of aerodynamic work was obtained by subtracting the wind off work from the wind on value.

For a constant freestream velocity, Figure 5-2a illustrates the elliptical shape of the moment versus angle loop which occurs at low mean angles of attack. Figure 5-2b is a composite photograph of the changes in this moment loop caused by a harmonic variation in the free-stream velocity. These changes in the moment loop can be quite large, and can in turn, greatly alter the aerodynamic work done on the airfoil.

Figure 5-3 shows the effect of frequency ratio on the moment loop for a larger amplitude of airfoil oscillation. The loop corresponding to an infinite frequency ratio (i.e., constant velocity) is no longer elliptical in shape. The loops for finite values of F_R illustrate the two ways in which the work per cycle can be altered. In Figure 5-3b, the work has changed due to the expansion of the loop. In Figure 5-3c the loop has crossed over itself, thereby causing one half of the loop to be traversed in a clockwise direction, and the other half in a counter-clockwise direction. The total work for this cross-over loop is then found by algebraically adding the amounts of positive and negative work.

Figure 5-4 illustrates how a moment loop, which normally crosses over itself in a constant freestream velocity, can become a simple loop when the freestream is unsteady. After taking into account the wind off value of aerodynamic work, the loop in Figure 5-4a represents a net positive amount of work being done on the airfoil as it oscillates into and out of the stall region. At a finite value of frequency ratio, the

moment loop begins to uncross in Figure 5-4b. Figure 5-4c and 5-4d show the loop shape changing progressively until, as shown in Figure 5-4d, the loop is traversed totally in a counter-clockwise direction. The stabilizing effect of the freestream gust illustrated by these photographs is reflected in the average work per cycle obtained from the analog computer, as shown below.

For $\theta_o = 12^\circ$, $\Delta\theta = \pm 4^\circ$, $V_o = 30$ ft/sec

F_R	C_W average work/cycle
00	+ .00778
15	- .00308

Figures 5-5 and 5-6 illustrate a test condition for which the effects of an axial gust are destabilizing. In Figure 5-5 the moment versus angle-of-attack loops are shown for three different constant freestream velocities. In Figure 5-5c the moment loop is traversed in a counter-clockwise direction, while in Figures 5-5a and 5-5b the loops are in the clockwise direction.

The photographs in Figure 5-6 were taken as the speed of the velocity gust passed through values corresponding to the three constant velocities of Figure 5-5. In the presence of an axial gust, however, all three loops are traversed in a clockwise direction, denoting positive work done during airfoil motion throughout the gust cycle. For this test condition, the use of constant freestream data to predict the work done on an oscillating airfoil would produce non-conservative

results.

During this experimental investigation, the average work coefficient per cycle of oscillation was obtained for mean angles from zero to twenty degrees, and for several values of frequency ratio. The frequency ratio was varied by keeping the model oscillation frequency constant and changing the gust frequency. This method was picked because of the lengthly set up time required when using the tracking filters to cancel out the inertial moment signal.

The experimentally determined work coefficient is plotted in Figures 5-7 through 5-10 for constant values of frequency ratio. For small amplitudes of airfoil oscillation the maximum positive work coefficient increases inversely with frequency ratio, the maximum for these tests, thus occurring at $F_R = 5$ (see Figures 5-7 and 5-8). For a larger oscillation amplitude, $\Delta\theta = \pm 6^\circ$, this trend is repeated, with a positive work coefficient occurring only for the smaller values of frequency ratio (see Figure 5-9). During the largest oscillating amplitude tests, the work coefficient remains predominately negative throughout the range of mean angles tested (see Figure 5-10).

In Figures 5-11 to 5-12 the work coefficient is replotted versus frequency ratio for constant values of mean angle. For oscillation amplitudes of four degrees (see Figure 5-12) the maximum negative work coefficients occur at frequency ratios of between five and six.

The work coefficient data plotted in Figures 5-7 to 5-12 was subject to a certain amount of fluctuation during the experimental tests. Table 5-1 illustrates typical variations in C_W which occurred for two

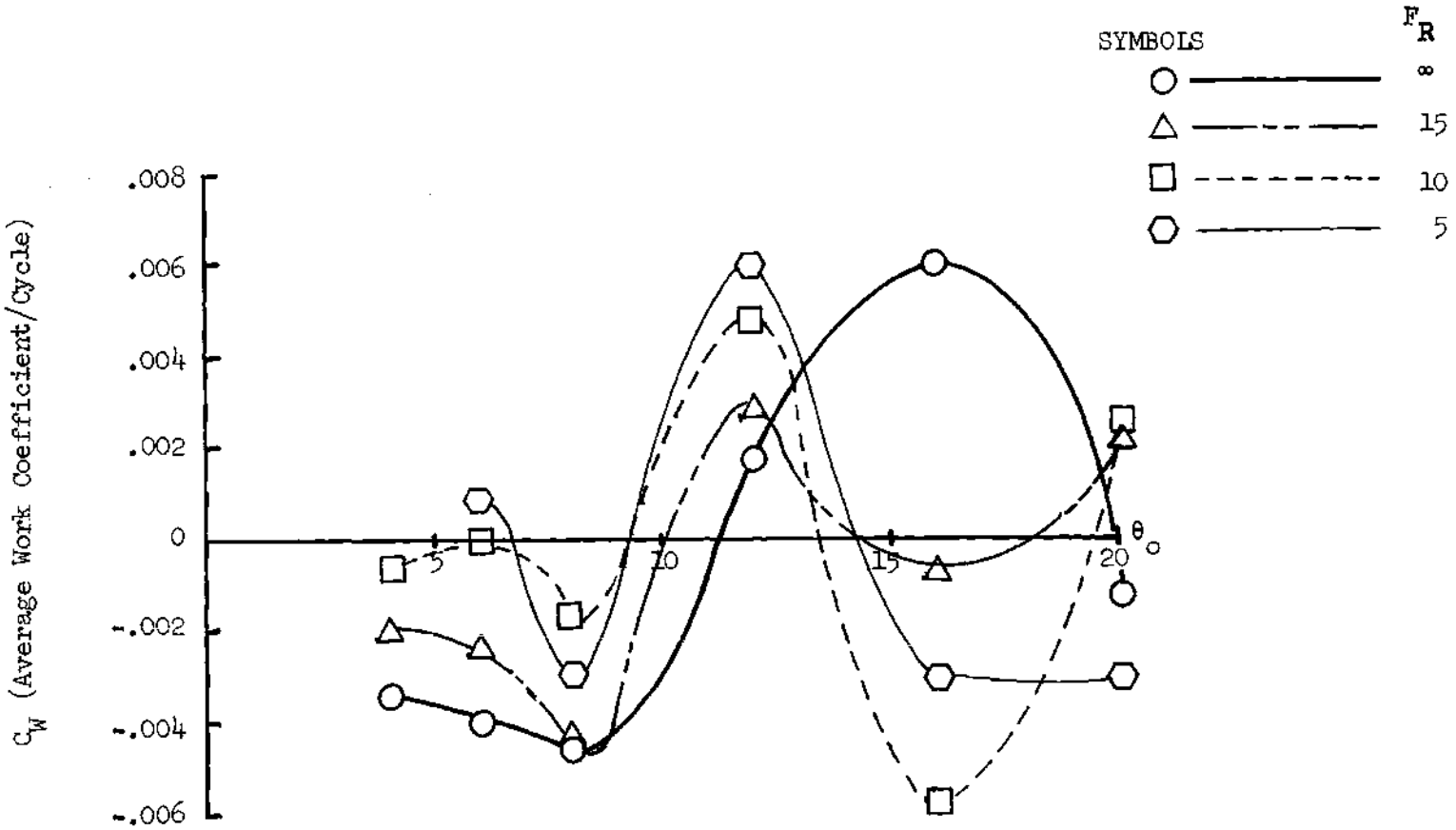

Figure 5-7. Work Coefficient Versus Mean Angle for $\Delta\theta = \pm 2°$

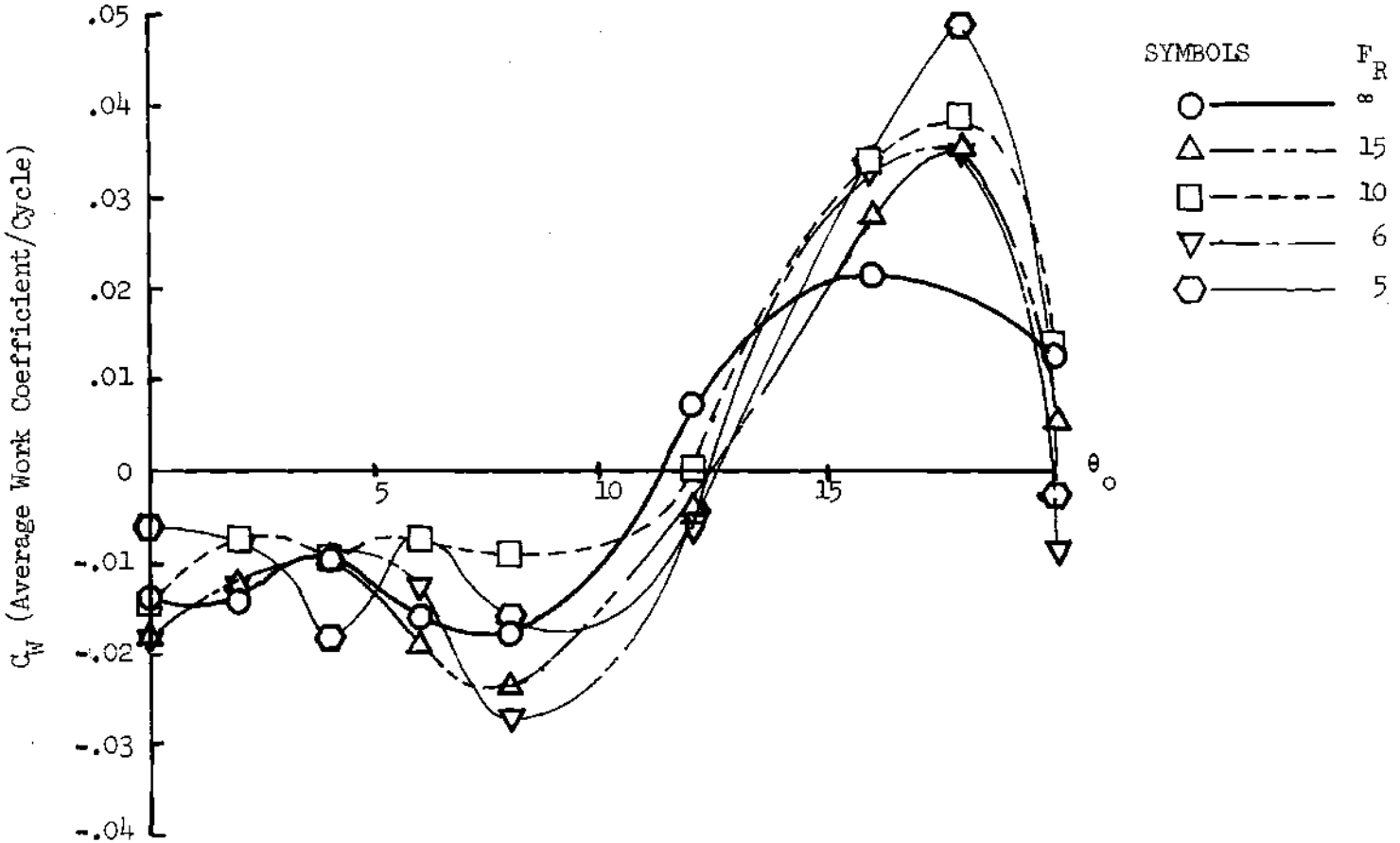

Figure 5-8 . Work Coefficient Versus Mean Angle for $\Delta\theta = \pm 4^\circ$

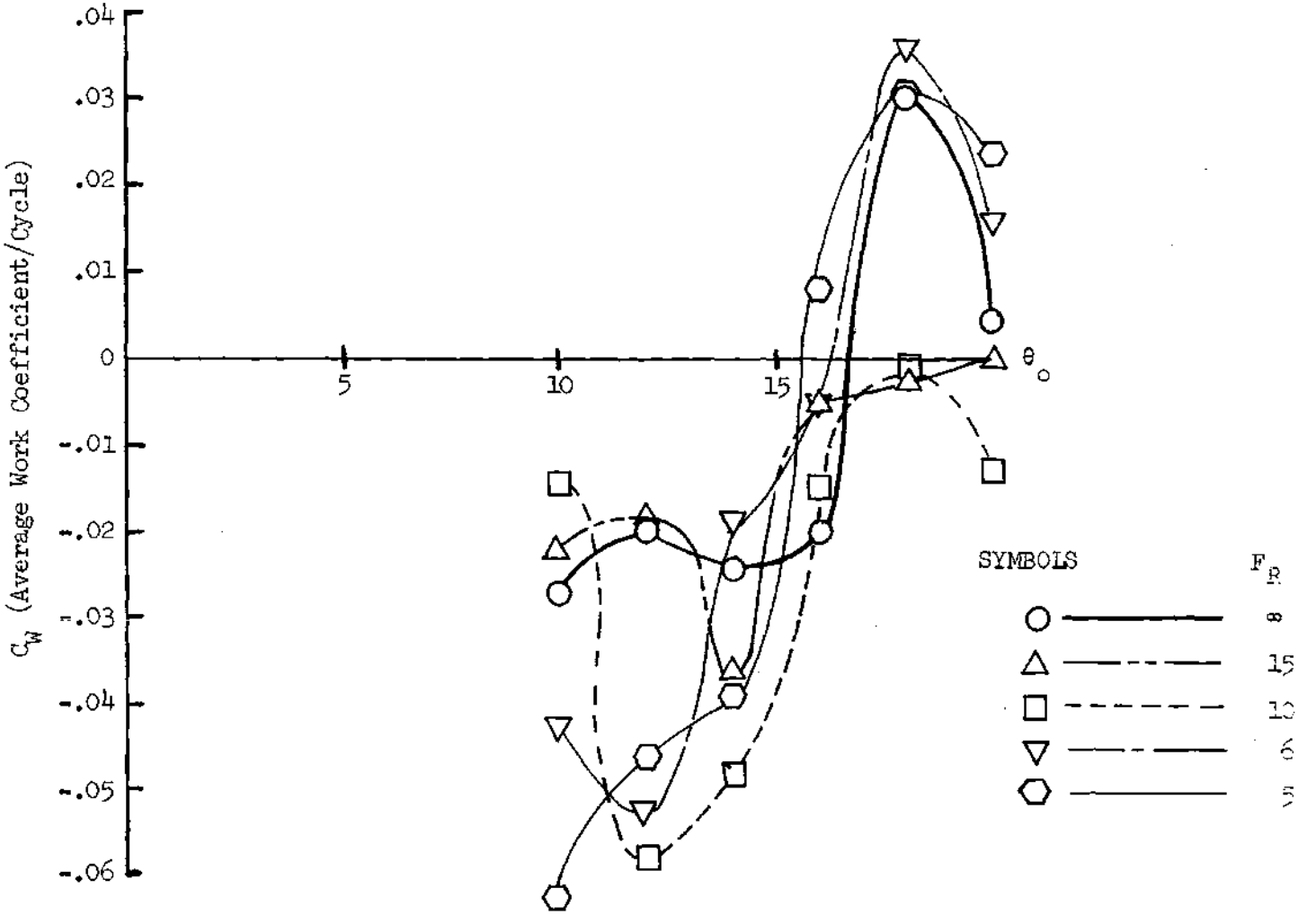

Figure 5-9. Work Coefficient Versus Mean Angle for $\Delta\theta = \pm 6°$

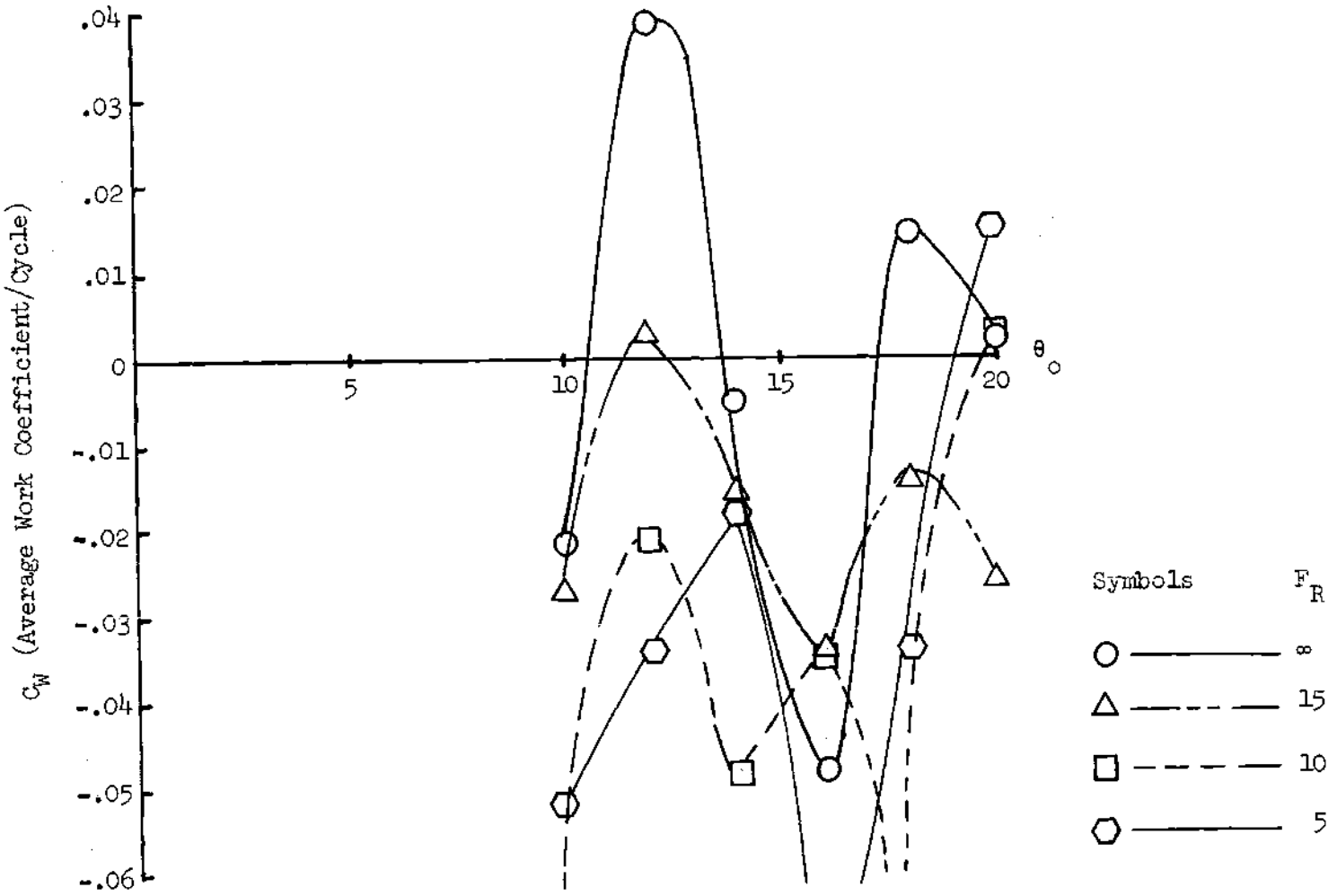

Figure 5-10. Work Coefficient versus Mean Angle for $\Delta\theta = \pm 8°$

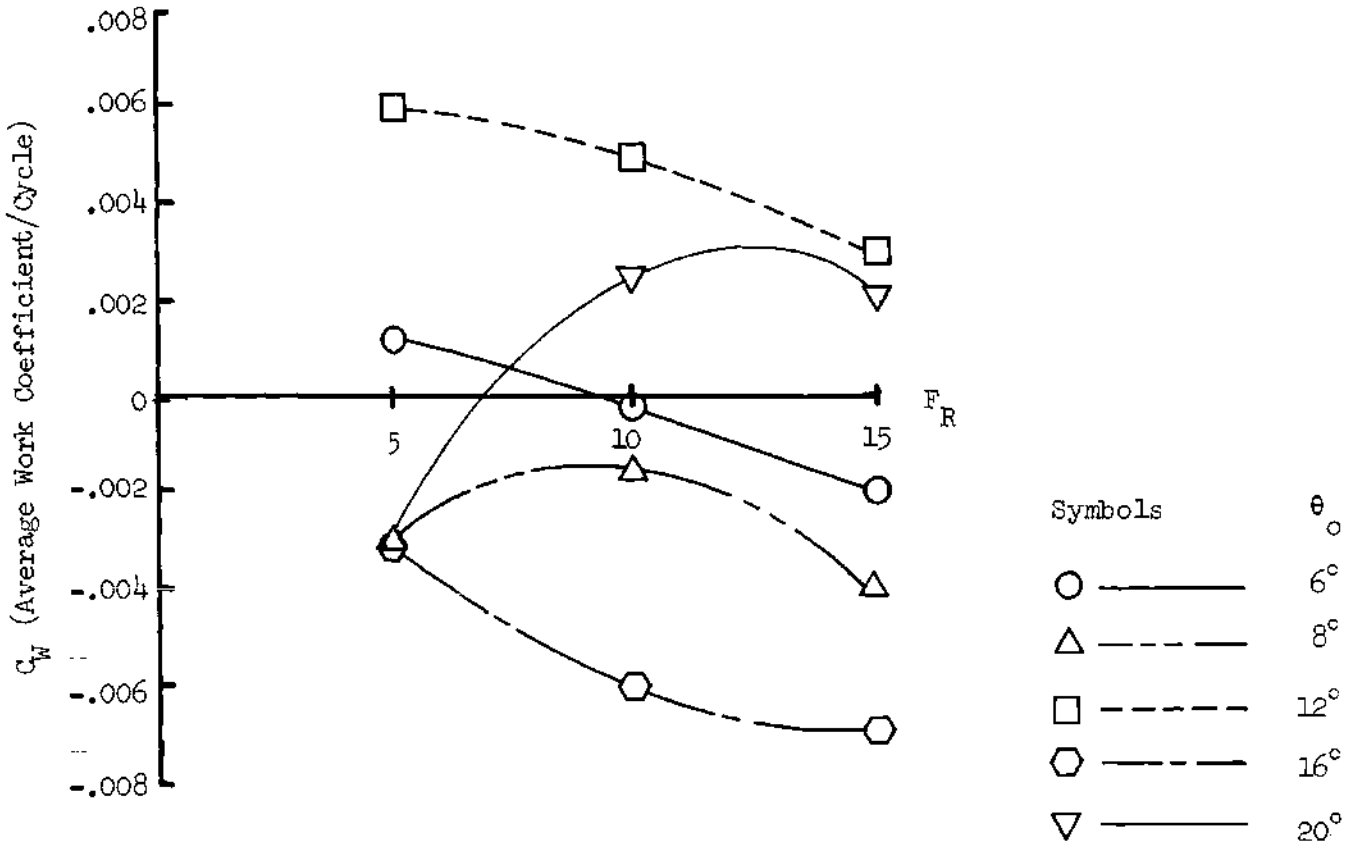

Figure 5-11. Work Coefficient versus Frequency Ratio for $\Delta\theta = \pm 2^{\circ}$

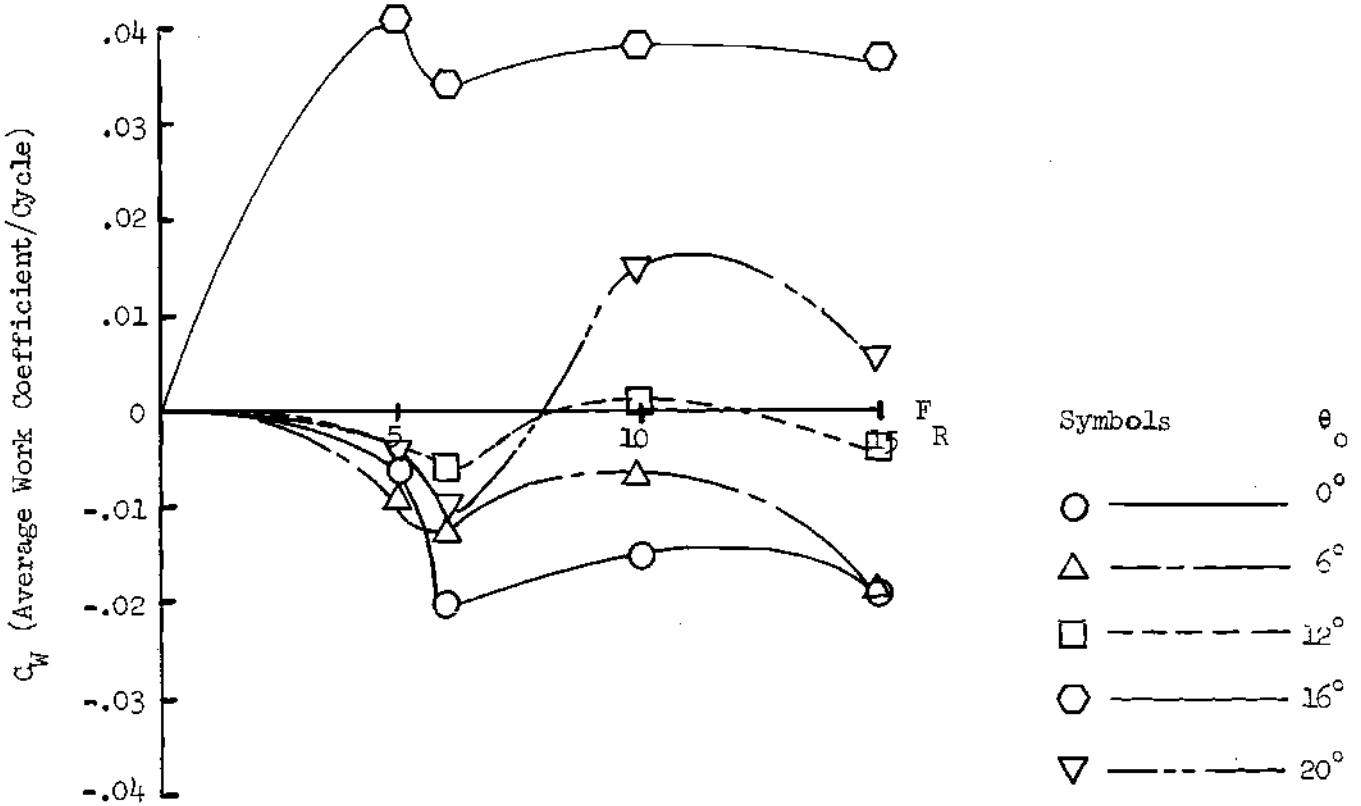

Figure 5-12. Work Coefficient versus Frequency Ration for $\Delta\theta = \pm 4°$

Table 5-1. Experimental Variation in Work Coefficient

Mean Angle	Frequency Ratio	Average C_W for Groups of 100 Cycles (Percent Deviation from Overall Average)				
4°	00	- .00364	- .00379	- .00418	- .00563	- .00370
		(13.1)	(9.5)	(0.2)	(34.4)	(11.6)
8°	15	- .00432	- .00467	- .00390	- .00482	- .00508
		(5.2)	(2.5)	(14.4)	(5.7)	(11.4)

particular test conditions. Each value of work coefficient represents the average C_W over 100 cycles of airfoil oscillation. The data point which was plotted for each test condition was then taken as the average of the five groups.

The aerodynamic work done on the airfoil was found to be sensitive to drift of the model oscillation frequency. Variations in frequency of only 1/3 Hertz produced noticable changes in the average work coefficient. This effect was caused by the use of the narrow bandpass filter to match the accelerometer and strain gage signals (see Figure 5-1). As the airfoil frequency changed, the amount of phase shift required to match the signals also varied. This phase shift altered the signal representing the aerodynamic moment which was generated on the analog computer.

CHAPTER VI

PITCHING OSCILLIATIONS AT LOW MEAN ANGLES

An extensive literature survey has revealed that several authors have developed analytical techniques to predict the forces and moments acting on an airfoil executing pitching oscillations in an unsteady free-stream [25-28]. For this investigation, the lift and moment data for low mean angles of attack were compared with the analytical results obtained using the method given in Reference 28. In addition, this technique was used in the development of analytical expressions for the aerodynamic work done on a pitching airfoil.

Lift and Moment Equations

J. Mayo Greenberg [28] developed expressions for the total force and moment acting on a two dimensional airfoil executing pitching and translational oscillations in an incompressible, pulsating freestream. This theoretical development uses unsteady, potential flow theory, with the effects of a continuous sheet of vorticity in the airfoil wake. The theory allows for different frequencies of freestream velocity and airfoil motion, and also takes into account the different initial amplitudes of each parameter as a phase angle with respect to the associated frequency.

The theory assumes the phase difference occurs in the expressions for airfoil displacement, as shown below.

$$V = V_o\left(1 + V_1 e^{i\omega_v t}\right) \tag{6-1}$$

$$\Delta\theta = B_o e^{i(\omega_b t + \varphi_b)} \tag{6-2}$$

$$h = h_o e^{i(\omega_h t + \varphi_h)} \tag{6-3}$$

For the experiments discussed in this thesis, the phase difference between velocity and displacement was applied to the velocity term, since only the airfoil displacement at $t = 0$ was known. Therefore, for the present investigation with $h = 0$

$$V = V_o\left(1 + V_1 e^{i(\omega_v t + \varphi)}\right) \tag{6-4}$$

$$\Delta\theta = B_o e^{i\omega_b t} \tag{6-5}$$

Equations (6-4) and (6-5) were used to modify Greenberg's original equations. The resulting equations are given, using, where required, the notation of this paper.

The total lift force acting on a two dimensional airfoil (positive up) is given below (see Equation (12a) of Reference 28).

$$L = \pi\rho b^2 \left\{ V\Delta\dot{\theta} + \dot{V}\,(\theta_o + \Delta\theta) - ba\Delta\ddot{\theta} \right\} \tag{6-6}$$

$$+ 2\pi\rho bV \left\{ V_o\theta_o + V_o\theta_o V_1 C(k_v)\; e^{i(\omega_v t+\varphi)} \right.$$

$$\left. + \left[b(\tfrac{1}{2} - a)\,\Delta\dot{\theta} + V_o\Delta\theta \right] C(k_b) + V_o V_1 \Delta\theta C(k_{vb})\; e^{i(\omega_v t+\varphi)} \right\}$$

where:

$$k_v = \omega_v b/V_o \tag{6-7}$$

$$k_b = \omega_b b/V_o \tag{6-8}$$

$$k_{vb} = (\omega_v + \omega_b)b/V_o \tag{6-9}$$

and $C(k)$ is Theodorsen's function [29].

$$C(k) = F(k) + iG(k) \tag{6-10}$$

The total moment (positive nose up) acting on the airfoil is given below (see Equation (12b) of Reference 28).

$$M = -\pi\rho b^2 \left\{ b(\tfrac{1}{2} - a)V\Delta\dot{\theta} - ba\,\dot{V}(\theta_o + \Delta\theta) + b^2\,(\tfrac{1}{8} + a^2)\Delta\ddot{\theta} \right\} \tag{6-11}$$

$$+ 2\pi\rho b^2\,(a + \tfrac{1}{2})\,V \left\{ V_o\theta_o + V_o\theta_o V_1 C(k_v)\; e^{i(\omega_v t+\varphi)} \right.$$

$$\left. + \left[b(\tfrac{1}{2} - a)\Delta\dot{\theta} + V_o\Delta\theta \right] C(k_b) + V_o V_1 \Delta\theta C(k_{vb})\; e^{i(\omega_v t+\varphi)} \right\}$$

Equations (6-6) and (6-11) reduce to the original Theodorsen equations [29] when the freestream velocity is constant.

$$V_1 = 0 \tag{6-12}$$

$$\omega_v = 0 \tag{6-13}$$

$$\varphi = 0 \tag{6-14}$$

$$L\Big|_{V = cst} = \pi\rho b^2 \left\{V\Delta\dot{\theta} - ba\Delta\ddot{\theta}\right\} \tag{6-15}$$

$$+ 2\pi\rho bV \left\{V_o\theta_o + \left[b(\tfrac{1}{2} - a)\,\Delta\dot{\theta} + V_o\Delta\theta\right] C(k_b)\right\}$$

$$M\Big|_{V = cst} = -\pi\rho b^2 \left\{b(\tfrac{1}{2} - a)\,V\Delta\dot{\theta} + b^2\,(\tfrac{1}{8} + a^2)\Delta\ddot{\theta}\right\} \tag{6-16}$$

$$+ 2\pi\rho b^2\,(a + \tfrac{1}{2})V\left\{V_o\theta_o + \left[b(\tfrac{1}{2} - a)\Delta\dot{\theta} + V_o\Delta\theta\right] C(k_b)\right\}$$

During the experimental studies described here, the analog computer was started when the airfoil angle-of-attack reached a maximum. Thus, at $t = 0$

$$\theta = \theta_o + \Delta\theta_{max} \tag{6-17}$$

$$V = V_o(1 + V_1 \sin\varphi) \tag{6-18}$$

The variables in Equations (6-6) and (6-11) can be rewritten in complex notation as:

$$V = V_o \left\{1 + V_1 \sin (\omega_v t + \varphi)\right\} = R \left\{V_o \left(1 - iV_1 e^{i(\omega_v t+\varphi)}\right)\right\} \tag{6-19}$$

$$\dot{V} = V_o V_1 \omega_v \cos(\omega_v t + \varphi) = R \left\{V_o V_1 \omega_v e^{i(\omega_v t+\varphi)}\right\} \tag{6-20}$$

$$\theta = \theta_o + \Delta\theta = \theta_o + R \left\{B_o e^{i\omega_b t}\right\} \tag{6-21}$$

$$\Delta\dot{\theta} = - \omega_b \sin \omega_b t = R\left\{i\omega_b B_o e^{i\omega_b t}\right\} \tag{6-22}$$

$$\Delta\ddot{\theta} = - \omega_b^2 \cos \omega_b t = R \left\{- \omega_b^2 B_o e^{i\omega_b t}\right\} \tag{6-23}$$

Following the method of complex variable substitution described in Reference 28, Equations (6-6) and (6-11) are rewritten to reflect to present experimental work.

The first bracket in Equation (6-6) is written as

$$\pi\rho b^2 \left\{V_o(1 + V_1 \sin (\omega_v t + \varphi)) \ (-\omega_b B_o \sin \omega_b t)\right. \tag{6-24}$$

$$+ V_o V_1 \omega_v \cos (\omega_v t + \varphi) \ (\theta_o + B_o \cos \omega_b t)$$

$$\left. - ab(- \omega_b^2 B_o \cos \omega_b t) \right\}$$

The second bracket in Equation (6-6) is written as

$$2\pi\rho b\ R\left[V_o\left(1 - iV_1 e^{i(\omega_v t+\varphi)}\right)\right]\left\{V_o\theta_o\right. \tag{6-25}$$

$$+ R\left[- iV_o\theta_o V_1 C(k_v)\ e^{i(\omega_v t+\varphi)}\right]$$

$$+ R\left[b(\tfrac{1}{2} - a)C(k_b)\ i\omega_b B_o e^{i\omega_b t}\right]$$

$$+ R\left[V_o C(k_b)\ B_o e^{i\omega_b t}\right]$$

$$\left. + R\left[-iV_o V_1 C(k_{vb})B_o e^{i\omega_b t}\ e^{i(\omega_v t+\varphi)}\right]\right\}$$

After performing the indicated multiplications of the complex variables and taking the appropriate real portions of the resulting complex forms, expression (6-25) reduces to

$$2\pi\rho b\ V_o\left[1 + V_1 \sin(\omega_v t + \varphi)\right]\left\{V_o\theta_o\left[1 + V_1 F(k_v)\sin(\omega_v t+\varphi)\right.\right. \tag{6-26}$$

$$\left. + V_1 G(k_v)\cos(\omega_v t + \varphi\ )\right] + b(a - \tfrac{1}{2})\,\omega_b B_o\left[F(k_b)\sin\omega_b t\right.$$

$$\left. + G(k_b)\cos\omega_b t\ \right] + V_o B_o\left[F(k_b)\cos\omega_b t - G(k_b)\sin\omega_b t\right]$$

$$+ V_o V_1 B_o\left[G(k_{vb})\cos((\omega_v + \omega_b)\ t + \varphi)\right.$$

$$\left. + F(k_{vb})\sin((\omega_v + \omega_b)\ t + \varphi)\right]\Big\}$$

The expression for the lift on the airfoil is then obtained by adding expressions (6-24) and (6-26). The lift coefficient for the airfoil, normalized with respect to the mean freesreeam velocity, is then obtained and it is given as

$$C_L = L/\tfrac{1}{2}\rho V_o^2(2b) \tag{6-27}$$

and

$$C_L = \pi b \left\{ \frac{1}{V_o}\left(1 + V_1 \sin(\omega_v t + \varphi)\right)\left(-\omega_b B_o \sin \omega_b t\right) \right. \tag{6-28}$$

$$+ \frac{V_1}{V_o}\omega_v \cos(\omega_v t + \varphi)(\theta_o + B_o \cos \omega_b t)$$

$$\left. + ab\left(\frac{\omega_b^2}{V_o^2}\right) B_o \cos \omega_b t \right\}$$

$$+ 2\pi\left[1 + V_1 \sin(\omega_v t + \varphi)\right]\left\{\theta_o\left[1 + V_1 F(k_b) \sin(\omega_v t + \varphi)\right.\right.$$

$$\left. + V_1 G(k_v) \cos(\omega_v t + \varphi)\right] + b(a - \tfrac{1}{2})\omega_b \frac{B_o}{V_o}\left[F(k_b) \sin \omega_b t\right.$$

$$\left.\left. + G(k_b) \cos \omega_b t\right] + B_o\left[F(k_b) \cos \omega_b t - G(k_b) \sin \omega_b t\right]\right.$$

$$\left. + V_1 B_o\left[G(k_{vb}) \cos\left((\omega_v + \omega_b)t + \varphi\right) + F(k_{vb}) \sin\left((\omega_v + \omega_b)\right.\right.\right.$$

$$\left.\left.\left. t + \varphi\right)\right]\right\}$$

A comparison of Equations (6-6) and (6-11) shows that the equation for the aerodynamic moment is of the same form as that of the

airfoil lift. Therefore, after the substitution of various constant terms within the bracketed expressions of Equation (6-6), the equation for the moment coefficient, normalized with respect to mean freestream velocity, can be written using Equation (6-28).

$$C_M = M/\tfrac{1}{2}\,\rho V_o^2\,(2b)^2 \tag{6-29}$$

and

$$C_M = -\frac{\pi}{2}\Big\{b(a-\tfrac{1}{2})\left(\frac{1}{V_o}\right)\Big(1+V_1\sin(\omega_v t+\varphi)\Big)\Big(B_o\omega_b\sin\omega_b t\Big) \tag{6-30}$$

$$-ab\left(\frac{V_1}{V_o}\right)\omega_v\cos(\omega_v t+\varphi)\,(\theta_o+B_o\cos\omega_b t)$$

$$+\left(\frac{1}{8}+a^2\right)b^2\left(-\frac{\omega_b^2}{V_o^2}\right)B_o\cos\omega_b t\Big\}$$

$$+\pi(a+\tfrac{1}{2})\Big[1+V_1\sin(\omega_v t+\varphi)\Big]\Big\{\theta_o\Big[1+V_1F(k_b)\sin(\omega_v t+\varphi)$$

$$+V_1G(k_v)\cos(\omega_v t+\varphi)\Big]+b(a-\tfrac{1}{2})\,\omega_b\frac{B_o}{V_o}\Big[F(k_b)\sin\omega_b t$$

$$+G(k_b)\cos\omega_b t\Big]+B_o\Big[F(k_b)\cos\omega_b t-G(k_b)\sin\omega_b t\Big]$$

$$+V_1B_o\Big[G(k_{vb})\cos\Big((\omega_v+\omega_b)\,t+\varphi\Big)+F(k_{vb})\sin\Big((\omega_v+\omega_b)\,t+\varphi\Big)\Big]\Big\}$$

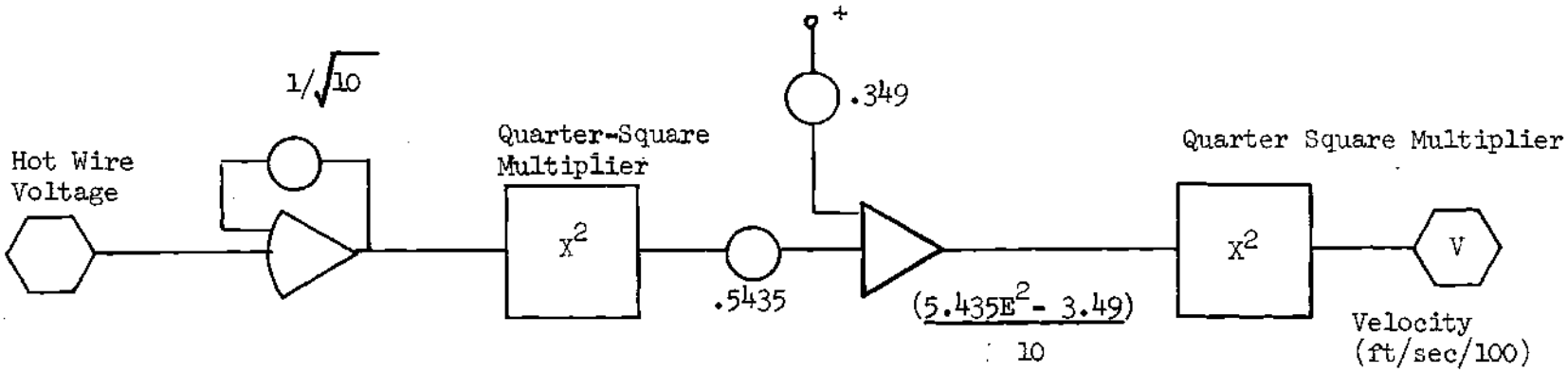

Note: Linear calibration equation for hot wire is given below

$$V = (5.435\ E^2 - 3.49)^2$$

Figure 6-1. Analog Mechanization Used to Convert Hot Wire Voltage Directly to Velocity

Constant Angle of Attack Data

The unsteady lift and moment acting on the model was determined for constant angles-of-attack ranging from two to eight degrees. Experimental data were obtained using the 50% and 75% gust generator vanes, with freestream gust frequencies of between 40 RPM and 120 RPM. The gust amplitude ratio ranged from

$$A_R = 0.10 \quad \text{to} \quad A_R = 0.66$$

where A_R, defined in terms of V_1, is given below.

$$A_R = \frac{D_a}{V_o} = \frac{2V_o V_1}{V_o} = 2V_1 \tag{6-31}$$

The analog computer was used to convert the hot wire voltage signal directly into freestream speed with units of feet per second. The analog mechanization that was used is shown in Figure 6-1. The output of amplifier A65 was the freestream velocity (ft/sec/100). This signal was applied to an integrating circuit (see Figure 4-17) to determine the tunnel mean speed during gust generator operation.

Equations (6-28) and (6-30) were used to determine theoretical values of the lift and moment coefficients corresponding to the experimental data. The value of V_1 was determined using the equations listed in Tables 2-5 and 2-6. In addition, for constant angle-of-attack

$$B_o = 0 \tag{6-32}$$

$$\omega_b = 0 \tag{6-33}$$

$$\varphi = 0 \tag{6-34}$$

Figure 6-2 shows a plot of the unsteady portion of the lift coefficient, R_L, versus amplitude ratio. The coefficient R_L, is related to the total lift as

$$C_L(t) = C_{L_o} + R\left\{R_L\, e^{i(\omega_v t + \varphi_L)}\right\} \tag{6-35a}$$

where

φ_L = phase angle between velocity and lift vector

C_{L_o} = steady portion of lift coefficient

Figure 6-3 is a graph of the unsteady portion of the moment coefficient versus amplitude ratio, where

$$C_M(t) = C_{M_o} + R\left\{R_M\, e^{i(\omega_v t + \varphi_M)}\right\} \tag{6-35b}$$

and where C_{M_o}, φ_M, and R_M are defined in a manner similar to C_{L_o}, φ_L, and R_L. In Figures 6-2 and 6-3, the analytical results obtained from Equations (2-28) and (6-30) are plotted with the experimental data.

In Figure 6-2, the correlation between theoretical and experimental values of R_L is good only for a constant angle of attack of two degrees. Figure 6-3 illustrates similar data correlations for R_M when the amplitude ratio is restricted to values smaller than $A_R = .15$.

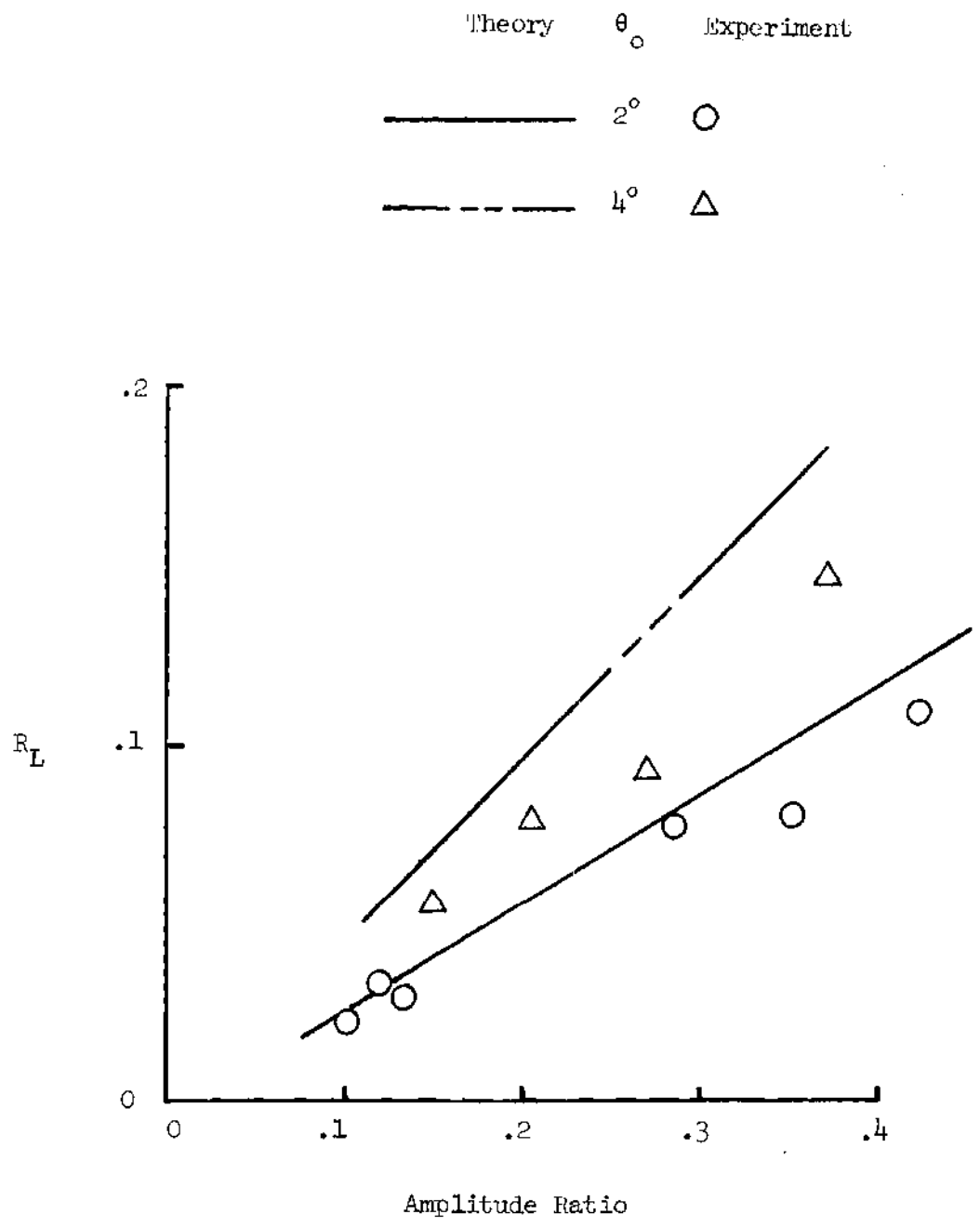

Figure 6-2. Unsteady Lift Coefficient versus Amplitude Ratio

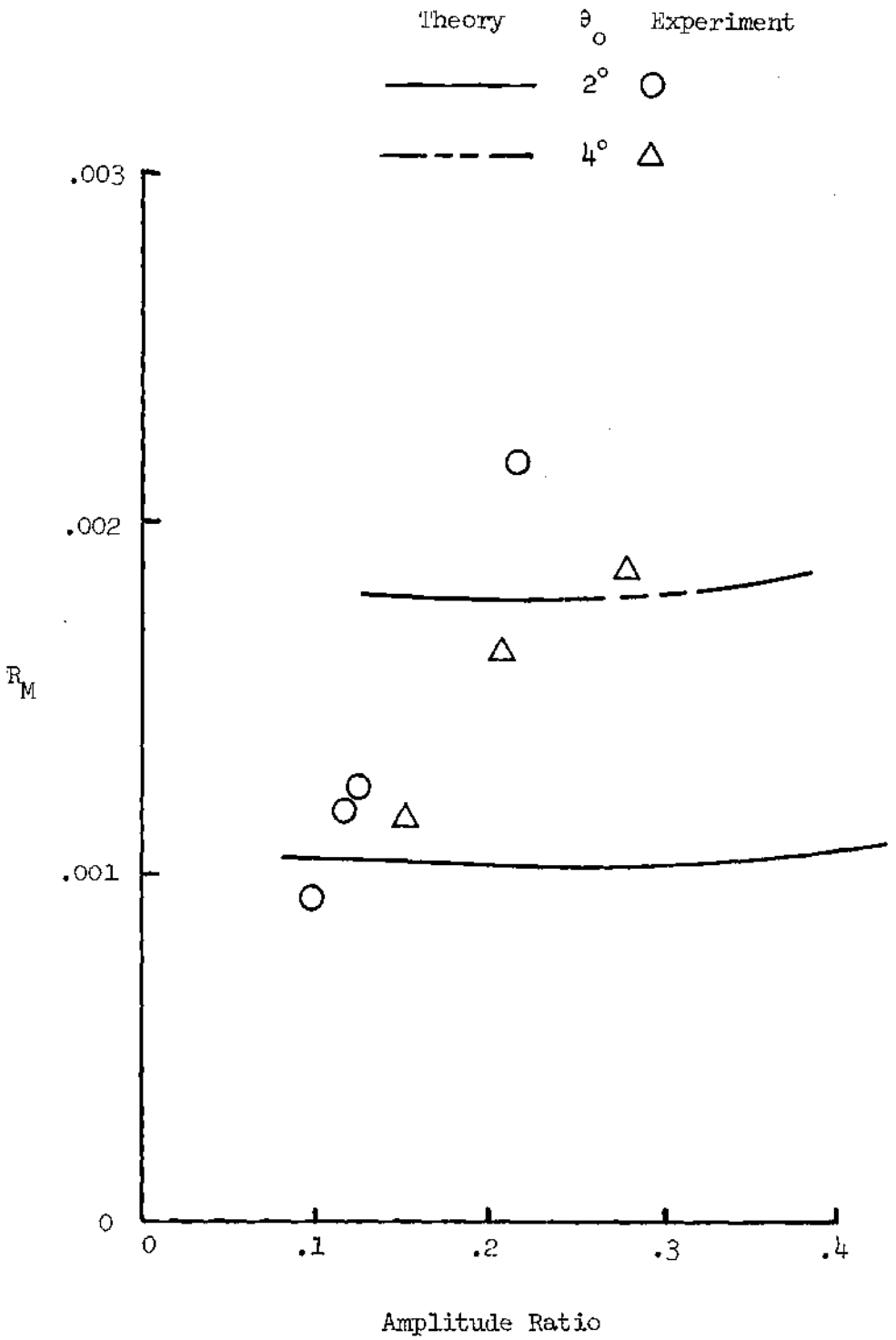

Figure 6-3. Unsteady Moment Coefficient versus Amplitude Ratio

Aerodynamic Work During Pitching Oscillations

An analytical expression for the work done on an airfoil oscillating in pitch was obtained by substituting Equation (6-30) into Equation (4-17), and performing the indicated integration. The resulting work coefficient, defined in Reference 30 as

$$C_W = \frac{\text{Work}}{\frac{1}{2}\rho V_o^2 (2b)^2} \tag{6-36a}$$

could then be evaluated as

$$C_W = \int_{T_1}^{T_2} C_M \dot{\theta} dt \tag{6-36b}$$

where

$$\dot{\theta} = -\omega_b \sin \omega_b t \tag{6-37}$$

and C_M is obtained from Equation (6-30).

The limits of integration are

$$T_2 = (2n + 2)\pi/\omega_b \tag{6-38}$$

$$T_1 = 2n\,\pi/\omega_b \tag{6-39}$$

where n represents each consecutive cycle of airfoil oscillation starting with $n = 0$ for the first cycle of oscillation.

The expression for the work coefficient was obtained by splitting

Equation (6-36) into twenty-one separate integrals and evaluating each integral at the limits given in Equations (6-38) and (6-39). The resulting equation for the work coefficient is given below.

$$C_W = -\frac{\pi^2 B_o^2 k_b}{2} \tag{6-40}$$

$$+ \frac{\pi}{4} k_v V_1 B_o^2 \left[F_R^2 \left(1 + \frac{A_o/B_o}{(1 - F_R^2)}\right)\right]$$

$$\left\{\cos\left[\frac{(2n + 2)\pi}{F_R} + \varphi\right] - \cos\left[\frac{2n\pi}{F_R} + \varphi\right]\right\}$$

$$- B_o\pi \left(a + \tfrac{1}{2}\right) \sum_{i=1}^{5} I_i$$

where

$$I_1 = 2\pi B_o \left[\left(a - \tfrac{1}{2}\right) k_b F(k_b) - G(k_b) - \frac{V_1^2 G(k_{vb})}{4}\right] \tag{6-41}$$

$$I_2 = \frac{V_1^2 F_R^2}{2} \left[\frac{A_o F(k_v)}{(F_R^2 - 4)} - \frac{B_o F(k_{vb})}{4(F_R + 1)}\right]\left\{\cos\left[\frac{(4n + 4)\pi}{F_R} + \varphi\right]\right\} \tag{6-42}$$

$$- \cos\left[\frac{4n\pi}{F_R} + \varphi\right]$$

$$I_3 = \frac{V_1^2 F_R^2}{2}\left[\frac{B_o G(k_{vb})}{4(F_R+1)} - \frac{A_o G(k_v)}{(F_R^2 - 4)}\right]\left\{\sin\left[\frac{(4n+4)\pi}{F_R} + \varphi\right]\right. \tag{6-43}$$

$$\left. - \sin\left[\frac{4n\pi}{F_R} + \varphi\right]\right\}$$

$$I_4 = V_1 F_R^2\left[\frac{B_o G(k_{vb})}{(2F_R + 1)} + \frac{2B_o F_R}{(1-4F_R^2)}\left[(a - \tfrac{1}{2})\, k_b G(k_b) + F(k_b)\right]\right. \tag{6-44}$$

$$\left. - \frac{A_o G(k_v)}{(F_R^2 - 1)}\right]\left\{\cos\left[\frac{(2n+2)\pi}{F_R} + \varphi\right] - \cos\left[\frac{2n\pi}{F_R} + \varphi\right]\right\}$$

$$I_5 = V_1 F_R^2\left[\frac{B_o F(k_{vb})}{(2F_R + 1)} + \frac{B_o\left[(a-\tfrac{1}{2})\, k_b G(k_b) + G(k_b)\right]}{(4F_R^2 - 1)}\right. \tag{6-45}$$

$$\left. - \frac{A_o(1 + F(k_v))}{(F_R^2 - 1)}\right]\left\{\sin\left[\frac{(2n+2)\pi}{F_R} + \varphi\right] - \sin\left[\frac{2n\pi}{F_R} + \varphi\right]\right\}$$

For a constant freestream velocity, the work coefficient is obtained from Equations (6-40) and (6-41).

$$C_W = -\frac{\pi^2 B_o^2 k_b}{2} - 2\pi^2 B_o^2 (a + \tfrac{1}{2})\left[(a - \tfrac{1}{2}) k_b\, F(k_b) - G(k_b)\right] \tag{6-46}$$

The first term on the right hand side of Equation (6-46) is the same expression given for the work coefficient in Reference 30.

Equation (6-40) was used to obtain theoretical estimates for C_W corresponding to several test conditions. Table 6-1 shows the data correlation for three constant velocity test conditions. These values of C_W represent averages over 500 cycles of airfoil oscillation. The good correlation between experimental and theoretical values of work coefficient for a constant freestream velocity provides a check on the accuracy of the method described in this thesis for the determination of aerodynamic work.

Table 6-2 compares the effects of frequency ratio on the value of C_W for a specific mean angle-of-attack. The work coefficient was again averaged over 500 cycles to eliminate phase effects. For the given test conditions, Table 6-2 indicates that the analytical expression derived for C_W provides a reasonable estimate for an average work coefficient, when the average is taken over a large number of cycles.

Table 6-1. Average Work Coefficient for Constant Freestream Velocity

(Airfoil frequency = 10 Hertz)

Mean Angle	Amplitude of Oscillation	Tunnel Velocity	$C_{W_{experimental}}$	$C_{W_{theoretical}}$	% Error
4°	2°	41.1 (ft/sec)	- .0034075	- .00345178	1.3
6°	2°	32.8 (ft/sec)	- .003997	- .00432942	7.8
8°	2°	32.4 (ft/sec)	- .004603	- .00438258	5.0

Table 6-2. Effects of Frequency Ratio on Work Coefficient for $\theta_o = 4^\circ$, $\Delta\theta = \pm 2^\circ$

(Airfoil Oscillation Frequency = 10.0 Hertz)

Gust Frequency	Gust Double Amplitude	$C_{W_{experimental}}$	$C_{W_{theoretical}}$	% Error
		- .0039007	- .00438257	10.9
.6667 (Hertz)	13.3 (ft/sec)	- .0045583	- .00437836	4.1
1.3333 (Hertz)	6.6 (ft/sec)	- .0041230	- .00438087	5.9
2.0 (Hertz)	3.7 (ft/sec)	- .0041726	- .00438259	4.8

CHAPTER VII

CONCLUSIONS AND RECOMMENDATIONS

A gust generator was designed and installed in the Georgia Tech Low-Turbulence Wind Tunnel. Experiments were conducted to determine the effects of an unsteady freestream on a two-dimensional airfoil. An operational analog computer was used to simultaneously determine the aerodynamic moment and the work done on the airfoil during pitching oscillations. The experimental data for each test condition were presented in the form of an average work coefficient obtained over a number of airfoil oscillation cycles.

Conclusions

1. The gust generator mechanism produces an axial variation in freestream velocity. The waveform of this velocity gust is relatively free of distortion throughout the operational range of the wind tunnel. The repeatability of the gust waveform is good.

2. Use of the analog computer greatly simplifies the determination of work done on the oscillating airfoil. Previous methods required either graphical calculation of the area inside the moment loop or the use of a digital computer to numerically integrate transducer data. At low mean angles and for constant freestream velocities, there was good correlation between the experimentally determined work coefficient and that predicted by established theory.

3. The unsteady freestream is shown to have a definite effect on the airfoil work coefficient. At large mean angles, the unsteadiness of the freestream can alter the sign, as well as the value of the work coefficient.

Recommendations

1. Additional experimental studies will be necessary to obtain a complete parametric study of the unsteady flow effects on an oscillating airfoil, due to the large number of variables involved in the problem.

2. A higher dynamic pressure will be necessary to improve the signal to noise ratio of the transducer output signals. In addition, a higher Reynolds number will allow the facility to more closely simulate the flow experienced by an actual helicopter rotor blade.

3. For the present facility, additional gust generator vanes which provide tunnel exit blockage of between 30 and 60 percent should be manufactured. This will increase the detectable aerodynamic fluctuations obtained with the smaller vanes, while permitting higher tunnel speeds with the larger vanes installed in the facility.

4. A more reliable motor control unit should be used with the model to obtain a constant oscillation frequency during tunnel operation. If possible, the vanes and airfoil should be geared together. This would simplify determining the phase between velocity and airfoil displacement.

APPENDIX A

CROSS-PLOTTING OF GUST GENERATOR CALIBRATION DATA

The original calibration of the gust generator facility was conducted using only three vane frequencies. These frequencies corresponded to freestream gust frequencies of 40, 80, and 120 RPM. In order to obtain additional operational curves at intermediate gust frequencies, the calibration data was cross-plotted as described below.

First, for each set of vanes, the three calibration equations were used to determine gust double amplitudes at each frequency corresponding to a constant tunnel speed. The coefficients of a quadratic equation:

$$D_a(f) = a\, f^2 + b\, f + c \qquad \text{(A-1)}$$

which passed through the three data points were obtained by solving the resulting set of simultaneous equations. This procedure was then repeated for twenty different values of wind tunnel speed. Thus, a family of curves was generated which related gust amplitude to gust frequency.

Next, intermediate values of gust frequency were substituted into each equation for gust double amplitude. This produced twenty data points of gust amplitude versus tunnel speed for each frequency. A least squares quadratic fit equation was obtained for the data at each intermediate gust frequency. These quadratic equations were then used as the operational calibration curves for the gust generator facility.

APPENDIX B

ANALYTICAL PREDICTION OF ELASTIC LINKAGE DIMENSIONS

The torsional stiffness of the elastic linkage was estimated using Timoshenko's membrane analogy [31] for rectangular bars. This method results in an expression for the effective spring constant, K_{eff} , given below

$$K_{eff} = \frac{4\, d c^3\, G\, \beta}{L} \qquad \text{(B-1)}$$

where

d = width of web

c = thickness of web

L = length of web

(see Figure 3-6)

G = shear modulus of elasticity

and

$$\beta = \frac{1}{3}\left\{ 1 - \frac{192}{\pi^5}\left(\frac{c}{4d}\right) \sum_{n=1,3,5,\ldots}^{\infty} \frac{1}{n^5} \tanh \frac{2n\pi d}{c} \right\} \qquad \text{(B-2)}$$

For given values of web length and width, an estimate of the mass moment of inertia for the airfoil was used to determine the thickness, c , of the spring web, which would cause a specified

torsional natural frequency.

$$\omega_n = \sqrt{K_{eff}/I_m} \tag{B-3}$$

From Equations (B-1) and (B-3)

$$c^3 = \left(\frac{I_m \omega_n^2 L}{4d\ G\ \beta}\right) \tag{B-4}$$

Since $\beta = f(c)$, Equation (B-4) can be rewritten as

$$c = \left[F(c)\right]^{1/3} \tag{B-5}$$

where

$$F(c) = \frac{I_m \omega_n^2 L}{4d\ G\ \beta(c)} \tag{B-6}$$

Successive iterations of Equation (B-5) were performed until the solution converged at the required value of thickness, c .

REFERENCES

1. Halfman, R. L., H. C. Johnson and S. M. Haley, "Evaluation of High-Angle-of-Attack Aerodynamic Derivative Data and Stall Flutter Prediction Techniques," NACA TN 2533, 1951.

2. Liiva, J., "Unsteady Aerodynamic and Stall Effects on Helicopter Rotor Blade Airfoil Sections," Journal of Aircraft, Vol. 6, No. 1, Jan-Feb. 1969.

3. Liiva, J. and F. J. Davenport," Dynamic Stall of Airfoil Sections for High-Speed Rotors," Journal of the American Helicopter Society, Vol. 14, No. 2, April 1969, pp. 26-33.

4. Liiva, J., F. J. Davenport, L. Gray and I. C. Walton, "Two-Dimensional Tests of Airfoils Oscillating Near Stall, Vol. I, Summary and Evaluation of Results," USAAVIABS TR 68-13A, U. S. Army Aviation Material Laboratories, Fort Eustis, Virginia, April 1968.

5. Carta, F. O., "Experimental Investigation of the Unsteady Aerodynamic Characteristics of an NACA 0012 Airfoil," United Aircraft Research Laboratories Report M-1283-1, August 1960.

6. Carta, F. O., G. L. Commerford, R. G. Carlson and R. H. Blackwell, "Investigation of Airfoil Dynamic Stall and Its Influence on Helicopter Control Loads," UASSMRDL Tech. Rep. 72-51, September 1972.

7. Tarzanin, F. J., Jr., "Prediction of Control Loads Due to Blade Stall," Journal of the American Helicopter Society, Vol. 17, No. 2, April 1972.

8. Bellinger, E. D., "Analytical Investigation of the Effects of Blade Flexibility, Unsteady Aerodynamics, and Variable Inflow on Helicopter Rotor Stall Characteristics," Journal of the American Helicopter Society, July 1972, pp. 35-44.

9. Johnson, W., "The Effect of Dynamic Stall on the Response and Air Loading of Helicopter Rotor Blades," Journal of the American Helicopter Society, April 1969.

10. Carta, F. O., G. L. Commerford and R. G. Carlson, "Determination of Airfoil and Rotor Blade Dynamic Stall Response," Journal of the American Helicopter Society, April 1973, pp. 31-39.

11. Crimi, P. and B. L. Reeves, "A Method for Analyzing Dynamic Stall of Helicopter Rotor Blades," NASA CR-2009, May 1972.

12. Ericsson, L. E. and J. P. Reding, "Unsteady Airfoil Stall," NASA CR-66787, July 1969.

13. Ham, N. D. and M. I. Young, "Torsional Oscillation of Helicopter Blades Due to Stall," Journal of Aircraft, Vol. 3, No. 3, May-June, 1966.

14. Rainey, A. G., "Measurement of Aerodynamic Forces for Various Mean Angles of Attack of an Airfoil Oscillating in Pitch and on Two Finite-Span Wings Oscillating in Bending with Emphasis on Damping in the Stall," NACA TN 3643, 1956.

15. Gray, L., J. Liiva and F. J. Davenport, "Wind Tunnel Tests of Thin Airfoils Oscillating Near Stall, Vol. I: Summary and Evaluation of Results," USAAVIABS TR-68-89a, January 1969.

16. Arcidiacono, P. J., F. O. Carta, L. M. Casellini and H. L. Elman, "Investigation of Helicopter Control Loads Induced by Stall Flutter," USAAVIABS Technical Report 70-2, March 1970.

17. Martin, J. M., R. W. Empey, W. J. McCroskey and F. X. Caradonna, "A Detailed Experimental Analysis of Dynamic Stall on an Unsteady Two-Dimensional Airfoil," Presented at the 29th Annual National Forum of the American Helicopter Society, Washington, D.C., May 1973, Preprint No. 702.

18. Johnson, W. and N. D. Ham, "On the Mechanism of Dynamic Stall," Journal of the American Helicopter Society, October 1972.

19. Ham, N. D., "Aerodynamic Loading on a Two-Dimensional Airfoil During Dynamic Stall," AIAA Journal, Vol. 6, No. 10, October 1968.

20. Despond, R. A. and J. A. Miller, "Separation in Oscillating Laminar Boundary-Layer Flows," Journal of Fluid Mechanics, Vol. 47, Part I, pp. 21-31, 1971.

21. Electronic Associates, Inc., Handbook of Analog Computation, edited by Alan Carlson, et al., 1967.

22. Electronic Associates, Inc., Continuous Data Analysis with Analog Computers Using Statistical and Regression Techniques, Applications Reference Library No. 1.3.2a; Bulletin No. 952015, August 1969.

23. Bratt, J. B., et al., "Free Oscillations of an Aerofoil About the Half-Chord Axis at High Incidences, and Pitching Moment Derivatives for Decaying Oscillations," ARC R & M 2214, September 1940.

24. Frost, M. D., "The Inertial Effects of Springs in Resonance and Free Oscillation Experiments to Determine Damping," Australian Aeronautical Research Laboratories, Report ACA-61, August 1959.

25. Isaacs, R., "Airfoil Theory for Flows of Variable Velocity," Journal of the Aeronautical Sciences, pp. 113-117, January 1945.

26. Isaacs, R., "Airfoil Theory for Rotary Wing Aircraft," Journal of the Aeronautical Sciences, pp. 218-220, April 1946.

27. Randall, D. G., "Forces on Aerofoils with Both Incidence and Forward Speed Varying," ARC R & M 3414, 1965.

28. Greenberg, J. M., "Airfoil in Sinusoidal Motion in a Pulsating Stream," NACA TN 1326, June 1947.

29. Theodorsen, T. and Garrick, I. E., "Nonstationary Flow about a Wing-Aileron-Tab Combination Including Aerodynamic Balance," NACA TR 736, December 1941.

30. Carta, F. O., "An Analysis of the Stall Flutter Instability of Helicopter Rotor Blades," American Helicopter Society 23rd Annual National Forum, Washington, D. C., May 10-12, 1967.

31. Timoshenko, S. D. and Goodier, J. M., Theory of Elasticity, McGraw-Hill Book Co., 1970.

VITA

John Bruce Malone, born on March 31, 1945, is the son of James T. and Florence H. Malone. He attended elementary and secondary schools in Bethesda, Maryland. After graduating from Walter Johnson Senior High School, he enlisted in the United States Marine Corps, in September, 1962.

While in military service, he attended the Marine Corps Electronics School, San Diego, California. After a tour of duty overseas, he was assigned to the Marine Corps Supply Depot, Albany, Georgia. Upon completion of his active duty tour, he was discharged from the service with the rank of Sargent, E-5.

After attending West Georgia College for nine months, Mr. Malone transferred to the Georgia Institute of Technology. In March, 1970, he was graduated with honor, receiving the degree, Bachelor of Aerospace Engineering. After entering graduate school at the Georgia Institute of Technology, he received the degree Master of Science in Aerospace Engineering, in June, 1971.

Mr. Malone is an associate member of the Society of the Sigma Xi and a member of Sigma Gamma Tau.

He is married to the former Linda Lynette Carden, of Bremen, Georgia.